The Pennsylvania State University

The Graduate School

Department of Aerospace Engineering

STATIC AND DYNAMIC CHARACTERIZATION OF COMPOSITE MATERIALS FOR FUTURE DRIVESHAFT SYSTEMS

A Thesis in

Aerospace Engineering

by

Todd C. Henry

Submitted in Partial Fulfillment
of the Requirements
for the Degree of

Master of Science

May 2012

The thesis of Todd Henry was reviewed and approved* by the following:

Charles E. Bakis
Distinguished Professor of Engineering Science and Mechanics
Thesis Co-Advisor

Edward C. Smith
Professor of Aerospace Engineering
Thesis Co-Advisor

George A. Lesieutre
Professor and Head of the Department of Aerospace Engineering

*Signatures are on file in the Graduate School

ABSTRACT

A single-piece fiber reinforced composite driveshaft is an attractive advancement over a multiple segmented metallic driveshaft. A composite driveshaft can be optimized to transmit power in a misaligned condition without the use of flexible couplers that add weight and complexity. Using a flexible matrix composite (FMC) for this application seems to be an attractive approach in comparison to a conventional rigid matrix composite (RMC) because of the potentially low energy dissipation and high cyclic strain capacity of elastomeric matrix materials. However, a lack of accurate models for critical strength and elastic properties of FMCs makes it necessary to experimentally characterize these parameters. Characterization of fiber dominated properties is further complicated by the presence of fiber undulations which are manufactured into the part during filament winding.

The objective of this research is to develop material characterization tools that provide the necessary inputs for the mechanical design of misaligned laminated composite driveshafts. A $[\pm\theta/89/\pm\theta]$ laminate was devised for the express purpose of evaluating the compressive strength and elastic modulus of the unidirectional composite in the fiber direction—properties which are believed to be strongly affected by fiber undulations. The fiber direction modulus back-calculated using this specimen design applied well to a range of laminates and winding patterns, although the fiber direction strength was found to be highly dependent on winding pattern. An empirical model relating the Young's modulus of the matrix material to the various quasi-static elastic and strength parameters of interest in shaft design was developed. This model is potentially useful for the rapid screening of candidate matrix materials.

Master curves representing the transverse and shear dynamic storage moduli and loss factors versus loading frequency and temperature were created for multiple candidate composites with different matrix stiffnesses. These curves, in conjunction with other properties measured in

this investigation, were used as inputs for a previously developed analytical tool for predicting the steady-state surface temperature of a spinning misaligned laminated composite shaft. Predictions from the model were compared to spin test data for several materials and laminates. Good agreement between the predicted and measured temperature increases was obtained for flexural strains up to approximately 2000 $\mu\varepsilon$, which encompasses the range of cyclic strains expected in rotorcraft driveshaft applications. In conclusion, the material characterization methods developed in this investigation have been shown to provide good estimations of all material properties of relevance in the mechanical aspects of driveshaft design.

TABLE OF CONTENTS

LIST OF FIGURES

LIST OF TABLES

ACKNOWLEDGEMENTS

I would like to thank Dr. Charles E. Bakis and Dr. Edward C. Smith for making time weekly to help me in overcoming problems encountered during my time at The Pennsylvania State University. The work presented in this document was not usually easy but Dr. Bakis was always there with carefully thought out suggestions that ultimately lead to the completion of my degree.

I would also like to thank Harish Chandra, Ian Laskowitz, and Amy Clement from Chemtura Corporation for supplying curatives for my research on a free sample basis. I would like to thank Dr. Ralph Colby and Dr. Nichole Brown for allowing me to use their labs to conduct dynamic mechanical testing. I would like to thank Dr. Gordon Kahle from Cytec Industries for using his free time to formulate multiple new prepolymer resins for me to investigate on a free sample basis. Additionally I would like to thank Dr. Thomas Juska for technical advice and suggestions.

This project was funded by the Vertical Lift Consortium (VLC) and the National Rotorcraft Technology Center (NRTC), U.S. Army Aviation and Missile Research, Development and Engineering Center (AMRDEC) under Technology Investment Agreement W911W6-05-2-0003, entitled National Rotorcraft Technology Center Research Program. I would like to acknowledge that this research and development was accomplished with the support and guidance of the NRTC and VLC. The views and conclusions contained in this document are mine and should not be interpreted as representing the official policies, either expressed or implied, of the AMRDEC or the U.S. Government. The U.S. Government is authorized to reproduce and distribute reprints for Government purposes notwithstanding any copyright notation thereon. I

also thank the US Department of Defense for supporting my graduate studies through the SMART scholarship program.

I would like to especially thank Mr. Simon Miller for his seemingly endless supply of help in tooling and machining as well as electrical wiring and LabVIEW program writing. Lastly I would like to thank my family for being there to support me when things were going well and to cheer me up when things were not.

Chapter 1

Introduction

1.1 Background

Rotary wing aircraft, such as a helicopter, can perform jobs that their fixed wing counterparts cannot. They aerially pursue criminals, fight fires, report the news, rescue civilians in danger, transport civilians, and support the armed services. Two common restrictions that affect a helicopter's ability to complete these objectives are the time it can remain on station, and downtime incurred during regularly scheduled maintenance of the helicopter. Designers strive to minimize the weight of helicopters to increase the time for hover or gross payload. Designers also look for ways to minimize the number of parts to decrease maintenance downtimes.

Tail rotor driveshafts and interconnects have been the focus of on-and-off research in recent years. Current helicopter driveshafts are made of multiple, short metal shafts that are connected together via flexible couplers that accommodate inevitable shaft misalignment. Shaft misalignment is caused by loads on the airframe from crosswinds or regular maneuvering. The flexible couplers keep the metal shaft, usually aluminum, from developing cracks associated with cyclic fatigue loading during operation. Mid-span hangar bearings are spaced along the driveline to hold the shaft segments to the airframe while restricting the shaft segments from touching the airframe. The current multi-segmented driveline concept "gets the job done", but leaves much to be desired in terms of weight, complexity, and maintenance.

Many researchers have attempted to replace the multi segmented metallic driveshaft with a composite shaft consisting of carbon, boron, or glass fibers and an epoxy matrix. Replacing metallic driveshafts with composite driveshafts for low speed applications has already been

investigated in automotive and power generation applications, (Singh et al., 1996). To achieve the maximum amount of weight reduction, Hetherington et al. (1990) designed a single piece composite shaft to operate in the supercritical range, or at a speed above the shaft's first natural frequency. Composite driveshaft designs were able to provide a reduction in weight but some designs required additional damping, did little to reduce the amount of maintenance parts, or did not consider shaft misalignment which causes heating and fatigue failures (Darlow and Creonte, 1995; Zinberg 1970).

An optimum material for a one-piece helicopter driveshaft would need to be flexible in bending, such that during operation the shaft does not fail by fatigue or overheating, and also torsionally stiff for power transmission. Flexible matrix composites, FMCs, have high strength fiber and elastomeric matrix constituents making an FMC able to provide very high anisotropy for unique design cases such as a helicopter driveshaft (Hannibal and Avila, 1984; Ocalan, 2002; Shin et al., 2003; Mayrides et al., 2005). A single piece FMC driveshaft must be able to resist buckling, whirling, stress/strain, and temperature related failures (Roos and Bakis, 2011). The weight savings of a FMC driveshaft will be realized by eliminating the need for flexible couplers and reducing the number of hangar bearings in a final optimized design (Fig. **1-1**).

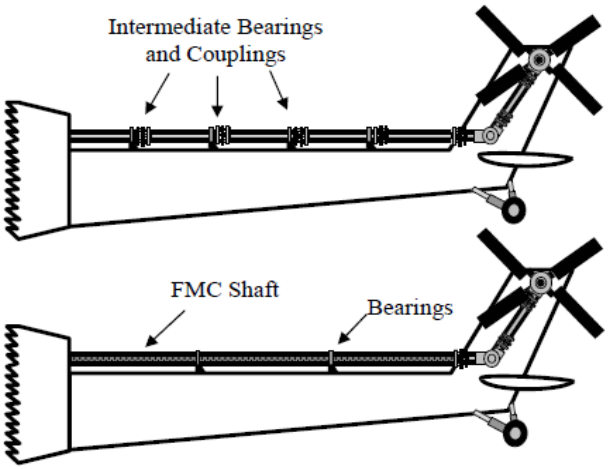

Figure **1-1**: Comparison of current driveline (top) and proposed FMC driveline (bottom), (Mayrides, 2005)

1.2 Previous Work

1.2.1 Quasi Static Modulus and Strength Properties

In this document, rectangular Cartesian coordinates aligned with the fibers in a ply are denoted the 1-2 system, with 1 being the fiber direction. In a filament wound shaft, the axial or longitudinal direction is referred to as the *x*-direction while the hoop-direction is the *y*-direction. These coordinate definitions are shown in Fig. **1-2**.

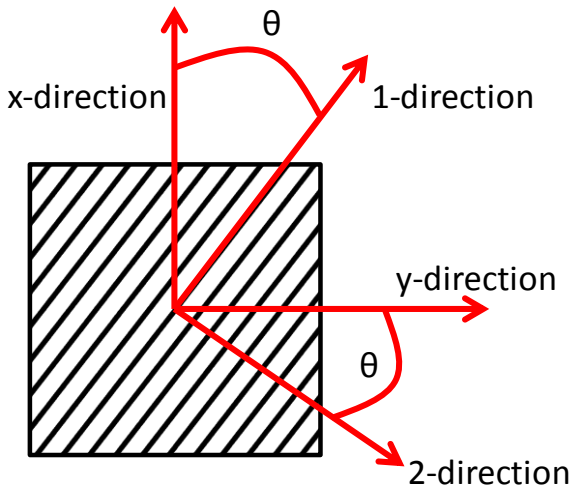

Figure **1-2**: Composite principle (12) and non-principle (*xy*) axes

One of the key difficulties in screening materials for FMC driveshafts is the difficulty in predicting the ply-level elastic properties and strengths using micromechanics-based analysis and classical laminated plate theory (CLPT) (Daniel and Ishai, 2006). The "rule of mixtures", RoM, is a method for estimating the material properties of a composite in the fiber direction based on the volume weighted average of the constituents of the composite. Sollenberger (2010) showed that the RoM expression for the fiber direction modulus, E_1, in compression did not agree well with values backed out from filament wound tube experiments using CLPT. Backed out values

of shear modulus, G_{12}, and shear strength, F_6, from CLPT are also known to be inaccurate (Crane and Ratcliffe, 1993).

Some of these discrepancies can be attributed to the effects of fiber undulations. Models of textile composites address the strength of undulated fibers as well as the modulus (Ishikawa and Chou, 1982), but these models are confined to orthogonally-crossing fibers. Filament wound tubes often have angle plies, where the fibers to not cross each other orthogonally. Approaches for modeling the axial modulus of filament wound FMC tubes have been presented by Zindel and Bakis (2011) and Jensen and Pai (1993) although neither model has been well vetted with extensive experimental data. The key features of these models are recognition of the modulus-reducing effects of out-of-plane fiber undulations that occur where fibers cross under and over each other in filament winding. Zindel and Bakis (2011) recognized that the compressive longitudinal modulus of fibers in a flexible matrix is less than the tensile modulus and also included non-linear behavior

Previous research by Sollenberger (2010) aimed to back out the in-situ fiber-direction modulus of FMC material in filament wound tubes using an empirical approach. Tubes of various angle-ply lamination arrangements ranging from ±20-deg. to almost 90-deg. (a circumferential winding pattern) were manufactured and loaded in axial compression to failure. Tubes with ±45-deg. plies provided the longitudinal shear modulus of the plies, G_{12}, while hoop-wound tubes provided the transverse modulus of the plies, E_2. The longitudinal Poisson's ratio of the lamina, ν_{12}, was calculated using the rule-of-mixtures and the longitudinal modulus E_1 was backed out with CLPT to match the axial modulus of the laminated tube, E_x. As can be seen in Fig. **1-3**, the extrapolated axial modulus of tubes with a hypothetical wind angle of 0-deg. (i.e., all axially oriented fibers), which actually provides the value of E_1 of the plies, ranges between 43 GPa and 60 GPa, depending on the sign of stress applied to the tubes. As expected due to the low modulus of the matrix (~245 MPa), the backed out E_1 is less in compression than in tension.

More important, however, is the discrepancy between either of these E_1 values and the predicted value of 145 GPa that one obtains using the RoM with the known fiber volume fraction and constituent properties. The discrepancy between the CLPT fit for the tension experiments and the CLPT fit for the compression experiments is about 30 %. Clearly, conventional models cannot be used to model the modulus of these tubes. Additionally, it was observed that the axial compressive strength of the tubes peaked with fiber angles of around ±20-deg. and decreased at smaller angles, which is also in disagreement with conventional analysis.

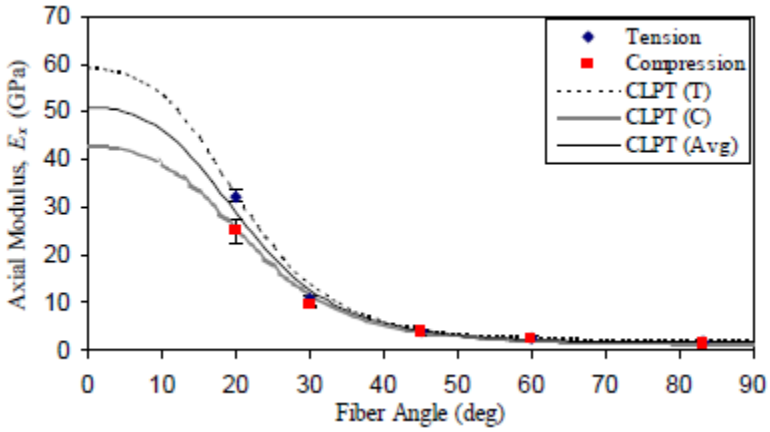

Figure **1-3**: FMC axial modulus versus fiber angle θ_x – experiments and theory (Sollenberger 2010)

Claus (1994) found that varying the winding pattern, elaborated on later, in different plies affected the axial compressive strength of the carbon/epoxy tubes. His results on the effect of winding pattern on axial modulus of the tube were inconclusive. Adams and Welsh (1997) demonstrated that the in-situ compressive strength of fibers in a laminate is dependent on the degree of constraint provided by adjoining plies. The compressive strength of fibers in most practical multi-directionally reinforced laminates can significantly exceed that in 0-deg. unidirectional coupons. Analytical models for the compressive strength of fibers in general

filament wound composites do not recognize the unique fiber architecture of filament wound tubes.

1.2.2 Dynamic Properties

The unique high anisotropy of a FMC can make using FMCs in design technically challenging. FMC materials are viscoelastic and have very large strain to failure. For example Shan (2006) measured strain to failure in the transverse direction to be as high as 28 % for a polyurethane matrix FMC. Visco-elastic behavior, or damping, leads to hysteretic self heating. Damping behavior in fiber composites has been investigated using a macro-mechanical strain energy method by Adams and Bacon (1973) (Crane, 1993). Shan (2002) extended Adam's work by adding the fractional derivative viscoelastic constitutive behavior developed by Bagley and Torvick (1979). To characterize the visco-elastic behavior of a material, a sinusoidal stress can be applied to the material while the sinusoidal strain is measured (Fig. **1-4**). If the material is purely elastic the stress and strain will be completely in phase, whereas if the material is completely viscous the stress and strain will be 90° out of phase.

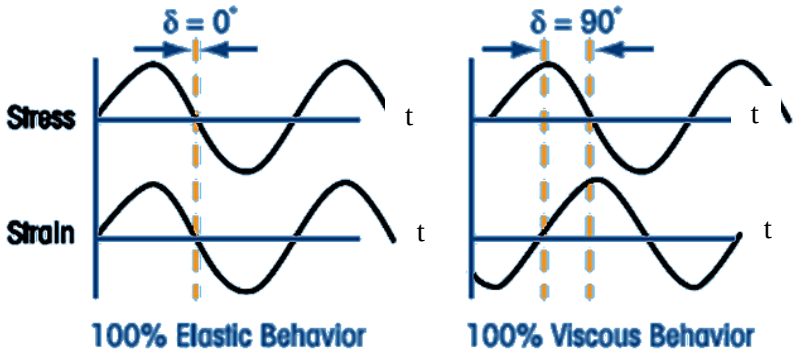

Figure **1-4**: Dynamic oscillatory test: elastic and viscous behaviors plotted vs. time (TA Instruments, 2010)

The complex modulus of the material, E^*, is amplitude of the stress divided by the amplitude of the strain. The phase difference between the stress and strain responses, δ, is also measured in the test and can be used to find the storage, E', and loss, E'', modulus of the material (Fig. **1-5**). The storage modulus is related to the elastic part of the response that is in phase. The loss modulus is related to the viscous part of the response that is out of phase, which dissipates energy and causes hysteretic heating. The loss factor, $\tan\delta$ also referred to as η, is the ratio of the storage modulus and loss modulus.

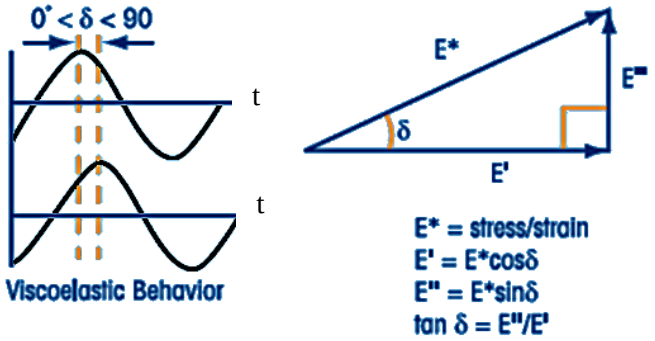

Figure **1-5**: Dynamic oscillatory test: storage modulus, loss modulus, tan delta (TA Instruments, 2010)

Dynamic tests in this research are carried out either in bending, for transverse dynamic mechanical properties (DMA) of a beam, or in torsion, for shear DMA properties of a rod. When a DMA test is carried out over a large range of temperatures and frequencies, the Williams-Landel-Ferry (WLF) function, equation (1), can be used to shift the storage modulus and loss factor responses relative to a reference temperature, T_r, to create a master curve. There are many shifting function available in the literature but Ferry (1970) has proven that the WLF function can be fit to a broad range of visco-elastic materials.

$$log(\alpha_t) = \frac{-C_1(T - T_r)}{C_2 + (T - T_r)} \quad (1)$$

α_t are the temperature shifting factors for which values are selected to fit by eye for each test temperature T. C_1 and C_2 are constants found by fitting equation(1) to the temperature shift factors and associated temperatures. This technique is carried out on the properties of the material that are most dominated by the viscoelastic behavior of the matrix—i.e. the transverse and shear moduli.

A fractional derivative constitutive model was developed in understanding viscoelastic damping of polymers (Bagley and Torvick, 1979) and used to predict the heating of an FMC shaft exposed to cyclic loading by misalignment (Shan and Bakis, 2009). In the model developed by Shan and Bakis (2009), fiber dominated properties are considered to be constant for all frequencies and temperatures as is the Poisson's Ratio. The generalized stress-strain relationship for the fraction derivative constitutive model (Shan, 2009) is expressed as equation (2).

$$\sigma(t) + \sum_{k=1}^{n} a_k D^{\beta_k}\sigma(t) = E\varepsilon(t) + E\sum_{k=1}^{n} b_k D^{\beta_k}\varepsilon(t) \tag{2}$$

where each of the fractional derivatives, $D^{\beta k}$, are defined as

$$D^{\beta_k}[x(t)] = \frac{1}{\Gamma(1-\beta_k)}\frac{d}{dt}\int_0^t \frac{x(\tau)}{(t-\tau)^{\beta_k}}d\tau \tag{3}$$

with β_k equal to zero for purely elastic and one for purely viscous materials, and

$$\Gamma(x) = \int_0^{\infty} t^{x-1}e^{-t}dt, \qquad (x > 0) \tag{4}$$

For harmonic excitation of the form $\sigma(t) = \sigma_0 e^{i\omega t}$ and response $\varepsilon(t) = \varepsilon_0 e^{i\omega t}$ equation (2) gives

$$\sigma_0 = E\varepsilon_0 \frac{1 + \sum_{k=1}^{n} b_k (i\omega)^{\beta_k}}{1 + \sum_{k=1}^{n} a_k (i\omega)^{\beta_k}} \tag{5}$$

The storage modulus, loss modulus, and loss factor are defined by equations 6-8.

$$E' = \frac{AC + BD}{C^2 + D^2} E \tag{6}$$

$$E'' = \frac{BC - AD}{C^2 + D^2} E \tag{7}$$

$$\eta = \frac{E''}{E'} = \frac{BC - AD}{AC + BD} \tag{8}$$

A, *B*, *C*, and *D* are defined by two fractional derivatives determined to be sufficient by Shan and Bakis (2009), equations 9-12.

$$A = 1 + b_1 \omega^{\beta_1} \cos\left(\frac{\pi\beta_1}{2}\right) + b_2 \omega^{\beta_2} \cos\left(\frac{\pi\beta_2}{2}\right) \tag{9}$$

$$B = b_1 \omega^{\beta_1} \sin\left(\frac{\pi\beta_1}{2}\right) + b_2 \omega^{\beta_2} \sin\left(\frac{\pi\beta_2}{2}\right) \tag{10}$$

$$C = 1 + a_1 \omega^{\beta_1} \cos\left(\frac{\pi\beta_1}{2}\right) + a_2 \omega^{\beta_2} \cos\left(\frac{\pi\beta_2}{2}\right) \tag{11}$$

$$D = a_1 \omega^{\beta_1} \sin\left(\frac{\pi\beta_1}{2}\right) + a_2 \omega^{\beta_2} \sin\left(\frac{\pi\beta_2}{2}\right) \tag{12}$$

The variables E, b_1, β_1, b_2, β_2, a_1, and a_2 are values unique to the transverse or shear properties of a material and ω is the frequency of sinusoidal loading in radians per second. To apply temperature shifting, the WLF equation, angular frequency ω is replaced by $\alpha_T f$ where $\omega = 2\pi f$. This substitution allows for equations 2-4 to be obtained over a range of temperatures and frequencies for creating a master curve.

Shan and Bakis (2009) applied this fractional derivative constitutive model to predict the heating for a FMC with a 58 MPa neat resin with very good agreement at different speeds and

flexural strains (Fig. **1-6**). They were also able to show that they could predict the heating of tubes of angles 45°, 60°, and 75° as well.

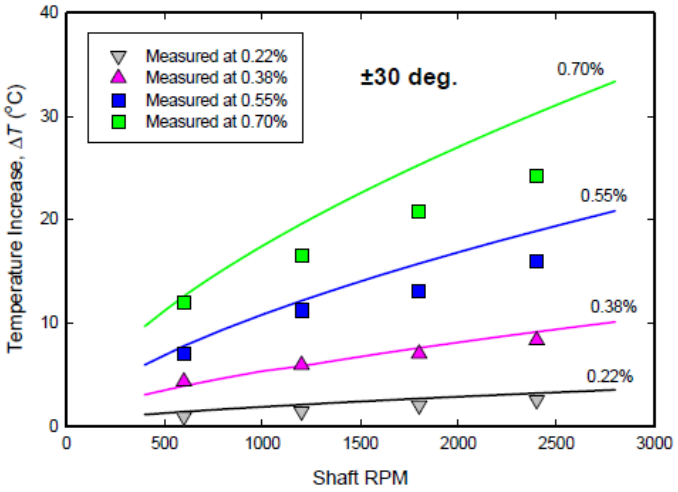

Figure **1-6**: Temperature increase of a ±30-deg. Shaft for various speeds and flexural strains (Shan and Bakis 2009)

1.3 Objectives/Goals

The objective of this research investigation is to develop a material characterization tools for a carbon fiber reinforced composite driveshaft with a main focus on test methods for determining all the strengths and elastic properties as well as dynamic material characterization for use in predicting self-heating due to cyclic flexural strain in a spinning shaft. The neat resin properties, dynamic properties in transverse and shear for self heating, as well as ply elastic and strength properties need to be developed for a variety of resins. The discrepancies in experimental and calculated modulus of filament wound tubes discussed above provide a challenge. A filament wound tubular specimen that is amenable to the determination of the in-situ fiber-direction Young's modulus, E_1, and compressive strength, F_{1c}, using a back-out approach needs to be found. The backed-out ply properties should be applicable to a range of laminates

that might be used in shafts designed with FMC materials. The specimen design is evaluated based on its ability to conform to CLPT axial modulus calculations and to provide fiber-dominated compressive failures. Additionally all composite material strengths and elastic properties will be related to the neat resin modulus. The approach of the current investigation involves the following tasks:

- Experimentally determine quasi-static material properties: neat resin modulus, neat resin Poisson's Ratio, ply elastic properties E_2, G_{12}, and ν_{12}, and strengths F_{2C}, F_{2T}, and F_6
- Filament wind tubular specimens using different winding patterns through the thickness of the specimen to determine strength and modulus dependence on winding pattern
- Filament wind tubular specimens using flexible and rigid polymer matrices and different fiber angles to determine a specimen design that lends itself to a single backed out value of E_1 using CLPT
- Back calculate laminate-independent values of F_{1c} for flexible and rigid matrix composite tubes
- Characterize the frequency and temperature-dependent dynamic behavior of unidirectional FMC composite material systems with different resins and use the properties as inputs to a previously developed self-heating model of a spinning shaft
- Carry out spin tests on composite shafts without torque to assess the prediction capability of a previously developed self-heating model

Chapter 2

Specimen Fabrication

2.1 Materials

Six resins, consisting of a wide range of stiffnesses, were investigated for their potential use as a constituent in a filament wound composite driveshaft. The first, Adiprene LF750D (Chemtura, Middlebury CT), is a toluene diisocyanate (TDI) terminated polyether prepolymer. Two polyurethanes, Conathane DPRN 30748 and Conathane DPRN 30757, were custom formulated by Dr. Gordon Kahle (Cytec Industries, Olean NY). Both are TDI/polytetramethylene ether glycol (PTMEG) polyether prepolymers. Two additional polyurethanes, Conathane DPRN 30918 and Conathane DPRN 30917, also formulated by Dr. Kahle, are TDI/PTMEG/polycaprolactone (PCL) polyether prepolymers with the addition of triol. The addition of triol, a molecule with three hydroxyl functional groups, increases the stiffness of the cured material compared to the traditional polyol, which only has two hydroxyl functional groups in the other prepolymers. These polyurethane prepolymers, as listed, have an increasing amount of functional nitrogen-carbon-oxygen (NCO) groups meant to increase the crosslink density in the cured material to create an overall stiffer resin. The polyurethane prepolymers were cured with a delayed-action diamine curing agent—either Caytur 31 DA or Duracure C3LF (both from Chemtura, Middlebury CT). "Delayed" in this context means that the active ingredient in the curing agent is blocked in a type of salt, so that cure will not proceed at room temperature. The resin, mixed prepolymer and curative, has a long pot life at room temperature, making it ideal for filament winding. When the temperature is raised to the cure temperature, the curative becomes

unblocked and cross linking begins solidifying the material. The amount of parts curative per 100 parts prepolymer for polyurethanes, by mass, is calculated using equation (13),

$$W_{curative} = (\%NCO\ of\ polymer)\left(\frac{equivalent\ weight\ of\ curing\ agent}{42}\right)(.95) \quad (13)$$

where 42 is the molar mass in grams of one mole of NCO and 0.95 is the prepolymer manufacturer's recommended stoichiometry for optimal all-around mechanical performance. Specific information on mix ratios for the resins used in the present investigation is given in Table **2-1.**

Table **2-1**: Polyurethane prepolymer equivalent weight and mix ratio

Prepolymer Material/Curative	Equivalent Weight, g	Pre-polymer NCO, %	Pre-polymer Triol, %	Mix Ratio	
				with Caytur 31 DA, per 100 parts prepolymer	with Duracure C3LF, per 100 parts prepolymer
Adiprene LF750	472	8.9	0	50.3	49.7
Conathane 30748	420	10.0	0	56.5	55.9
Conathane 30757	350	12.0	0	67.9	67.0
Conathane 30918	350	12.0	5	67.9	67.0
Conathane 30917	350	12.0	10	67.9	67.0
Caytur 31 DA	250	-	-	-	-
Duracure C3LF	247	-	-	-	-

The last material used is EPON 862, an bisphenol A epoxide, cured with an aromatic amine curing agent, Curative W (both from Momentive Specialty Chemicals, Columbus, OH). The mass mix ratio recommended by the manufacturer for EPON 862 and Curative W is 100 parts to 26.4 parts, respectively.

2.2 Neat Resin Dogbones

Neat resin dogbone specimens were made using an open aluminum mold which has four open cavities that make specimens 25.4 cm long, 1.3 cm wide in the gage section, and 1.0 cm thick (Fig. **2.1)**. The mold was prepared by first abrading the open surfaces with Scotch-Brite™ 7440 heavy duty hand pads (3M St. Paul MN), removing dirt and other foreign contaminants. The mold was then wiped clean with acetone leaving a smooth, contaminant-free surface on the molding surfaces.

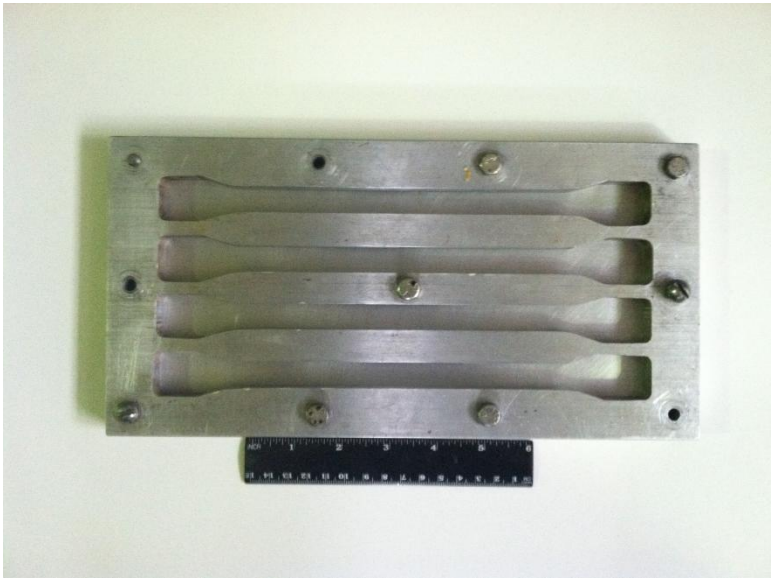

Figure **2-1**: Neat resin dogbone mold

A layer of silicone release agent, Ease Release 200™ (Mann Formulated Products, Easton PA), was then applied liberally to the open surfaces of the mold and the mold was placed in a convection heat oven at 140 °C (248 °F) to evaporate the solvents from the silicone. This is done two times for a period of thirty minutes each time. The prepolymer of interest is then mixed with the associated curative thoroughly at 50 °C. The resin is placed in a vacuum chamber under 30 inches of mercury (in Hg) to remove all air bubbles from within the resin which would become trapped after curing, leaving voids and reducing the quality of the specimen. When all

air bubbles have been removed from the resin, the resin is poured into the preheated dogbone mold. Polyurethane resin is cured at 140 °C (248 °F) for 2 h followed by a post cure at 100 °C (212 °F) for 16 h. The post cure gets makes sure there are no aging effects, or changes in material properties over time which can happen in soft materials. The cure schedule is 121°C (250 °F) for 1 h followed by 177 °C (350 °C) for 2 h for the epoxy matrix.

After the cure schedule is completed, the specimen is allowed to cool to room temperature. The specimens are removed from the mold and the top surfaces of the dogbones are machined flat and smooth using a grinding wheel to give a constant cross-section over the length. Three dogbone specimens of each resin type were made for quasi-static testing.

2.3 Filament Winding

Four types of specimens were fabricated using a McClean Anderson Super Hornet filament winder (Schofield WI). *Tubes* are hollow cylinders meant to be cut in multiple sections for compression testing. *Plates* are flat rectangular parts meant to be cut in multiple sections for testing in four-point bending and 10° off-axis tension. *Rods* are small solid cylinders from which one specimen will be taken. *Shafts* are hollow cylinders tested in their entirety as they were made. In this investigation only one fiber type was used. HexTow® AS4D-GP-12K carbon fiber is a high strength polyacrylonitrile (PAN) carbon fiber made by Hexcel Corporation (Stamford, CT). AS4D-GP-12K is a continuous tow consisting of 12000 individual carbon fibers.

All resin types were used in making parts with the wet filament winding technique. The process starts with the carbon fiber spool being placed in the fiber cabinet on a tensioning cylinder (Fig. **2-2**). The spool is placed over the tensioning cylinder which has a bladder across the outside, the carbon fiber spool is kept from rotating freely by air pressure which causes the bladder to expand holding the inside of the spool securely. The carbon fiber tow from the spool

is fed across two vertical pulleys which have pressure transducers that measure the force being put on the carbon fiber tow by the tensioner. The amount of tension on the carbon fiber tow can then be controlled by the user.

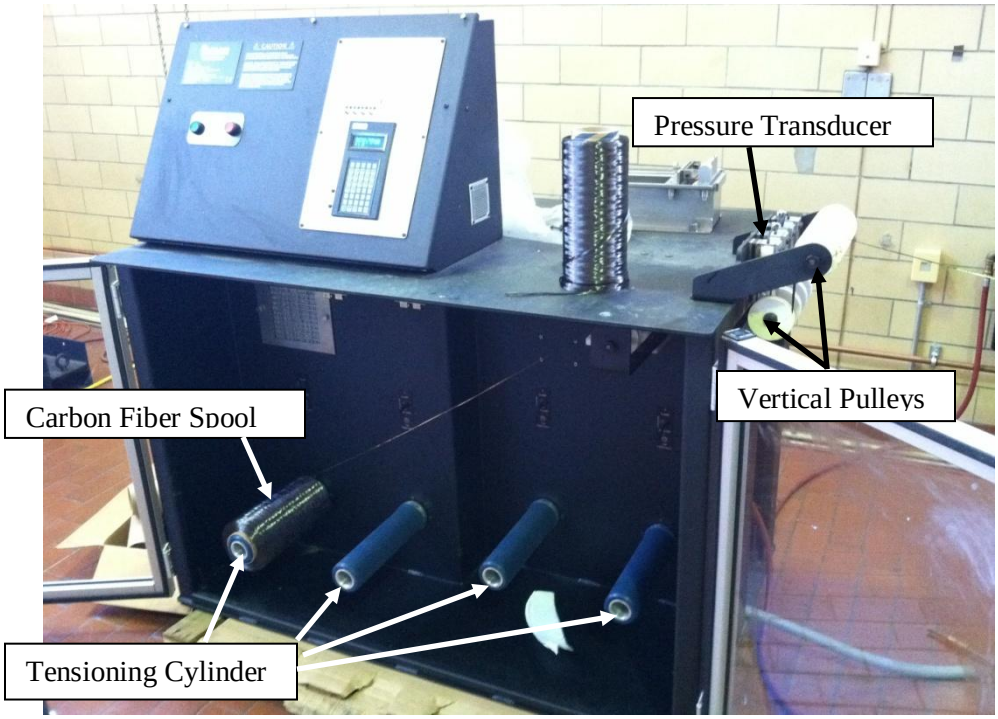

Figure **2-2**: Fiber tensioner cabinet

From the fiber cabinet the carbon fiber tow travels around a third pulley and into the resin bath. During filament winding the resin bath is kept at 50 °C to lower the viscosity of the resin. Heating is mainly necessary for polyurethane resins to reduce the viscosity and decrease the chance of fiber fraying and breakage. The resin bath is shown with half of it missing for illustration (Fig. **2-3**). The carbon fiber tow travels through a back orifice which acts only to guide the fiber through the center of the resin bath. The orifice has a polished steel bore with a precise sized opening. Surfaces with which the carbon fiber tow comes in contact must be polished smooth to avoid fiber fraying. As the tow travels over the polished steel slider bars the tension on the tow spreads the fibers out. This allows the tow to become saturated with resin.

The tow then enters the front orifice of the bath. The target fiber volume fraction of the part is controlled by the diameter of the opening in the front orifice. The target fiber volume fraction, V_{ft}, and the diameter of the front orifice, D_o, are related by equation (14) (Sollenberger 2010).

$$V_{ft} = \frac{D_f^2 N_f}{D_o^2} \tag{14}$$

In equation (10) D_f is the diameter of one fiber (6.7 μm) (Hexcel, 2010), and N_f is the number of fibers in a tow (12,000). In this investigation, the bore of the front orifice has a diameter of 0.965 mm (0.038 in), regulating the amount of resin and fiber by volume in the wet tow to 42% and 58% respectively. The cured part generally has a different fiber volume fraction due to resin drip. The geometric measurements of the cured part can be used to find the approximate fiber volume fraction, V_{fa} using equation (15).

$$V_{fa} = \frac{N_p N_f \pi D_f^2}{2 b_w t} \tag{15}$$

In equation (15) N_p is the number of plies, with each helical layer counting as one ply and each hoop layer counting as one half ply, b_w is the bandwidth, the width of the tow when placed on the mandrel, and t is the thickness of the cured part. When designing a winding program the input bandwidth, b_w, is selected to be slightly smaller than the natural bandwidth of the tow to take into account the uneven spreading of the tow on the mandrel. For this research bandwidth is defined as 2.34 mm (0.092 in) in all filament winding.

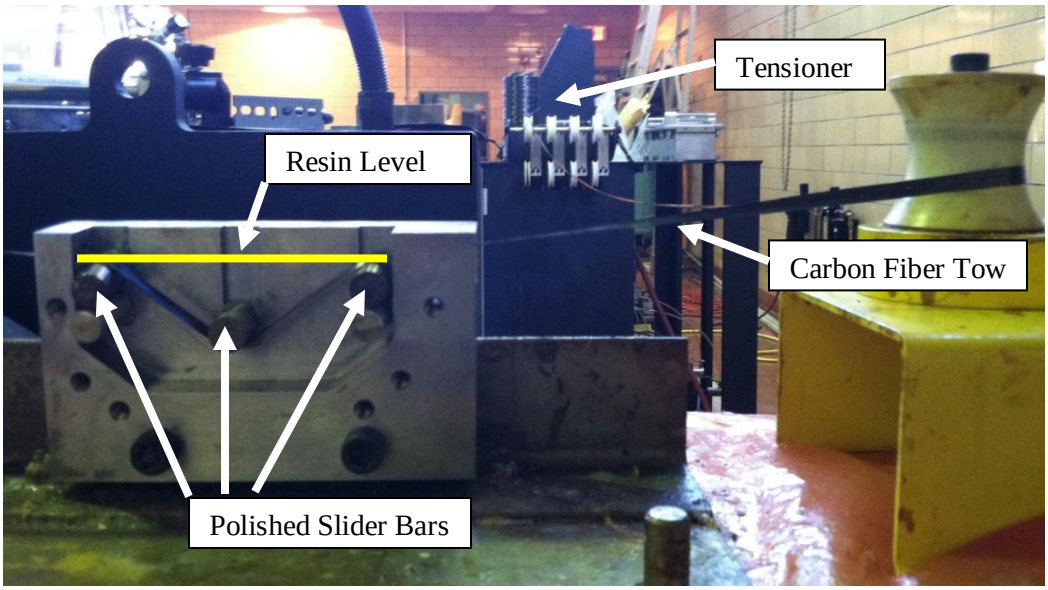

Figure **2-3**: Resin bath and filament winder carriage

The carbon fiber tow exits the resin bath and crosses the payout eye to be deposited on the mandrel. The Superhornet filament winder has four degrees of motion (Fig. **2-4**). Mandrel motion refers to the angular position and speed of the mandrel. Carriage motion refers to the location and speed of the payout eye and resin bath axially along the length of the mandrel. Crossfeed motion refers to the distance the payout eye is away from the mandrel. For a helical or hoop wind program, only mandrel and carriage motion are utilized, while the crossfeed motion is zero. The only time crossfeed motion would need to be non-zero is if the mandrel is not of a constant diameter which is not the case for parts made in this research. The tension on the tow was kept to 4.5-9 N (1-2 lb).

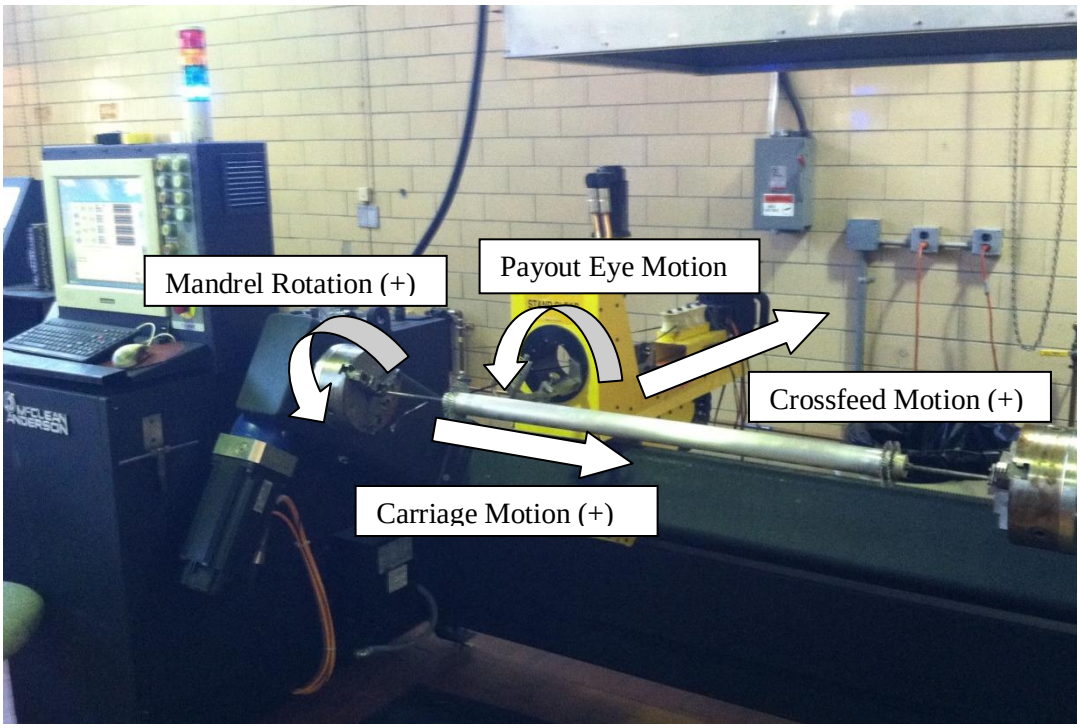

Figure **2-4**: Filament winder front view

Bandwidth, start position, end position, mandrel diameter, fiber angle, turn around range, and dwell angle are necessary parameters for compiling a filament winding program using the program Composite Designer. Start and end positions are user defined, typically a few inches longer than the desired part. Mandrel diameter is a measured parameter. Turn around range is the distance that the payout eye uses to slow down and reverse directions at each end of the mandrel, typically 5 % of the part length. Dwell is the angle that the mandrel rotates while the payout eye is at the end of the carriage travel. For very low angles (<30 deg.) where the tow might slip on the mandrel if unsecured by pin-rings, a dwell of 360° will secure the fiber during carriage motion reversal for small parts. Parts made for compression testing used pin rings to secure the fiber, as is discussed in a separate section of this document.

2.3.1 Plates

For the choice of resin and fiber used in this research project, there were no commercially available pre-impregnated unidirectional composites for use in making flat plates by techniques such as hand layup. Therefore in this research, flat plates were made by wet filament winding carbon fiber tows by the method described previously onto a paddle mandrel (Fig. **2-5**). The hoop winding pattern is used for wet filament winding onto a paddle mandrel. In a hoop pattern, each carbon fiber tow is placed next to the previous carbon fiber tow at approximately 90° relative to the carriage axis. The paddle mandrel has a rectangular cross-section with rounded edges. When designing a winding pattern for use with a paddle mandrel, end position, start position, bandwidth, and mandrel diameter are the required inputs. Mandrel diameter differs from the previous definition in that the user must measure the circumference of the paddle mandrel and convert that number into an equivalent diameter as if the paddle mandrel had a circular cross-section.

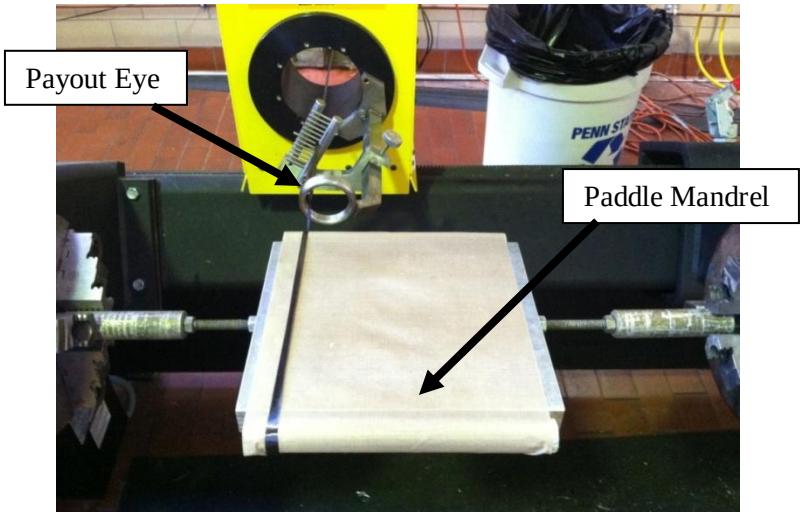

Figure **2-5**: 25.4 cm × 25.4 cm paddle mandrel

The paddle mandrel is covered by non-porous PTFE coated fiberglass peel ply from Airtech (Huntington Beach CA). Specimens for the transverse bending DMA and four-point bending testing are made by wet filament winding a saturated carbon fiber tow onto a 25.4 × 25.4 cm paddle mandrel. The mandrel is covered twice with saturated fiber and covered with another layer of peel ply. The mandrel is held in a 25 ton press and the end of the carbon fiber is cut along a groove on the paddle mandrels rounded edges (Fig. **2-6**). Each unidirectional sheet is cut into two 10.2 cm × 25.4 cm strips.

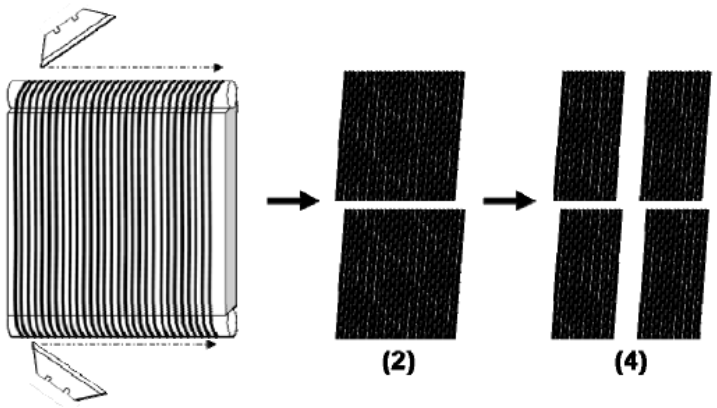

Figure **2-6**: Schematic of the cutting and arranging process of pre-preg in flat specimen mold (Sollenberger 2010)

The four strips are stacked on one another and placed into a mold (Fig. **2-7**) with the peel ply still attached to the top and bottom of the stack of unidirectional sheets. A pre-heated silicone slab is placed on top of the composite and the top of the mold is closed The silicone slab helps to keep even pressure on the composite and also keeps resin from escaping from the mold. Next, the mold is placed in a smart press under 241 kPa (35 psi) of pressure. The smart press then heats the platens according to the necessary cure schedules.

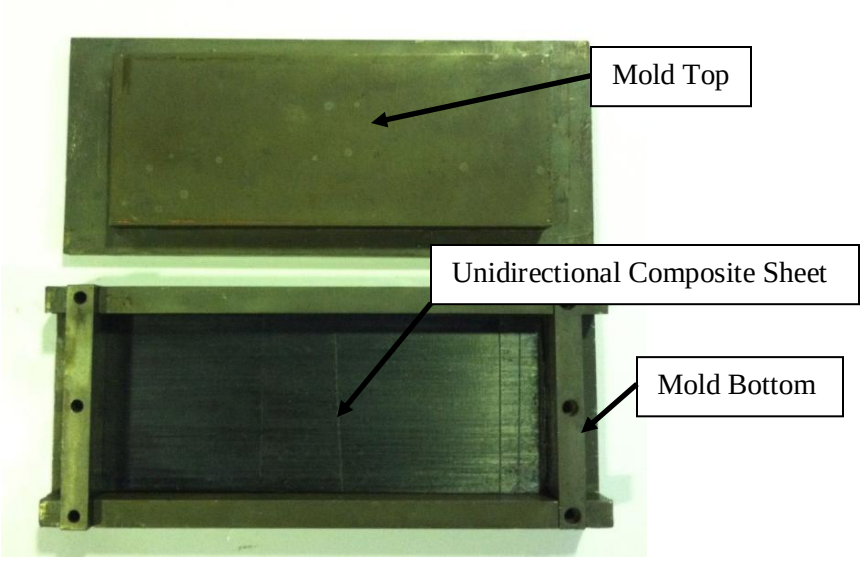

Figure **2-7**: 10.0 cm × 25.0cm plate mold

For transverse bending DMA testing, one specimen of each resin type was cut to the dimensions 60.0 mm × 10.0 mm with carbon fiber reinforcement solely in the width direction. Exact dimensions are listed in Table **2-2**.

Table **2-2**: Description of specimens for evaluating transverse dynamic properties

Matrix Material	Number Tested	Length, mm	Width, mm	Thickness, mm	N_p	V_{fa}
LF750	1	60.0	10.8	2.42	4	0.60
30748	1	60.0	10.4	2.52	4	0.57
30757	1	60.0	9.9	2.43	4	0.60
30917	1	60.0	10.0	2.60	4	0.56
30918	1	60.0	10.3	2.45	4	0.59
EPON 862	1	60.0	8.9	2.04	4	0.71

Four-point bending tests of unidirectional material were used to determine the transverse modulus and tensile strength of the unidirectional composite plate material. For four-point bending testing, three specimens of selected resins were cut to the dimensions 90.0 mm × 12.0

mm × 2.50 mm with carbon fiber reinforcement solely in the width direction. Average dimensions are listed in Table **2-3**.

Table **2-3**: Description of specimens for evaluating F_{2T} and E_2 of beams in four-point bending

Matrix Material	Number Tested	Avg. Length, mm	Avg. Width, mm	Avg. Thickness, mm	N_p	V_{fa}
30748	3	90.0	13.6	2.56	4	0.57
30917	3	90.0	14.1	2.45	4	0.59
EPON 862	3	90.0	11.3	2.07	4	0.70

A larger 35.6 cm × 35.6 cm paddle mandrel was used in making 10° off-axis unidirectional specimens. As with the smaller paddle mandrel, tows were wound on the larger paddle mandrel using a hoop pattern. When the coverage of the paddle mandrel was completed three times, the saturated unidirectional sheets were cut along a groove in the rounded part of the paddle mandrel. The 35.6 cm × 35.6 cm unidirectional sheets were laid atop one another in an aluminum mold with peel ply on the top and bottom of the stack (Fig. **2-8**). The mold was placed in a smart press under the same 241 kPa (35 psi) pressure and heated according to the appropriate cure schedule.

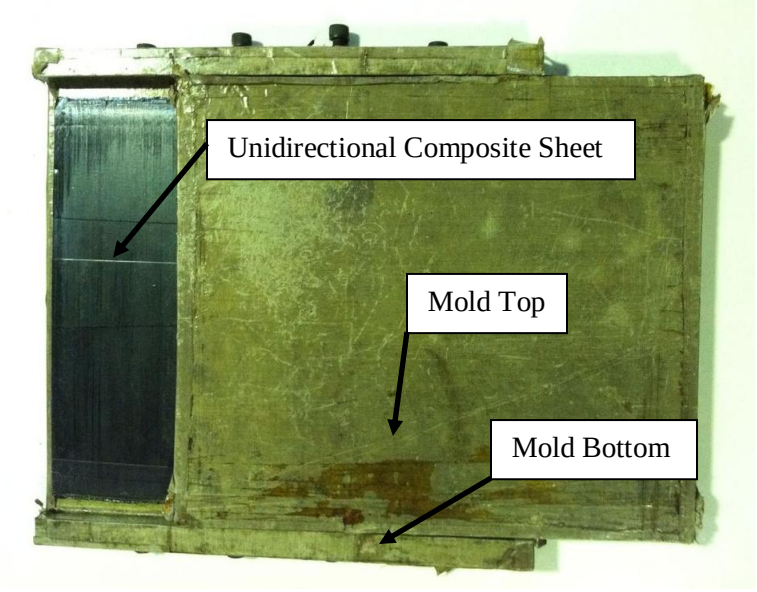

Figure **2-8**: 35.6 cm × 35.6 cm plate mold

After the plate has been removed from the mold, the plate is cut so that the carbon fibers are oriented at 10°, shown by the dotted line in Fig. **2-9**.

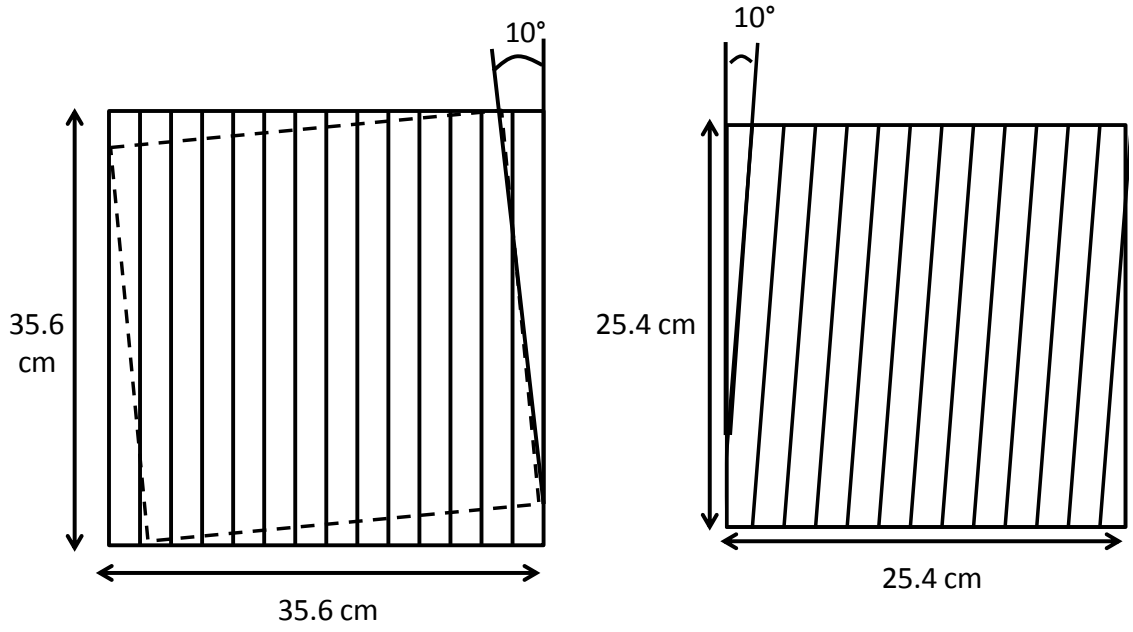

Figure **2-9**: Cutting schematic for 10° off-axis unidirectional specimens

For 10° off-axis testing, three specimens of selected resins were cut to the dimensions 256 mm × 12.5 mm × 1 mm. Average dimensions are listed in Table **2-4**.

Table **2-4**: Description of specimens for evaluating F_6 and G_{12} of beams for 10° off-axis tension

Matrix Material	Number Tested	Avg. Length, mm	Avg. Width, mm	Avg. Thickness, mm	N_p	V_{fa}
30748	3	254	11.5	0.91	1.5	0.60
30917	3	254	14.2	1.15	2	0.63
EPON 862	3	254	13.2	0.90	1.5	0.61

2.3.2 Tubes

Filament wound tubes with helical and/or hoop winding patterns were made using the filament winding process previously described. A helical winding pattern deposits the tow at an angle, relative to the longitudinal axis of the mandrel, chosen by the user as it moves along the carriage direction. When the payout eye reaches the end of the mandrel, the tow is placed at negative that angle, creating a woven architecture. An example of three complete passes of the carriage can be seen in Fig. **2-10**. Filament winding a tube requires the use of a cylindrical mandrel which will become the inner mold for the part. The mandrel is prepared in an identical manner to the neat resin dogbone mold. The mandrel surface is manually abraded using an abrasive pad and then cleaned with acetone removing foreign contaminants. The mandrel is then covered in release agent and baked so that the solvents in the release agent evaporate for thirty minutes at around 140 °C. This process is repeated twice.

To ensure proper fiber placement, pin rings were designed to capture the fiber as it passes the end of the mandrel (Fig. **2-10**). After a tube was wound, two layers of release-coated heat-shrinking tape called Hi-Shrink Tape: Release Coated (25-mm wide, 0.05-mm thick, 80°C

activation temperature) from Dunstone Inc. (Charlotte, NC) was wrapped with 50 % overlap around the composite to provide a smooth outside finish and part consolidation. The shrink tape is drawn taut by hand as tightly as possible, and was secured on both ends by Flashbreaker 2 high temperature tape (Airtech) which has a maximum temperature of 205 °C. For a hoop winding pattern, pin rings are not necessary.

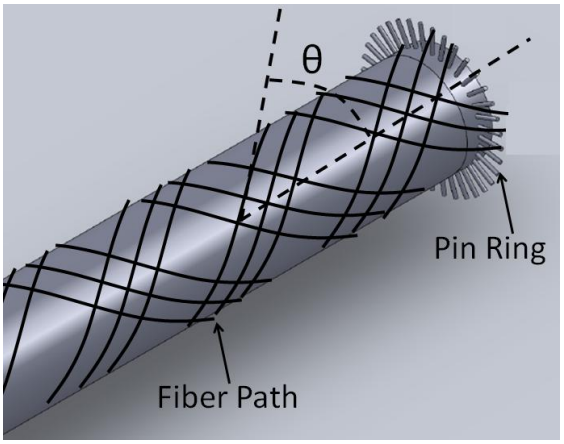

Figure **2-10**: Mandrel and pin ring

A hoop winding pattern was used on a 48.3 mm diameter aluminum mandrel to make specimens for transverse compression testing. The laminate of the part is designated $[89]_n$. Each time the carriage reaches the end of the mandrel the winding program is restarted at the head end so that the fiber angle is always +89 (rather than ±89 in a typical hoop pattern). When sufficient layers have been wound the part is covered with two layers of shrink tape and the mandrel and part are put in the oven at the resin cure schedule. The pin rings are removed before the part is placed into the oven. When the cure schedule is over, the part is removed from the mandrel and specimens are cut to a 7.6 cm length. Average dimensions are listed in Table **2-5**. V_{fa} is calculated with number of plies equal to two.

Table **2-5**: Description of specimens for evaluating F_{2C} and E_{2C} of tubes

Matrix Material	Number Tested	Avg. Radial Thickness, mm	Avg. Inner Diameter, mm	N_p	V_{fa}
30748	5	1.14	48.3	2	0.64
30917	5	1.13	48.3	2	0.64
EPON 862	5	1.13	48.3	2	0.64

Low-angle FMC tubes tested in compression in preliminary work were observed to take on a barrel shape due to the high longitudinal Poisson's ratio of single-angle laminates and the transverse constraint provided by the potted end caps (Fig. **2-11**). It is hypothesized that this barrel shape detracts from the compressive stiffness and modulus of the specimen, potentially biasing the backed out modulus E_1 and strength F_{1c} of the lamina downwards, as well. This barreling should therefore be eliminated by redesigning the laminate.

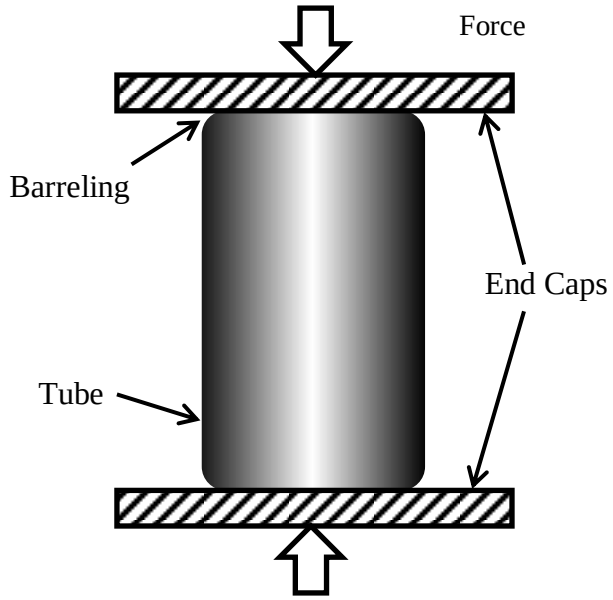

Figure **2-11**: Schematic of barreling of tube during compression test.

Using the AS4/LF750 FMC lamina properties of Sollenberger (2010), CLPT was used to estimate the longitudinal Poisson's ratio, ν_{xy}, of the entire spectrum of possible $[\pm\theta]_2$ angle-ply tubes (Fig. **2-12**), where θ is measured relative to the axial direction of the tube. It can be seen that ν_{xy} can be as high as 4 for a fiber angle near 20 degrees. A simple way to avoid barreling in a $[\pm\theta]_2$ tube is to add a circumferentially wound ply to the laminate. Figure **2-12** also shows ν_{xy} for $[\pm\theta/89/\pm\theta]$ laminates, where 89 deg. is the closest possible angle to 90 deg. because of the way a tow is wound with a finite bandwidth. The Poisson's ratio of an FMC tube with 20-deg. angle plies is reduced by nearly a factor of 10 with the addition of the 89-deg. layer, suggesting that barreling should be mitigated in a compression test. Therefore tubes evaluated in the current investigation were manufactured with a 89-deg. ply in the middle of the laminate.

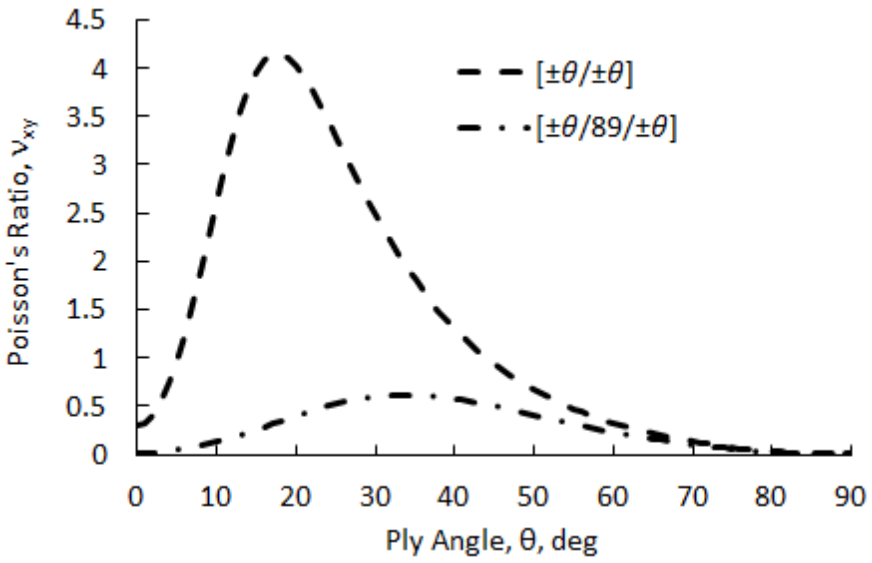

Figure **2-12**: Longitudinal Poisson's ratio, ν_{xy}, versus ply angle, θ, for an FMC tube. Estimated ply properties taken from (Sollenberger, 2010), with E_1 = 145 GPa.

The winding pattern created in specimen fabrication was found to be important by Claus (1994). In the present research, a simple design analysis involving winding pattern was carried out. A single helically wound layer creates adjacent triangular regions of $\pm\theta$ and $\mp\theta$ stacking

sequence in a tube, where the borders of the triangles comprise regions of out-of-plane fiber undulation. Two adjacent triangles are highlighted in Fig. **2-13** for winding patterns of 2, 5, and 10. The pattern number refers to the integer number of highlighted rhombic regions that can be placed side-by-side around the circumference of the tube. Helically wound tubes of the same geometric size and fiber angle can be made with one or more user-selectable patterns.

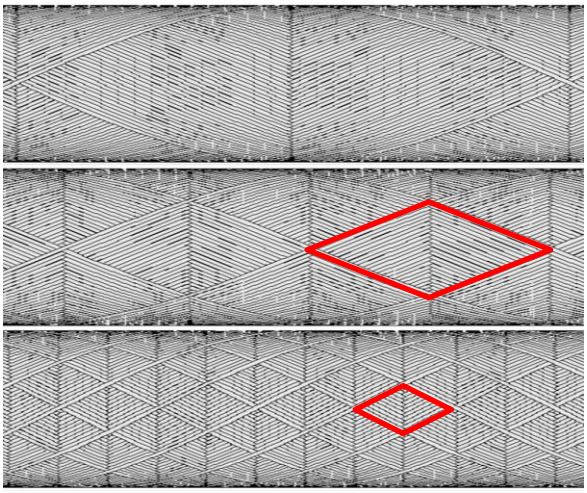

Figure **2-13**: Helical winding pattern of 2 (top), 5 (middle), and 10 (bottom), with rhombic regions highlighted

Considering that pattern is known to have a noticeable effect on the compressive strength of carbon/epoxy tubes (Claus, 1994), this parameter was evaluated in the current investigation as well. Three variations of the $[\pm 22/89/\pm 22]$ layup were used, where 22° is most affected by Poisson's ratio. For a pattern of 2, the filament winder was not able to find a winding solution at 22° for the given geometry. Therefore, 21° was used. The first has a pattern of 2 in the inner and outer helical layers, the second has a pattern of 10 in the inner and outer helical layers, and the third has a pattern of 10 in the inner helical layer and a pattern of 5 in the outer helical layer. A list of specimens for evaluating the effects of winding pattern on the axial compressive strength and modulus of the tubes is shown in Table **2-6**. Only Adiprene LF750 was used to evaluate

pattern effects. Circumferentially wound 89-deg. layers have no winding pattern because the tow is laid alongside itself.

Table **2-6**: Description of specimens for evaluating effects of pattern on axial compressive strength and modulus of tubes.

Matrix Material	Specimen Layup	Number Tested	Winding Pattern	Avg. Inside Radius, mm	Avg. Radial Thickness, mm	N_p	V_{fa}
LF750	[±21/89/±21]	3	[2/2]	48.61	1.74	2.5	0.52
	[±22/89/±22]	3	[10/10]	48.61	1.72	2.5	0.53
	[±22/89/±22]	3	[10/5]	48.61	1.72	2.5	0.53

Compression test specimens for evaluating the fiber direction compression strength and modulus of composite with four different resin materials, F_{1C} and E_1, were wound on a 49.3 mm aluminum mandrel with a helical pattern (Table **2-7**). Again two layers of shrink tape were used on the outside of the tube with the part and mandrel being placed into a convection oven at the corresponding cure schedule. The $[\pm 16/60/\pm 16]$ laminate was selected to explore the effects of using ±60-deg. plies rather than the more commonly used 89-deg. ply adjacent to the strength- and stiffness-dominating ±16-deg. plies. The selection of angles was made between 15° and 45° to give a distribution of tubes in which the axial strength is mostly fiber dominated leading to a better prediction of E_1. The helical plies were fabricated in such a way that the fiber circumferential undulation bands around the circumference should be in line through the thickness. The tubes in Table **2-7** have a pattern of 10 in the inner helical layer and a pattern of 5 in the outer helical layer. The pattern is two times larger on the inside than outside. Thus, only half of the circumferential undulation bands will line up. The number of plies for the fiber volume calculation is identical to Table **2-6.** The estimated fiber volume fraction is larger for EPON 862 compared to the polyurethane resins because EPON 862 is less viscous, resulting in more resin drip off from the part during manufacturing. Using larger amounts of fiber tension, as

was typically done when winding with EPON 862, also causes an increase in the fiber volume fraction.

Table **2-7**: Descriptions of specimens for back calculating F_{1c} and E_1 in tubes.

Matrix Material	Specimen Layup	Number Tested	Avg. Inside Radius, mm	Avg. Radial Thickness, mm	Avg. Helical Ply Thickness, mm	Avg. Middle Ply Thickness, mm	V_{fa}
LF750	[±16/89/±16]	3	48.49	1.60	0.32	0.30	0.57
	[±31/89/±31]	3	48.59	1.68	0.34	0.32	0.54
	[±45/89/±45]	3	48.39	1.68	0.34	0.32	0.54
	[±16/±60/±16]	4	48.44	1.75	0.29	0.29	0.62
30748	[±16/89/±16]	4	48.51	1.45	0.30	0.26	0.62
	[±31/89/±31]	5	48.39	1.47	0.31	0.22	0.62
	[±45/89/±45]	5	48.35	1.59	0.35	0.20	0.57
	[±16/±60/±16]	5	48.40	1.73	0.29	0.29	0.63
30917	[±16/89/±16]	5	48.45	1.38	0.28	0.24	0.66
	[±31/89/±31]	5	48.35	1.39	0.30	0.21	0.65
	[±45/89/±45]	5	48.35	1.39	0.30	0.20	0.65
	[±16/±60/±16]	5	48.36	1.76	0.29	0.29	0.62
EPON 862	[±16/89/±16]	3	48.39	1.22	0.25	0.21	0.74
	[±31/89/±31]	3	48.29	1.30	0.28	0.17	0.70
	[±45/89/±45]	5	48.31	1.32	0.29	0.18	0.69
	[±16/±60/±16]	4	48.31	1.42	0.24	0.24	0.76

2.3.3 Rods

Solid unidirectionally reinforced composite rods were made for measuring the shear dynamic response of all materials systems investigated. Rods were made by drawing the tow through the resin bath. The single saturated tow was drawn through a strip of flexible polyolefin heat-shrink tubing (McMaster Carr, 7496K416), designed to shrink at a 2:1 ratio at 90 °C from a 1.59 mm (1/16 in.) inner diameter to a 0.79 mm (1/32 in.) inner diameter. The polyolefin acts as

the outer molding surface of the tow. A weight was hung at one end of the tow and the other end was tied to a hanging rack in a convection heat oven. After the appropriate cure schedule was completed, the polyolefin was removed from the part by slicing the tubing along the its length with a knife and then peeling it off the specimen. A 10-mm-long specimen was cut from the cured tow. Particular specimen dimensions are listed in Table **2-8**. Fiber volume fraction is calculated by dividing the cross-sectional area of the fibers in a tow by the cross-sectional area of the specimen.

Table **2-8**: Descriptions of specimens for shear dynamic properties

Matrix Material	Number Tested	Diameter, mm	V_{fa}
LF750	1	0.92	0.64
30748	1	0.96	0.58
30757	1	0.89	0.68
30917	1	0.97	0.58
30918	1	0.97	0.58
EPON 862	1	0.89	0.68

2.3.4 Shafts

Composite shafts with LF750, 30917, and EPON 862 matrix materials were made for evaluating self-heating behavior during spin tests. The laminates [±45/±45], [±45/±30], [±30/±45], and [±30/±30] were evaluated at three different speeds (1200, 1800, and 2400 RPM) and various strain amplitudes. Shafts were made by wet filament winding onto a 9.9 mm steel mandrel per the method previously described. When filament winding is finished, shrink tape is applied to the part as before and the part and mandrel were placed into a convection oven at the

appropriate cure schedule. The part is then removed from the mandrel and cut to a 45.7 cm length. Dimensions of shaft specimens are presented in Table **2-9**.

Table **2-9**: Descriptions of shaft specimens for spin testing

Matrix Material	Specimen Layup	Number Tested	Inside Radius, mm	Radial Thickness, mm	N_p	V_{fa}
LF750	[±30/±30]	1	9.91	1.18	2	0.61
	[±30/±45]	1	9.91	1.18	2	0.61
	[±45/±30]	1	9.91	1.18	2	0.61
	[±45/±45]	1	9.91	1.22	2	0.59
30917	[±30/±30]	1	9.92	1.20	2	0.61
	[±30/±45]	1	9.94	1.20	2	0.60
	[±45/±30]	1	9.91	1.20	2	0.60
	[±45/±45]	1	9.92	1.17	2	0.62
EPON 862	[±30/±30]	1	9.92	0.95	2	0.76
	[±30/±45]	1	9.91	0.96	2	0.75
	[±45/±30]	1	9.91	0.98	2	0.74
	[±45/±45]	1	9.94	1.09	2	0.66

Chapter 3

Test Methods

3.1 Quasi-Static

All quasi static testing data was completed in the Composites Manufacturing Technology Center, Room 113 Research West building. Data was acquired using software developed using National Instruments Laboratory Virtual Engineering Workbench (LabVIEW). Version 8.5 was used from all testing except for spin testing which used version 6.1. Voltage from testing instruments was recorded by LabVIEW through a PCI-6200 M Series Multifunction data acquisition system at a rate of 5 Hz except for spin testing which used 1 Hz.

3.1.1 Neat Resin Tension

Neat resin dogbones were tested in tension using a Instron Model 1331 test frame with a 15 kN electronic load cell. A 13.3 kN load card and 76 mm displacement card were used in displacement control. Mechanical wedge grips with serrated faces were used to hold the ends of the specimens. Longitudinal strain, transverse strain, and stress were measured for calculating neat resin modulus and Poisson's ratio. It is important to be aware that the modulus of the flexible matrix material varies depending on the range of strain measured. Two 2.5-cm clip-gages were placed on opposite sides of the specimen along the length to measure longitudinal strain and compensate for bending (Fig. **3.1**). Two 1.25-cm clip-gages were placed on opposite sides of the specimen along the width to measure transverse strain and compensate for bending. Specimens were tested in stroke control such that the longitudinal strain rate was approximately

250 με/s. Three loading cycles were undertaken with material modulus and Poisson's ratio reported for the last cycle. The stress in the specimen is defined by the load divided by the original cross-sectional area. The strain is defined as the clip gage displacement divided by the initial gage length.

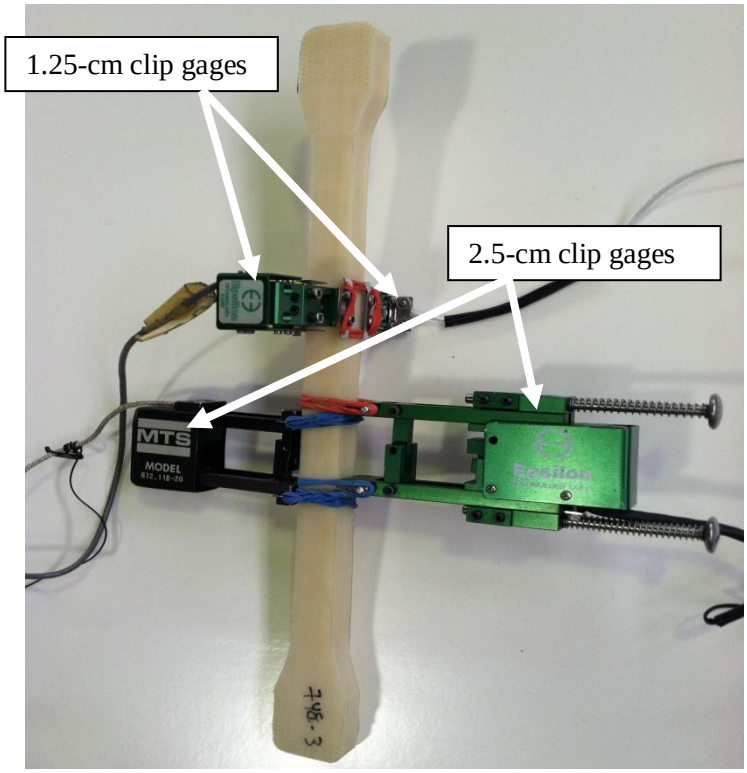

Figure **3-1**: Extensometer arrangement for neat resin dogbone testing

3.1.2 Transverse Flexure of Composite Beam

Four-point bending tests for evaluating static transverse strength, F_{2T}, and static transverse modulus, E_{2T}, of 90° specimens, were conducted using ASTM D 6272. A half-span set-up—i.e., top support span equal to half the bottom support span—was used with an outer span of 72 mm (Fig. **3-2**). The weight of the spreader bar used during the test to make the available three-point fixture into a four-point fixture imparts pre-load and pre strain to the specimen. The

weight of the spreader bar was measured using an electronic scale and accounted for in post-test analysis. Tests were carried out on a MTS 810 test frame. Load was measured with a 445 N electronic load cell. Specimens are assumed to fail in tension due to the compression strength being much higher than the tensile strength (Gibson, 2009; Shan and Bakis, 2009). Longitudinal strain was measured on the top and bottom of the specimen with two CEA-06-125UN-120 linear pattern strain gages from Vishay Precision Group — Micro-Measurements (Wendell NC). The gaging procedure was as follows:

1. Degrease the surface of the specimen with acetone
2. Abrade with M Prep Conditioner A and 120 grit sand paper, wipe clean
3. Wipe clean with M Prep Neutralizer 5A
4. Mark the center location of the specimen for the strain gage
5. Transfer the gage to the specimen using cellophane tape
6. Apply M-Bond 200 Catalyst-C to the gage and specimen, wait 1 minute
7. Apply a small drop of M-Bond 200 adhesive to the specimen
8. Press and hold the gage to the specimen for 2 min. and then peel the tape away at a high angle
9. Apply flux and solder to the gage tabs and attach leadwires

The gages were placed perpendicular to the carbon fiber reinforcement in the composite. The gain of the Measurements Group V2100 bridge/amplifier was adjusted to provide 1000 $\mu\varepsilon = 0.5$ V.

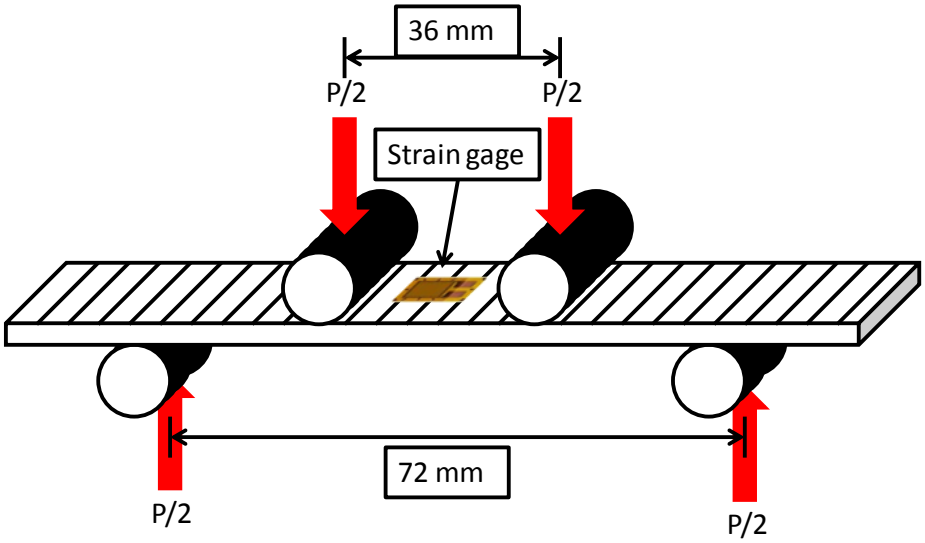

Figure **3-2**: Four-point flexure test set-up

Strain gages were placed on the top and bottom of the beam, in order to measure and compensate for different moduli in tension and compression. The moduli in compression and tension can be calculated by considering the strain, stress, and moment balance in a bimodular beam (Fig. **3-3)**. The strain, ε, is assumed to vary linearly through the thickness and the position of the neutral axis relative to the bottom of the beam is denoted called z_{NA}.

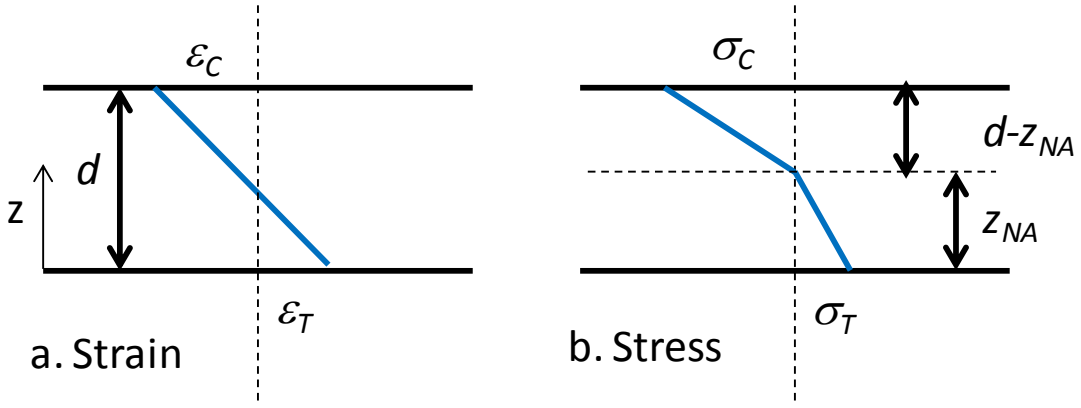

Figure **3-3.** Strain and stress balance in a bimodular material

Relating ε, z, d, ε_T, and ε_C using similar triangles leads to equation (16)

$$z - 0 = \frac{d - 0}{\varepsilon_c - \varepsilon_t}(\varepsilon - \varepsilon_t) \tag{16}$$

Evaluating equation (16) to find an expression of $z_{NA,}$ at which x is zero, yields equation (17).

$$z_{NA} = \frac{d\varepsilon_t}{\varepsilon_t - \varepsilon_c} \tag{17}$$

In equation (17) the only unknown is z_{NA} where ε_c and ε_t are measured during the test and d is the specimen thickness. The two triangular stress distributions must balance each other for axial equilibrium. The force balance yields equation (18).

$$\frac{1}{2}\sigma_t z_{NA} = \frac{1}{2}\sigma_c(d - z_{NA}) \tag{18}$$

Equation (18) can be simplified into equation (19).

$$\frac{\sigma_c}{\sigma_t} = \frac{z_{NA}}{d - z_{NA}} \tag{19}$$

The moment due to the triangular stress distributions must equal the applied moment (Fig. **3-4)**.

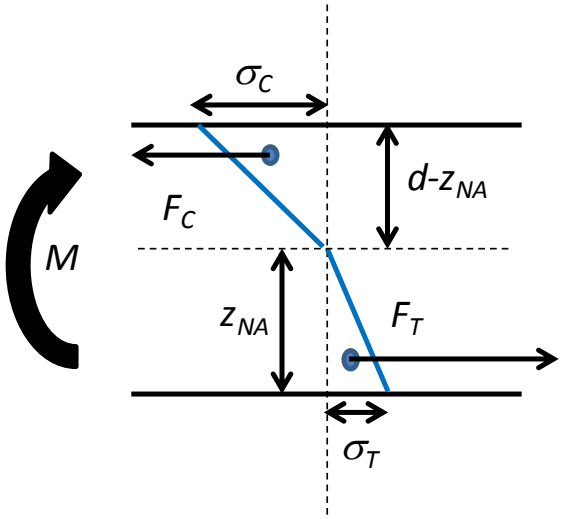

Figure **3-4.** Moment balance in a bimodular material

The resultant forces are described by equations (20a) and (20b)

$$F_c = \frac{1}{2}(d - z_{NA})b\sigma_c \tag{20a}$$

$$F_T = \frac{1}{2} z_{NA} b \sigma_T \tag{20b}$$

where *b* is the specimen width. The moment applied in a four-point bending test with a half-span set-up is equal to half the load divided by a fourth of the outer span. The moment balance is described by equation (21).

$$M = \frac{PL}{8} = \frac{2}{3} F_C (d - z_{NA}) + \frac{2}{3} F_T z_{NA} \tag{21}$$

Substituting equations (20a) and (20b) into equation (21) yields a second relationship between σ_T and σ_C shown as equation (22).

$$\frac{3PL}{8b} = (d - z_{NA})^2 \sigma_C + z_{NA}^2 \sigma_T \tag{22}$$

Using equation 15 to eliminate σ_C from equation (22) yields equation (23) where all variables are known except for σ_T.

$$\sigma_T = \frac{3PL}{8 b z_{NA} d} \tag{23}$$

σ_C can then be found in terms of *P*, by substituting or equation (23) into equation (19).

3.1.3 Shear of Composite

Testing for the determination of the shear modulus, G_{12}, and shear strength, F_6, of the composite material was carried out on an Instron Model 1331 test frame with a 15 kN electronic load cell. Identical to the neat resin dogbone testing, a 13.3 kN load card and 76 mm displacement card were used in displacement control. Mechanical wedge grips with serrated faces were used to hold the ends of the specimens (Fig. **3-5**). Strain was measured on the front and back of the specimen with two CEA-06-062UR-120 rectangular rosette pattern strain gages from Vishay Precision Group — Micro-Measurements (Wendell NC) to measure and compensate for bending.

The surface of the composite was carefully prepared for strain gage adhesion in a manner identical to the four-point bending specimens.

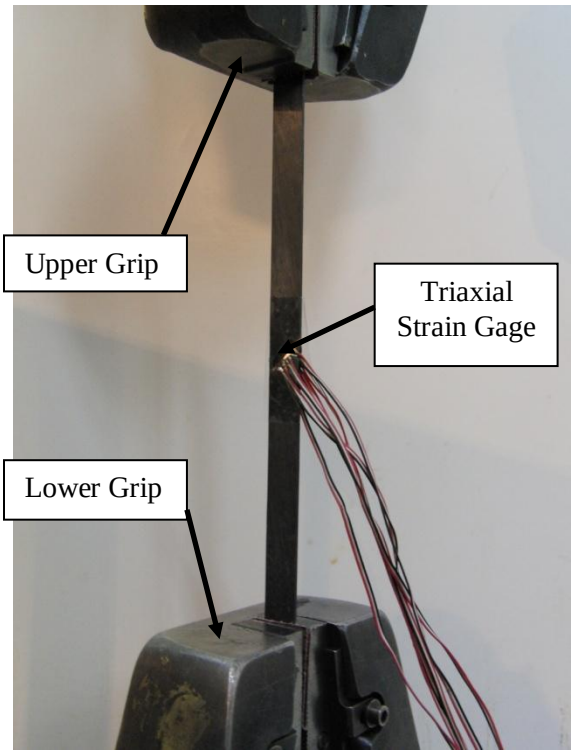

Figure **3-5**: Set-up for 10° off-axis testing

The 10° degree off-axis test was developed by Chamis and Sinclair (1977). A test specimen for measuring shear strength needs to fail in shear. This can be done by testing a unidirectional specimen in which the intra-laminar shear stress is much closer to the failure stress than the other two stresses—i.e, transverse and longitudinal. Chamis and Sinclair (1977) found that this test method had many advantages but that the specimen gage length needs to be at a ratio of 14:1 with the specimen width and that the strain needs to be measured in three directions for subsequent transformation. The shear stress in the laminate can be found from well-known transformation equations presented as equation (24) for an angle of 10°.

$$\tau_{12} = \frac{1}{2}\sigma_x \sin(2\theta) = 0.171\sigma_x \tag{24}$$

The applied stress, σ_{xx}, is found by dividing the applied load by the cross-sectional area of the specimen. The shear strain is related to the structural axis of the specimen by equation (25) for a ply orientation θ.

$$\gamma_{12} = \left(\varepsilon_y - \varepsilon_x\right)\sin(2\theta) + \gamma_{xy}\cos(2\theta) \tag{25}$$

The strains measured by the rectangular strain gage rosette ($\varepsilon_{g1}, \varepsilon_{g2}, \text{and} \varepsilon_{g3}$) are oriented at 0°, 45°, and 90° relative to the longitudinal axis of test specimen. The strains measured by the rosette are related to the structural axes by equations (26),

$$\begin{aligned} \varepsilon_x &= \varepsilon_{g1} \\ \varepsilon_y &= \varepsilon_{g3} \\ \gamma_{xy} &= -\varepsilon_{g1} + 2\varepsilon_{g2} - \varepsilon_{g3} \end{aligned} \tag{26}$$

where ε_g are the strains in the strain gage coordinate system. The relationship between the lamina shear strain and the strains measured by the rosette are found by substituting equation (26) into equation (25) with θ set equal to10 deg., yielding equation (27),

$$\gamma_{12} = -1.282\varepsilon_{g1} + 1.879\varepsilon_{g2} - 0.598\varepsilon_{g3} \tag{27}$$

3.1.4 Longitudinal and Transverse Compression of the Composite

The objective of compression testing is to obtain the transverse strength and modulus, E_{2C} and F_{2C}, as well as the longitudinal strength and modulus, E_1, and F_{1C}. Steel end caps with a circular milled groove (7 mm wide by 5 mm deep) were fitted to the ends of the tubes for compression testing. The grooves were filled with a bismuth alloy (Cerrobend Alloy 158, Bolton Metal Products, Bellefonte, PA) which melts at roughly 70°C and serves as a potting agent for the tubes. This alloy expands as it solidifies, which applies compressive radial stress to the tube and thereby prevents brooming during compression testing. A hemispherical joint is placed in the

load train underneath the test specimen to minimize the introduction of moment loading to the tube. Axial strain is based on the average recorded by two 2.5-cm clip gages attached to the tube on opposite sides. Tensile loading was applied using a screw-driven 267-kN universal testing machine with an electronic load cell using the range 53.4 kN = 10 V for polyurethane and 267 kN = 10 V for epoxy . The cross-head rate was approximately 0.025 cm/min. Specimens were loaded until failure (indicated by a significant drop in the load). Axial stress is defined as the applied load divided by cross sectional area. A typical set-up for measuring F_{1C} and E_{1C} in a helically wound tube is shown in Fig. **3-6.** The testing set-up is identical for hoop wound tubes used for F_{2C} and E_{2C} testing.

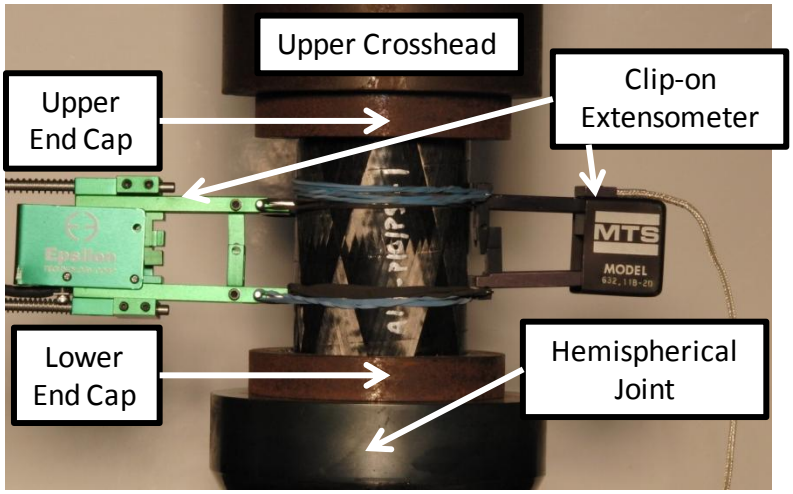

Figure **3-6**: Tube compression test set-up

3.2 Dynamic

3.2.1 Dynamic Transverse Flexure of Composite

Dynamic transverse properties of 90° composites were measured with a Q-800 Series Dynamic Mechanical Analyzer (DMA) made by TA Instruments (New Castle, DE), located in the Wood Chemistry Laboratory in Forest Resources Building at Penn State. The Q800 DMA was used to apply a sinusoidal loading to a beam specimen in a dual cantilever set-up at a constant strain while changing the temperature and frequency. In the dual cantilever set-up the beam specimen has fiber reinforcement in the width direction, perpendicular to the applied stress, and is clamped to the stationary load frame at both ends and at a driveshaft in the center (Fig. **3-7**). Two amplitudes of strain were investigated; 200 με and 1700 με. The temperature was controlled between 20° and 100°C via a heating element or liquid nitrogen. The loading frequency was varied stepwise at 1, 5, 10, 20, 40, 60, and 80 Hz as the temperature increases linearly. The data collected from the bending DMA was used in determining the temperature and frequency dependent properties of the material in transverse loading, (E_2'', E_2', and η_2). The bending DMA is limited to an 18 N force capacity. Mayrides (2005) suggests that the maximum strain in the x-direction that a shaft will encounter is 1500 με. In an optimized design (Roos and Bakis, 2011), that corresponds to a maximum transverse strain of about 1400 – 1800 με. Therefore, the strain amplitude 1700 με was chosen as the transverse strain a helicopter driveshaft might see in operation. The loading frequency 80 Hz, at a strain amplitude of 1700 με, will give a strain rate in the material as close as possible to that of a driveshaft.

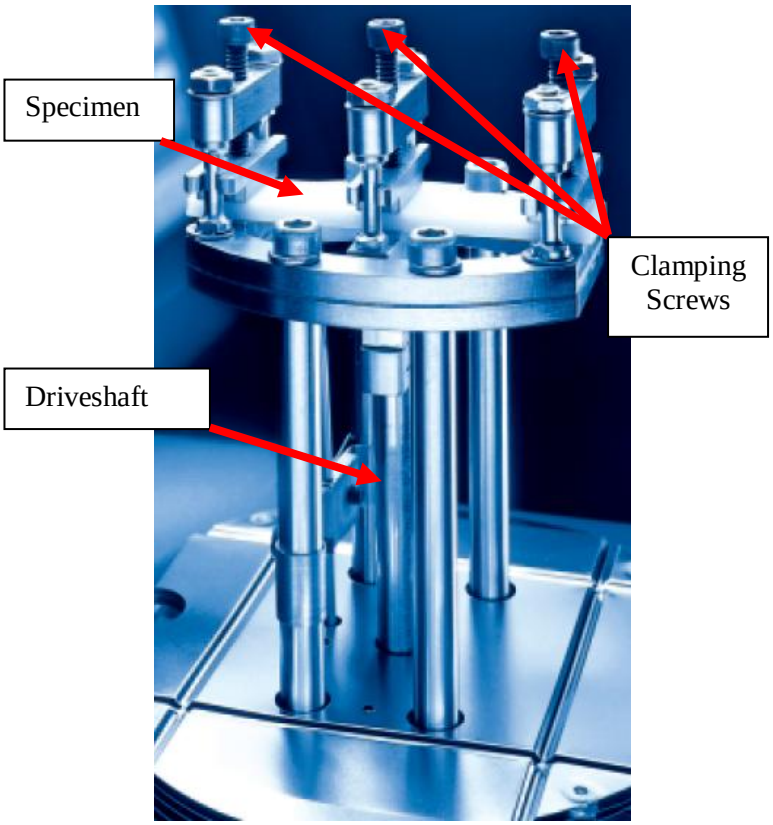

Figure **3-7**: Set-up of dual cantilever DMA test

3.2.2 Dynamic Shear of Composite

Dynamic shear properties of composites were measured using a Dynamic Spectrometer — II (torsional DMA) made by Rheometrics, Inc., located in the Rheometrics Lab in Hostler Building at Penn State. The torsional DMA accepts specimens in a parallel plate geometry. A 1-cm-long rod specimen with reinforcement in the length direction was cut and bonded to grips using EPON 862/ Curative W with 5 % by weight glass microspheres to increase the viscosity of the resin. After bonding the rod into the disk grips (Fig. **3-8**) the gage length of the rod was approximately 1 mm. The actual value was measured with dial calipers. The adhesive was cured at 121 °C (250 °F) for 24 hours.

Figure **3-8**: Top and side view of torsional DMA specimen bonded to its grips

The specimen grips are machined to a precise size so that they will fit into stationary (top) and rotating (bottom) platforms in the torsional DMA which hold the grips with a set screw. Axial and a torsional force transducers are attached to the top platform. The motor applies a dynamic sinusoidally varying shear strain to the rod—in this case 5000 με. The torque cell of capacity 2000 g-cm measures the dynamic shear response ($G'_{12}, G''_{12},$ and η_{12}). Temperature was varied step-wise at 30, 40, 60, 80, and 100 °C and held constant while frequency was varied step-wise at 1, 2, 4, 7, 10, 13, and 15 Hz. Temperature was controlled in an environmentally isolated chamber with cooling via liquid nitrogen and heating through an electrical heating element. A front view of the torsional DMA with the environmental chamber closed is presented in Fig. **3-9**. The maximum shear strain amplitude in a helicopter driveshaft is approximately 3500 με for a flexural strain of 1500 με (Roos and Bakis, 2011). The torsional DMA is unable to reach higher frequencies, i.e. 80 Hz, so shear strain amplitude for the test was chosen to be 5000 με to have the shear strain rate in the experiment and application be similar (Appendix B).

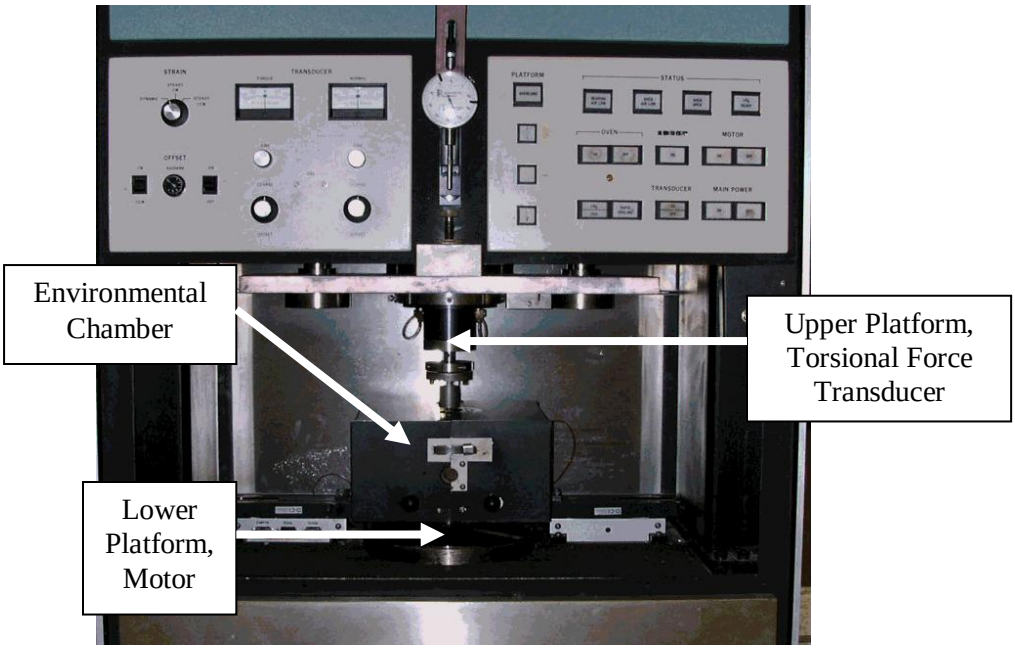

Figure **3-9**: Front view of the torsional DMA

3.2.3 Spin Testing of Shafts

A custom rig for spin testing misaligned tubes was built by Dr. Ying Shan as part of his previously completed PhD work at Penn State (2006). The shaft is glued into steel end grips with Devcon Plastic Welder (ITW Devcon, Danvers MA) a methacrylate glue that cures at room temperature within 24 hours. The end grips protrude 38 mm (1.5 in) into each end of the shaft, leaving a free length of 38.1 cm (15 in). The shaft being tested is designed to be in pure bending, uniform strain, as long as the free length of the tube and the tail stock position are precise. The tail stock of the rig is moved to pre-determined positions in order to apply different strains. The end fixtures attached to the shaft are placed into sets of two roller bearings at the headstock and tailstock side (Fig. **3-10**) of the rig.

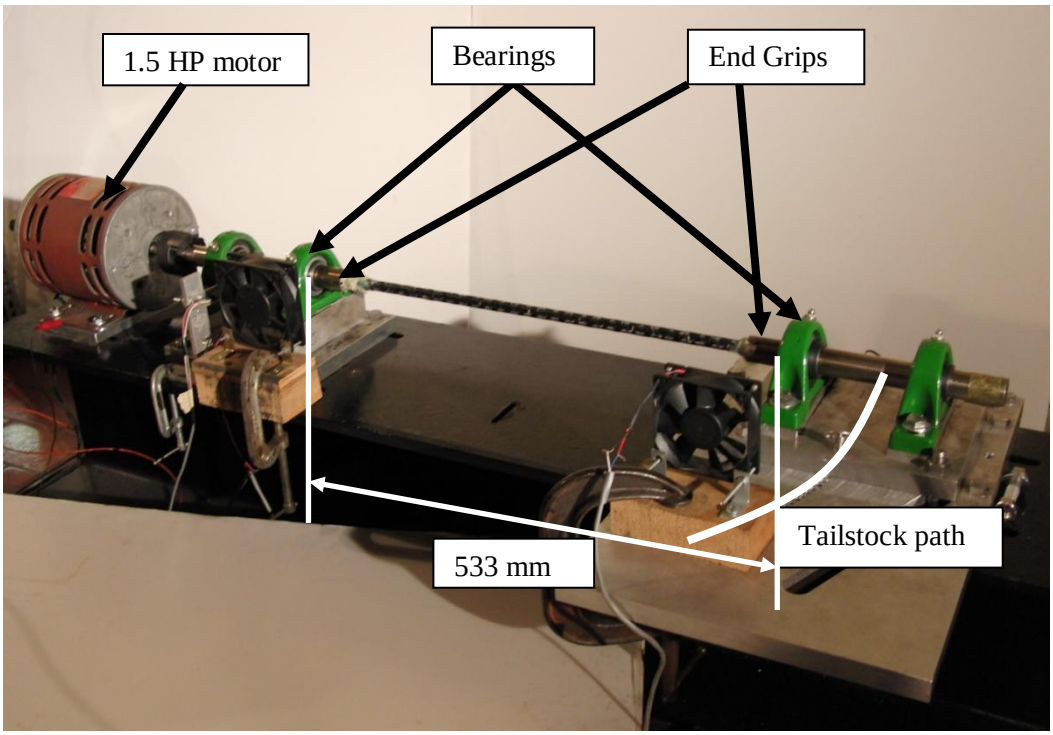

Figure **3-10**: Front view of spin rig

The shaft is driven by a 1.5 HP motor without any braking torque. Before testing, the strain on the misaligned shaft is measured using a 2.5-cm clip gage at five locations along the length from quarter span on the left to quarter span on the right. Strain in compression and tension is measured by attaching and zeroing the gage when the shaft is in the straight configuration and then moving the tailstock to various other locations. A tachometer measures rotational speed by sensing differences in reflectivity between light and dark surfaces on the driveshaft. Three infrared thermocouples are used to measure temperature. The first is fixed at the left quarter span and the second is fixed at the midspan (Fig. **3-11**). The third infrared thermocouple was manually positioned to measure shaft temperature at the 3/8, 5/8, and 3/4 span locations. A J-type thermocouple was used to measure ambient room temperature.

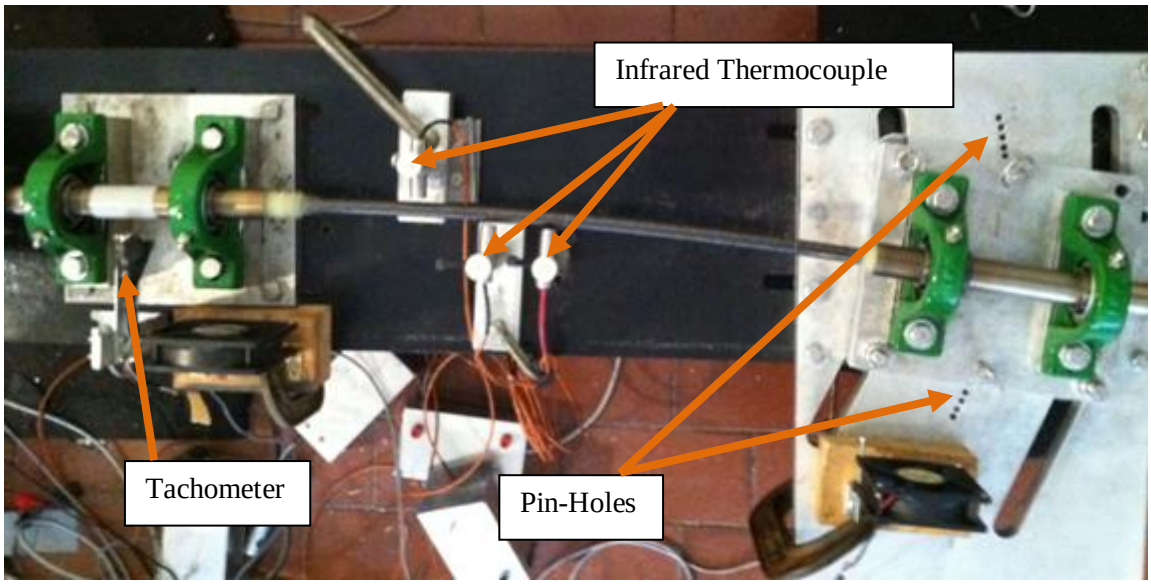

Figure **3-11**: Top view of spin rig

Chapter 4

Quasi-Static Test Results

4.1 Neat Resin Tension

During neat resin testing, two 2.5-cm clip gages were used to measure and compensate for longitudinal and transverse bending. There was little observed bending in the specimens, as seen by good agreement between the left and right longitudinal clip gages (Fig. **4-1**) and the front and back transverse clip gages (Fig. **4-2**).

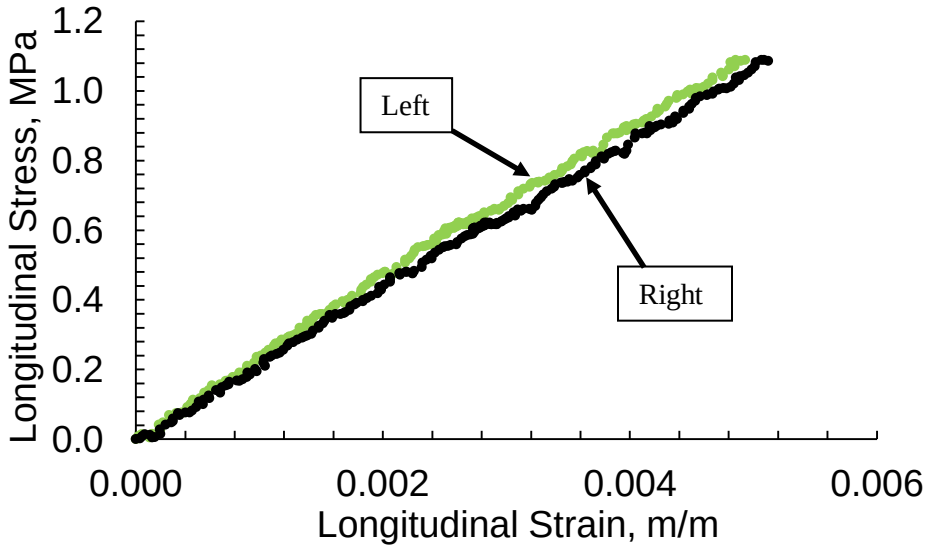

Figure **4-1**: Longitudinal stress vs. longitudinal strain — neat LF750 Specimen 3, first loading cycle

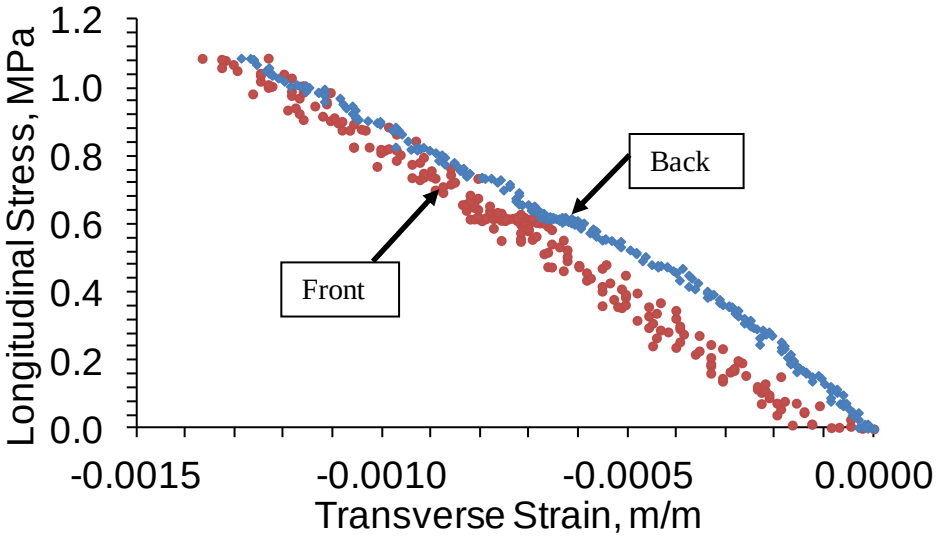

Figure **4-2**: Longitudinal stress vs. transverse strain — neat LF750 Specimen 3, first loading cycle

Neat resin specimens were loaded in displacement control to around 1 % and returned to zero three times. This was to ensure that the modulus (Fig. **4-3)** and Poisson's ratio (Fig. **4-4**) of the material exhibits the same response after multiple loadings. The second and third loadings have approximately the same longitudinal stress versus longitudinal strain response.

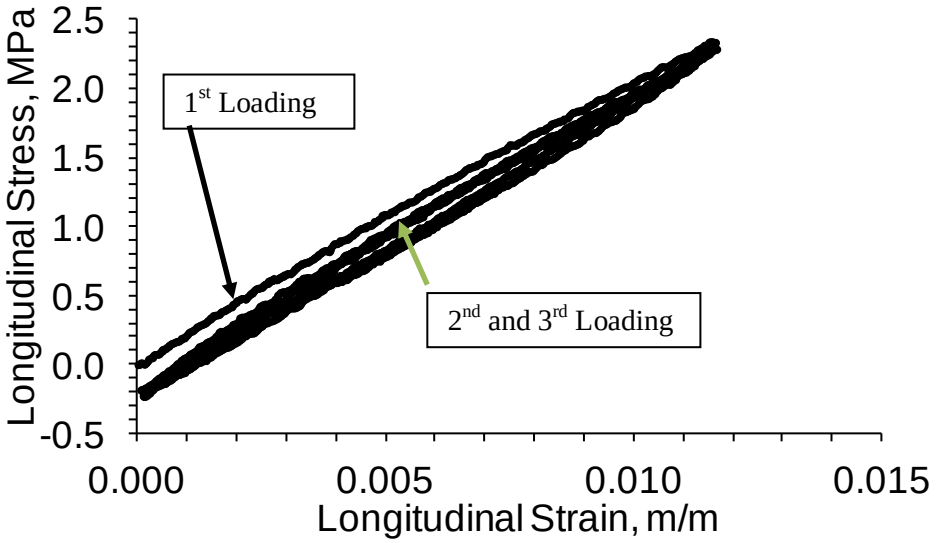

Figure **4-3**: Longitudinal stress vs. longitudinal strain — neat LF750 Specimen 3, all loading cycles

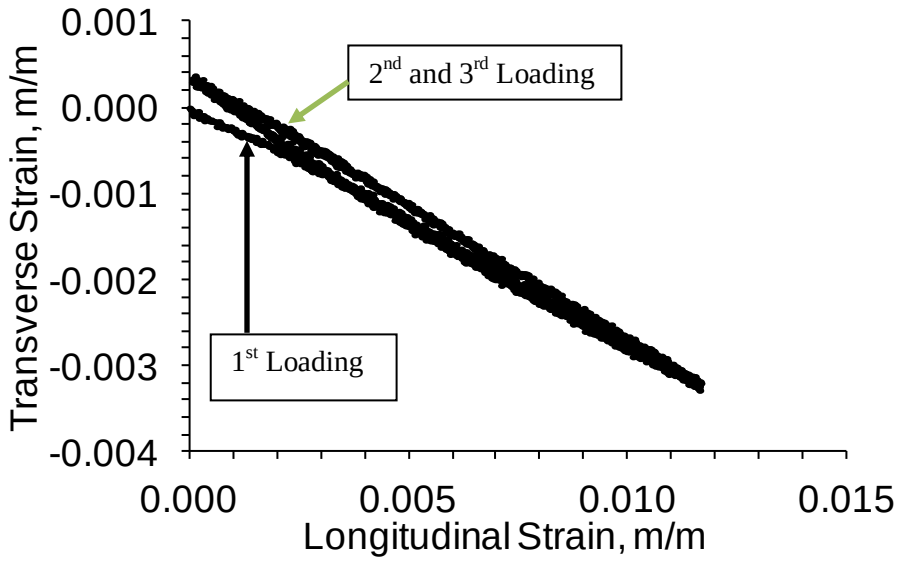

Figure **4-4**: Transverse strain vs. longitudinal strain — neat LF750 Specimen 3, all loading cycles

The modulus of the material was found from the third loading cycle of the material. A line was fit to longitudinal strain, 0 – 500 με (solid), 500 – 1000 με (dotted), 1000 – 2000 με (dashed), and 2000 – 10000 με (double solid) (Fig. **4-5**). The modulus of the resin is highly dependent on the strain range chosen, decreasing approximately 33 % from the 0 – 500 με range to the 2000 – 10000 με range in this case. In a helicopter driveshaft application, the shaft is likely to experience anywhere between 1500 – 1800 με longitudinal strain, at most (Mayrides et al., 2005). For that reason, the neat resin modulus used throughout this investigation is the value fit to the stress-strain curve in the 1000 – 2000 με range.

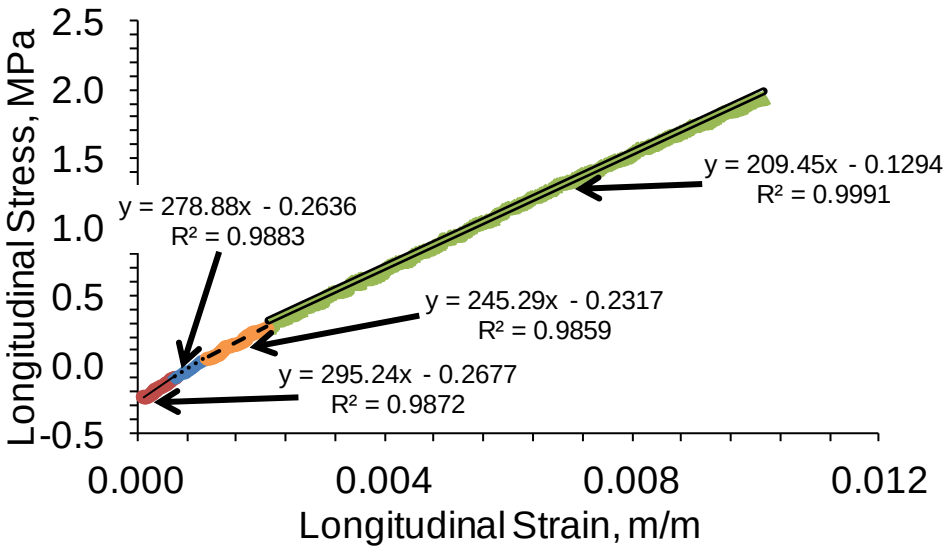

Figure **4-5**: Young's modulus of LF750 Specimen 3 in various strain ranges, third loading cycle

The Poisson's ratio of the material was found from the third loading cycle of the material. A line was fit to longitudinal strain in the 0 –1000 με range (Fig. **4-6**), indicated by dashed green points, because the Poisson's ratio was fairly constant over all strains investigated. Neat resin dogbone tests were carried out in a similar manner for all of the other resins. The results are tabulated in Table **4-1**. In general, the materials under investigation were found to become stiffer and more linear with subsequent loadings. Materials were also found to be less stiff as the strain range under consideration was increased.

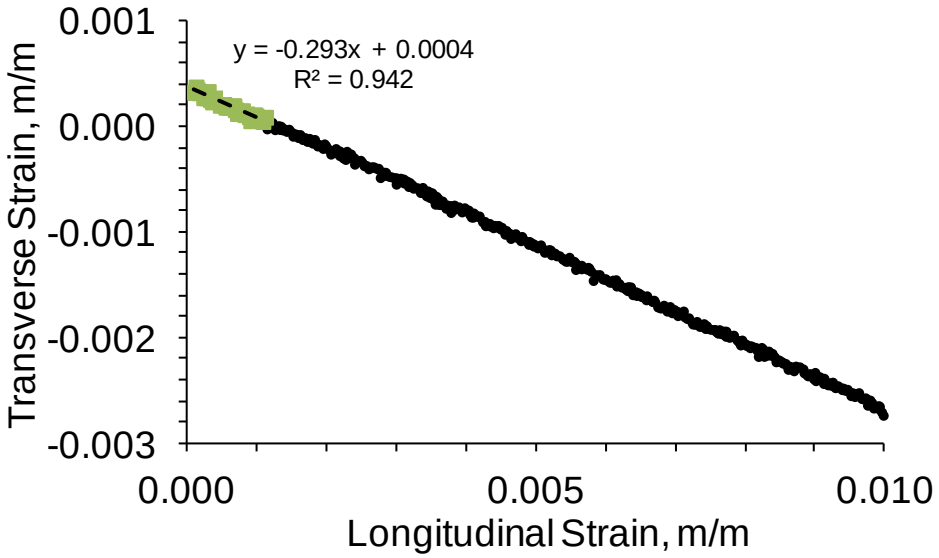

Figure **4-6**: Poisson's ratio of LF750 Specimen 3, third loading cycle

Table **4-1**: Neat resin dogbone modulus and Poisson's ratio results

Resin Material	First Cycle Modulus, MPa			Second Cycle Modulus, MPa			Third Cycle Modulus, MPa				Poisson's Ratio	Average Modulus, MPa		Average Poisson's Ratio	
	(a)	(b)	(d)	(a)	(b)	(d)	(a)	(b)	(c)	(d)	0-1000 με	(c)	C_V, %	0-1000 με	C_V, %
LF750-1	230	239	202	270	253	209	282	269	241	211	0.34	245	2.24	0.32	7.33
LF750-2	247	227	205	292	278	216	289	268	251	213	0.32				
LF750-3	223	212	199	279	262	211	295	279	243	209	0.29				
748-1	531	489	417	575	540	434	559	540	521	435	0.33	510	2.22	0.36	10.02
748-2	524	518	415	555	562	431	560	557	498	434	0.40				
748-3	480	473	424	576	533	441	576	552	510	445	0.34				
757-1	995	856	768	1038	858	799	1026	849	875	803	0.40	887	1.38	0.39	4.55
757-2	872	846	751	947	815	788	914	826	886	789	0.40				
757-3	961	773	775	896	815	793	888	812	899	793	0.37				
917-1	1080	879	820	1050	879	837	1140	892	957	833	0.35	976	4.83	0.33	9.6
917-2	1050	866	824	992	848	838	1040	836	942	793	0.30				
917-3	712	1081	817	1010	1049	802	1040	1030	1030	788	0.35				
918-1	707	929	754	837	802	734	898	800	834	724	0.41	850	2.76	0.37	7.67
918-2	823	918	749	929	781	727	911	833	840	719	0.36				
918-3	877	774	771	910	819	755	910	741	877	747	0.36				
862-1	3070	3050	2840	3200	3090	2880	3230	3270	2930	2880	0.34	2950	1.89	0.38	11.42
862-2	2600	2950	2740	2700	2800	2750	2720	2930	2920	2930	0.36				
862-3	3080	3250	2760	2680	3100	2800	2880	3060	3020	2770	0.43				
Note: (a) 0 – 500 με, (b) 500 – 1000 με, (c) 1000 – 2000 με, and (d) 2000 – 10000 με															

The strength factors that most often limit the feasibility of an FMC as a helicopter driveshaft material are the transverse tensile strength, F_{2T}, and fiber direction compressive strength, F_{1C} (Roos and Bakis, 2011). It is important to also consider the materials dynamic characteristics which contribute to self-heating during cyclic loading. It is hypothesized that F_{2T} and F_{1C} are both related to E_m. This hypothesis is investigated in the subsequent sections. The polyurethane resin with the largest value of E_m is 30917 (Fig. **4-7**).

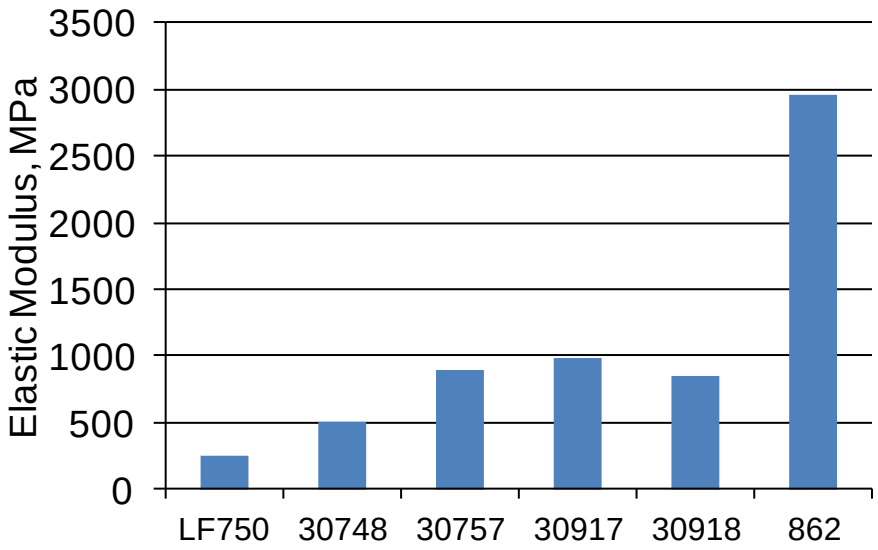

Figure **4-7**: Elastic modulus for all resins — third loading cycle, 1000 – 2000 με range

4.2 Composites

4.2.1 Transverse Flexure of Composite

Quasi static four-point bending tests were conducted on unidirectional composites made with 30748, 30917, and EPON 862 resin to determine E_{2T} and F_{2T}. These resins were chosen because they represent a large range of E_m values. The strain on the tension as well as the

compression side of the specimen was measured for later compensation by the method described in Section 3.1.2. Modulus of the material, E_2, was found by fitting a line to the 1000 – 2000 με region of the stress-strain curve after taking into consideration possible bi-modular behavior. Failure is demarked by a transverse crack propagating across the width of the specimen on the tension strain side (bottom) of the specimen (Fig. **4-8**). The failure point was typically at or in between the inner loading points where bending moment is maximized.

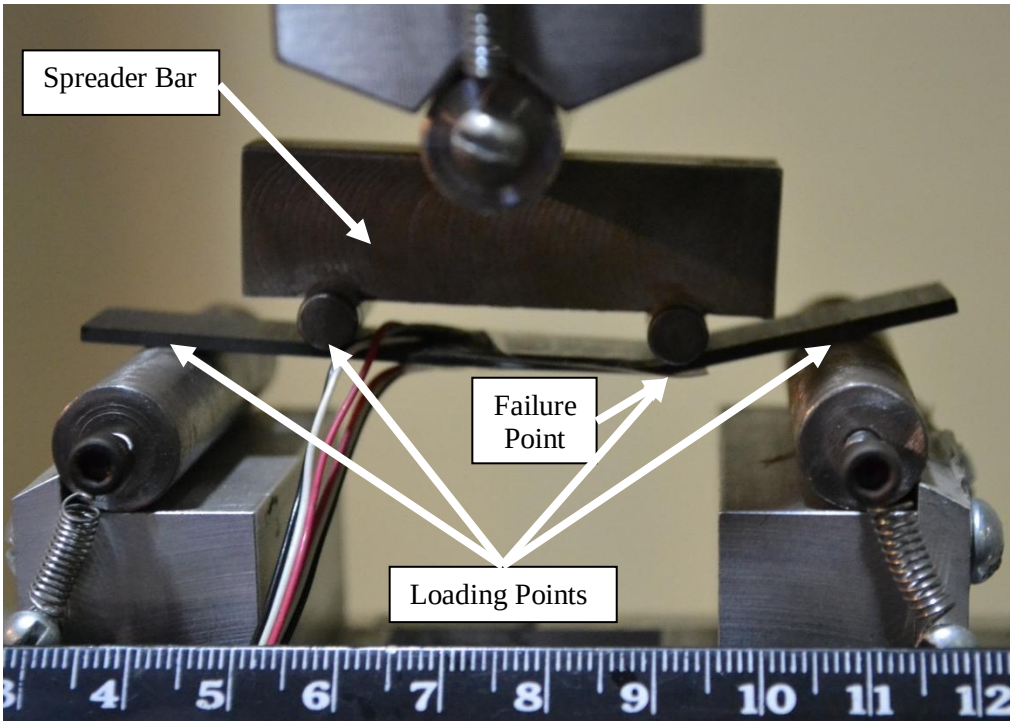

Figure **4-8**: Photograph of failed four-point bending specimen

Tensile and compressive stress-strain responses of the material measured during a typical four-point bending test, shown in Fig. **4-9** and Fig. **4-10**, respectively, revealed that the compression modulus is typically slightly higher than the tension modulus. The 1000-2000με linear fit is based on the points highlighted.

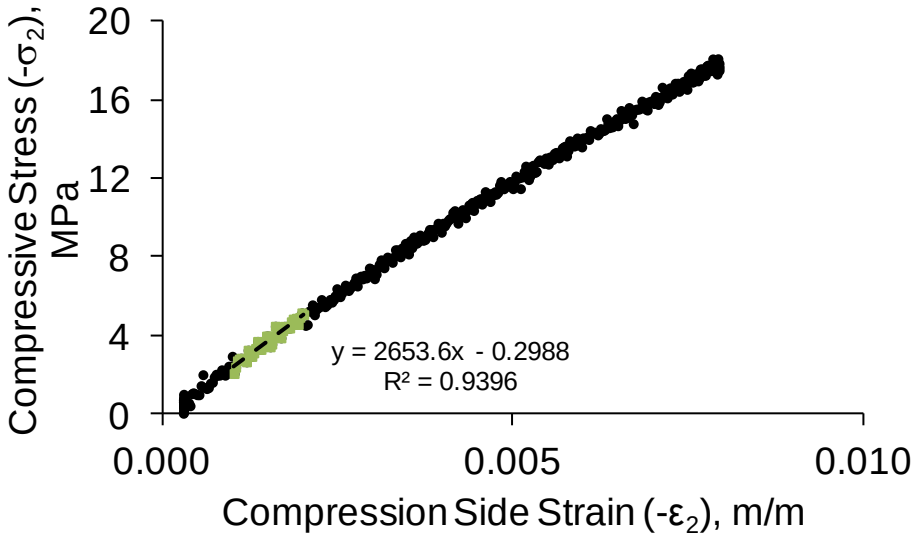

Figure **4-9**: Typical four-point bending compressive stress vs. compressive strain — 30748 Specimen 1

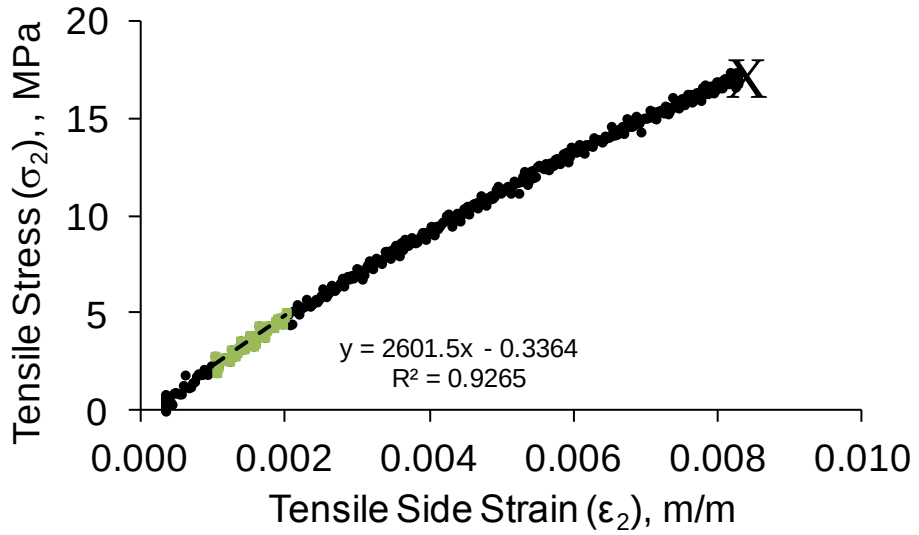

Figure **4-10**: Typical four-point bending tensile stress vs. tensile strain — 30748 Specimen 1

The correction for bimodular behavior is made using the method described in Section 3.1.2 on a point by point basis, given that the only unknowns are compression and tensile strain and load which are measured quantities. The ultimate transverse tensile strength, F_{2T}, is the highest tensile stress achieved before failure, marked in Fig. **4-10** with an "X." Ultimate

transverse tensile strain is the largest value of tensile strain before failure. Strength and modulus results for the three resins tested are listed in Table **4-2**. There was no compression strain gage used for EPON 862 tests due to there not being a large difference in compression and tensile moduli for the previously-tested 30748 and 30917 composites. The transverse tensile strain at failure was found to be smaller for 30917 than for EPON 862. This is an interesting observation as it suggests that 30917 is more like a rigid matrix than a flexible one. It should be noted that the sizing on the fiber is meant for an epoxy matrix and there could be a weak bond between the fiber and polyurethane resin. Gibson (2007) reports 9.0 GPa and 48.3 MPa as typical modulus and strength values for a AS/3501 composite which is very similar to the values found in this investigation for AS4D/EPON 862.

Table **4-2**: Four-point bending modulus and strength results

Resin Material	Transverse Tensile Modulus, E_{2T}, GPa	Avg.	C_v (%)	Transverse Compression Modulus, E_{2C}, GPa	Avg.	$C_{v,}$ %	Transverse Tensile Strength, F_{2T}, MPa	Avg.	$C_{v,}$ %	Transverse Tensile Strain, ε_T, με	Avg.	$C_{v,}$ %
748-1	2.60	2.38	8.53	2.65	2.38	9.73	17.4	17.4	1.81	8270	8680	4.22
748-2	2.20			2.27			17.7			8810		
748-3	2.34			2.23			17.1			8970		
917-1	5.14	5.26	2.51	5.49	5.35	4.06	22.2	23.0	6.88	5000	4720	7.89
917-2	5.40			5.10			24.9			4860		
917-3	5.23			5.46			22.0			4300		
862-1	9.10	9.09	0.66	N/A	N/A	N/A	48.2	46.7	3.00	5190	5260	0.90
862-2	9.15			N/A	N/A	N/A	46.3			5150		
862-3	9.03			N/A	N/A	N/A	45.5			5100		
Note: strain range 1000-2000 με												

4.2.2 Shear of Composite

Shear tests for G_{12} and F_6 using the 10° off-axis tests were conducted as described in Section 3.1.3 on composites made with 30748, 30917, and EPON 862 resins. Shear modulus of the material, G_{12}, was found by fitting a line to the 3000 – 4000 με region of the shear stress-shear strain curve because 3000 με is a typical amount of shear strain an FMC shaft with typical ply angles might encounter during operation (Mayrides, 2005; Roos and Bakis, 2011). This value is found by using the optimization code developed by Roos and Bakis (2011) and finding the maximum γ_{12} in the optimized shaft. Failure is typically demarked by a crack propagating along the fiber direction in the gage section (Fig. **4-11**).

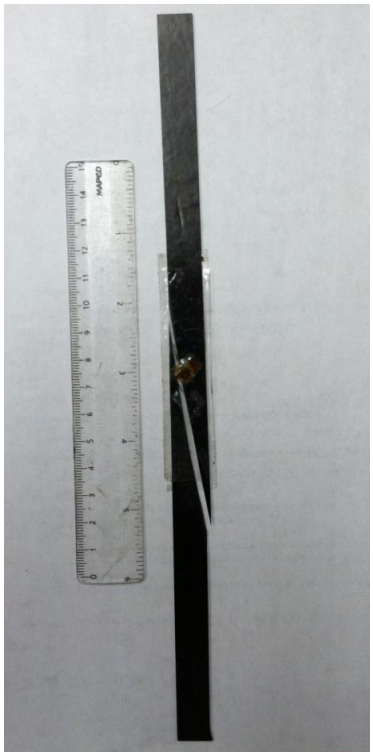

Figure **4-11**: Photograph of a typical failed 10° off-axis tension specimen

The ultimate shear strength, F_6, is the highest stress achieved before failure, marked with an "X" in Fig. **4-12**. The ultimate shear strain is the highest strain achieved before failure. Shear strength and modulus results for the three composites tested are listed in Table **4-3**. The shear strain to failure of both of the polyurethane FMCs is much higher than the epoxy composite. On the other hand, ultimate shear strength of the FMCs is much lower than that of the epoxy composite. Gibson (2007) reports values of 6.9 GPa and 62.1 MPa as typical modulus and strength values for a AS/3501 composite which is very similar to the values found in this investigation for AS4D/EPON 862.

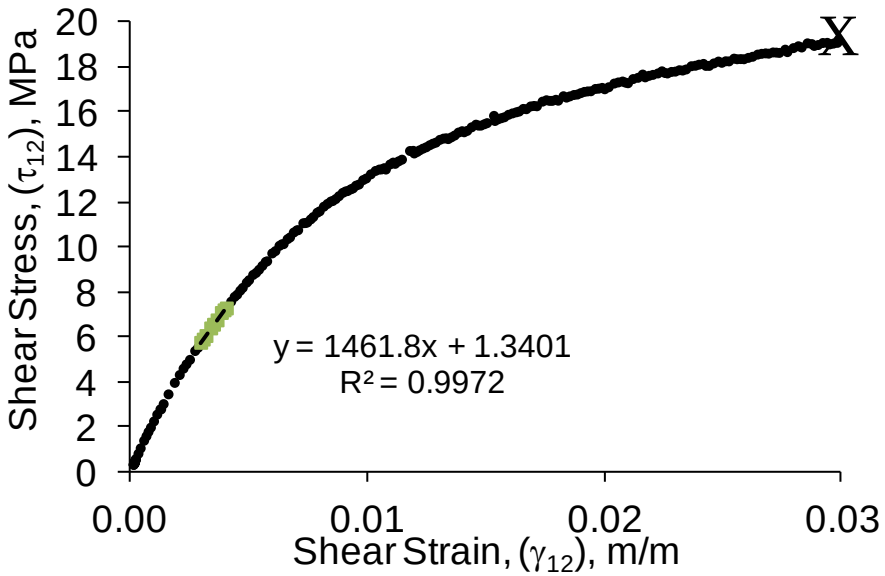

Figure **4-12**: Typical shear stress vs. shear strain — 30748 Specimen 1

Table **4-3**: 10° off-axis modulus and strength results

Resin Material	Shear Modulus, G_{12}, GPa	Avg.	C_v, %	Shear Strength, F_6, MPa	Avg.	C_v, %	Shear Strain, γ_{12}, με	Avg.	C_v, %
748-1	1.46	1.45	9.64	19.5	19.6	0.63	31100	29000	9.64
748-2	1.59			19.6			25800		
748-3	1.31			19.7			30100		
917-1	1.99	1.88	10.1	24.0	23.9	5.50	21200	23500	19.8
917-2	1.66			22.5			28800		
917-3	1.99			25.2			20400		
862-1	6.90	6.64	6.74	59.1	54.8	10.1	9840	9030	7.98
862-2	6.12			48.6			8460		
862-3	6.89			56.6			8800		
Note: strain range 3000-4000 με									

4.2.3 Transverse Compression of Composite

Compression tests were conducted on hoop-wound tubes to determine E_{2C} and F_{2C} of composites made with 30748, 30917, and EPON 862 resins according to Section 3.1.4. Axial modulus of the tubes, E_{2C}, was found by fitting a line to the 1000 — 2000 με region of the stress-strain curve. Failure is demarked by an "X" at a significant drop in load (Fig. **4-13**).

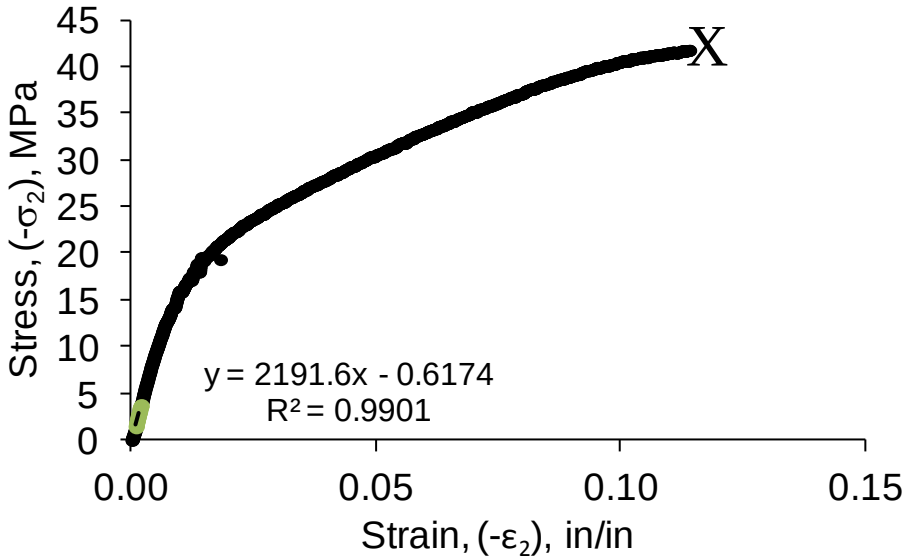

Figure **4-13**: Typical axial stress vs. strain for hoop-wound tube — 30748 Specimen 3

The ultimate compressive strength, F_{2C}, is the highest stress achieved before failure, marked in Fig. **4-13** with an "X." Strength and modulus results for the three resins tested are listed in Table **4-4**. The failure mode is a fiber direction crack propagating around the circumference. The transverse modulus, E_{2C}, found from hoop wound compression is approximately 5 % lower than that found by four-point bending in the strain range of 1000-2000 με. The modulus from hoop wound compression is used as E_2 for later use in this research because the hoop wound compression specimen is more representative of a driveshaft, being that it is a cylinder and not a beam, and is also more conservative in design.

Table **4-4**: Compression moduli and strengths from hoop-wound tubes

Resin Material	Transverse Comp. Modulus, E_{2C}, GPa	Avg.	C_v, %	Transverse Comp. Strength, F_{2C}, MPa	Avg.	C_v, %	Transverse Comp. Strain, ε_2, με	Avg.	C_v, %
748-1	2.24	2.28	8.69	39.4	39.3	5.8	101000	99200	13.9
748-2	2.63			41.2			107000		
748-3	2.19			41.8			114000		
748-4	2.15			38.2			94600		
748-5	2.19			36.2			79600		
917-1	4.69	4.73	3.99	48.5	50.3	3.81	16300	19300	11.8
917-2	4.79			48.0			19100		
917-3	4.54			51.5			22400		
917-4	4.60			51.0			20500		
917-5	5.02			52.4			18400		
862-1	8.55	8.56	2.65	139	131	4.32	19000	18300	4.21
862-2	8.47			134			18500		
862-3	8.79			125			17600		
862-4	8.23			128			19000		
862-5	8.75			128			17400		
Note: strain range 1000-2000 με									

The averaged ply elastic properties found so far through experimental testing, other than E_1, are summarized in Table **4-5**. The values for LF750 are taken from Sollenberger (2010). Poisson's ratio, the average from Table **4-1** for the resin and 0.28 for the fiber (Hexcel), is calculated using the RoM and E_2 and G_{12} are from Tables **4-4** and **4-3** respectively. The fiber volume fraction used is the average from the tube compression tests (Table **2-6)**. The remaining ply elastic property, E_1, is found in Section 4.2.5 by a back-out method based on CLPT and experimental results from multi-angle tube tests.

Table **4-5**: Neat resin modulus and composite ply elastic properties

Material	Resin Modulus, E_m, MPa	E_2, GPa	G_{12}, GPa	ν_{12}
LF750	245	1.57	1.07	0.30
30748	510	2.28	1.45	0.31
30917	976	4.73	1.88	0.30
EPON 862	2950	8.56	6.64	0.32

4.2.4 Winding Pattern Effect on Longitudinal Compression of Composite

This section is dedicated to first determining the winding pattern of a [±21/89/±21] tube made with LF750 resin which results in the highest strength. A representative axial compressive stress-strain plot of a [±21/89/±21] LF750 tube with a pattern of two on the inside and outside helical plies is shown in Fig. **4-14**. The modulus is measured as a linear fit to the stress-strain response from 0-500 με as highlighted on the curve. 0-500 με was chosen as the strain range because it is the largest linear range in axial testing of composites with LF750 resin. The ultimate compression strength, F_x, is the largest stress realized during the test, while failure is marked with an "X." Ultimate compressive strain is the highest strain realized during the test prior to a significant drop in load.

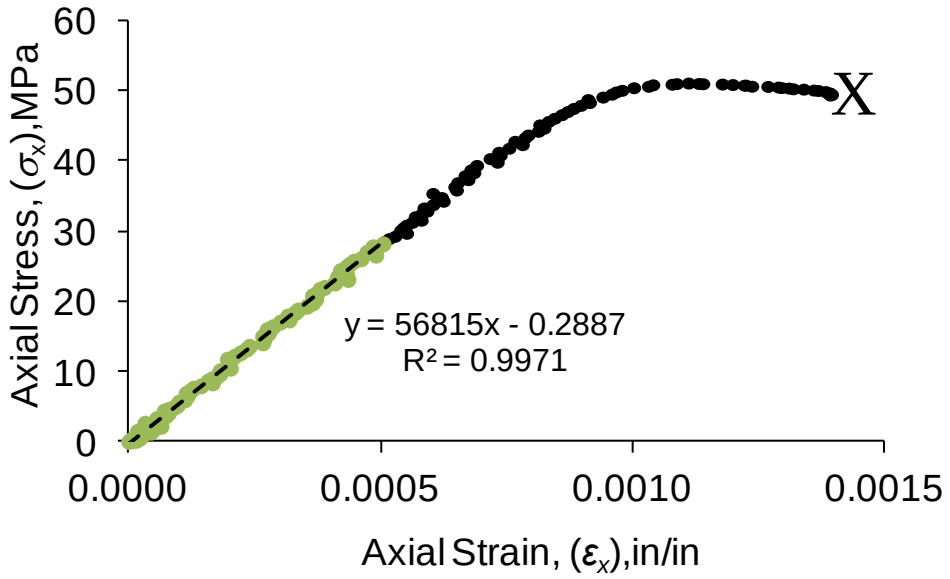

Figure **4-14**: Axial compressive stress versus axial strain curve for a [±21/89/±21] tube with [2/2] pattern.

The stress-strain response of the specimen in compression is essentially linear until 1000 με, when microbuckling of the fibers starts to occur. Microbuckling starts as a localized wrinkle on the surface of the specimen near a pattern-related fiber undulation that grows around the circumference until failure. Representative specimen failure is shown in Fig. **4-15**. The specimen in Fig. **4-15** had 10/5 patterns on the inside/outside helical layers. Failure of this type of specimen is interesting because the undulations in both helical plies do not overlay on the specimen. The undulation bands of the inner layer have approximately half the spacing as those of the outer layer. This caused the microbuckling path to sometimes jump from one circumferential undulation band to another.

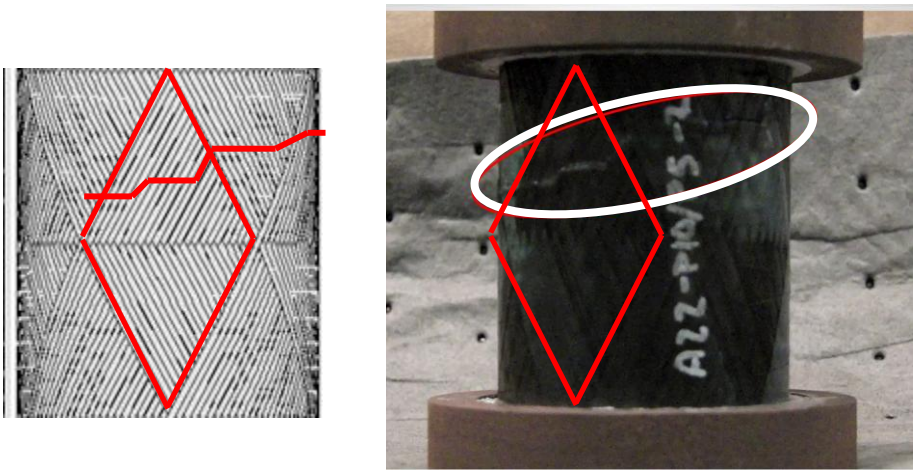

Figure **4-15**: Schematic with microbuckling path, and post-test picture with microbuckling path

The test results for the winding pattern investigation are summarized in Figure **4-16**. The winding pattern changes had little effect on modulus of the specimens because the values are approximately constant, considering the scatter in the data. However, the strength of the specimens was highly dependent on winding pattern. Increasing the pattern from [2/2] to [10/10] increased the average strength 27 %, while a mixed [10/5] pattern increased the average strength by 37 % over the 2-pattern specimen. The increase in compressive strength can be attributed to altering of the fiber microbuckling behavior. When the pattern is different in the inside and outside layers, the micro buckled fiber path has a more difficult time forming around the entire circumference of the tube. A more disorganized micro buckled pattern jumps between different pattern-related fiber undulations, resulting in a larger strength even though the axial modulus is relatively unaffected. The strength of a tube can therefore be increased by understanding the effects of winding pattern without changing the physical dimensions. It is hypothesized that varying the pattern through the thickness of a driveshaft, which will have multiple angle plies, will give you this higher strength as well. When conducting tests for evaluating F_{1C}, a pattern of [10/5] was selected.

Claus (1994) found changing the fiber pattern from through the thickness did not change the modulus of the tube. He also found that changing the pattern from [2/2] to [10/10] did not significantly change the strength but that staggering the pattern, [10/5], did increase the strength. The tubes tested by Claus were carbon/epoxy and were large enough to see that the global buckling pattern of the tubes is dominated by the size of the rhombic regions. He surmised that changing the winding pattern through the thickness caused the buckling patterns of the two plies to interfere, leading to a higher measured value of strength. A data table is available in Appendix A (Table **A-1**).

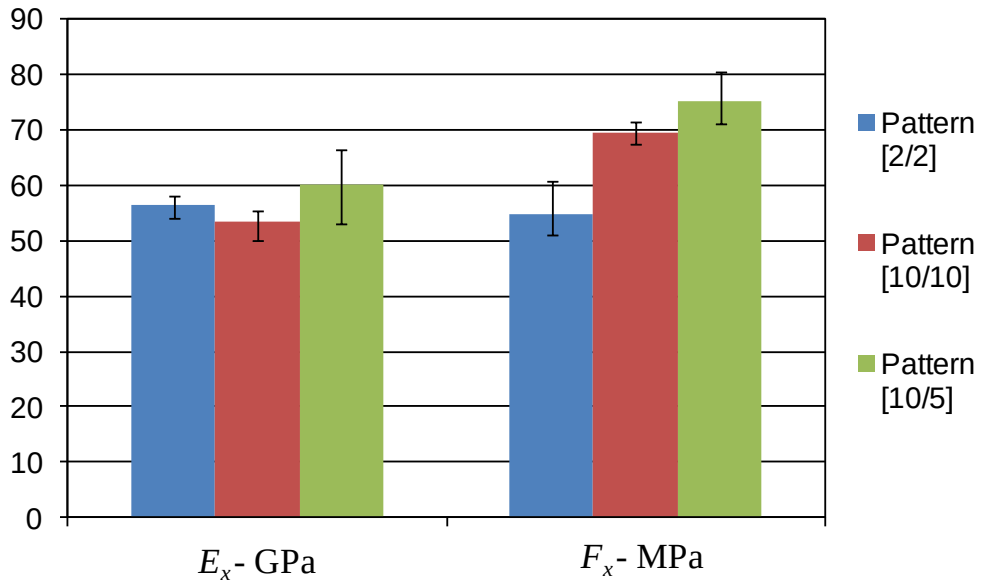

Figure **4-16**: Mean and scatter of compressive modulus, E_x, and ultimate strength, F_x, data for different winding patterns.

4.2.5 Longitudinal Compression Modulus of Composite

To determine E_1 and F_{1C}, compression tests were conducted on tubes made with LF750, 30748, 30917, and EPON 862 resins using the [10/5] winding pattern and various laminates. The

test method is described in Section 3.1.4. The compressive stress-strain results for LF750 compression tests are summarized in Table **4-6**. The stress and strain of these specimens were measured as explained in Section 3.1.4 with ultimate stress and strain defined as in Section 4.2.4. To validate the specimen design $[\pm\theta/89/\pm\theta]$ with CLPT, a value for E_1 is backed-out to match the experimentally measured axial moduli, E_x, listed in Table **4-6.** Other ply elastic properties are taken from Table **4-5**. E_x is found by fitting a line to the 0-500 με region of the stress-strain curve. A value of 101 GPa for E_1 was found by optimizing the R^2 fit, 0.9927, of CLPT to the experiment in MATLAB (Fig. **4-17**). When CLPT fit to the $[\pm\theta/89/\pm\theta]$ experiments is applied to the [±16/±60/±16] laminate, the predicted axial modulus is 55 GPa, which is 9 % lower than the experimental value. This result indicates little significance of exchanging the 89-deg. layer for the ±60-deg. layer when backing out a value of E_1 from laminate moduli with the specimen design adopted in this investigation. The backed-out value of E_1 applies equally well to a range of laminates designed with a controlled Poisson's ratio, reduced from a maximum of 4 to 0.5. For contrast, Sollenberger's (2010) fit of CLPT predictions of E_x to experimental compression data for $[\pm\theta/\pm\theta]$ laminates, for which the Poisson's ratio was uncontrolled, yields a backed out E_1 of approximately 43 GPa (Fig. **1-3**) which is far too low to be believable.

Table **4-6**: Summary of CLPT validation test results for LF750 laminates with [10/5] pattern.

Specimen Name	Specimen Layup	Compressive Modulus, E_x, GPa	Avg.	C_v, %	Compressive Strength, F_x, MPa	Avg.	C_v, %	Compressive Strain, ε_C, με	Avg.	C_v, %
A16-1	[±16/89/±16]	72	72	5.3	116	115	4.9	1620	1710	14.5
A16-2		69			120			2000		
A16-3		76			109			1500		
A31-1	[±31/89/±31]	42	38	8.0	78	75	5.9	2300	2170	14.5
A31-2		36			77			2400		
A31-3		36			70			1810		
A45-1	[±45/89/±45]	9.9	10	5.5	35	35	4.9	4700	4780	1.6
A45-2		9.5			33			4840		
A45-3		10.6			37			4810		
A16-60-1	[±16/±60/±16]	61	61	5.2	92	93	1.6	1640	1770	20.9
A16-60-2		62			91			1470		
A16-60-3		63			93			1660		
A16-60-5		56			94			2310		

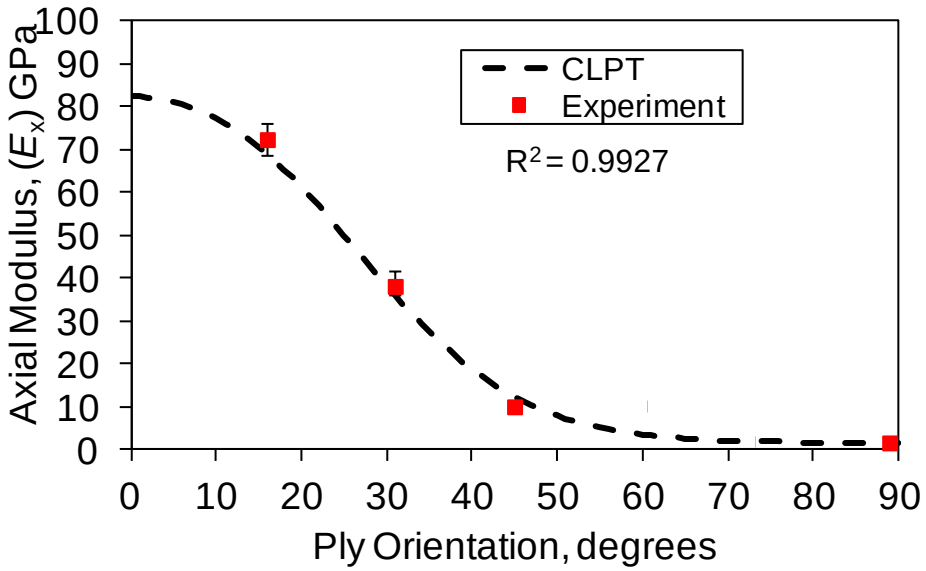

Figure **4-17**: Axial modulus versus helical ply orientation, θ, in $[\pm\theta/89/\pm\theta]$ LF750 tubes. CLPT fit is made with optimal E_1 = 101 GPa.

The process for validating this specimen design with CLPT was carried out for 30748, 30917, and EPON 862 identical to LF750. E_x is found by fitting a line to the 0-1000 με region of the stress-strain curve as a more representative strain for a helicopter driveshaft application. This can be done for stiffer resins which exhibit a linear stress-strain response to at least 1000 με. The CLPT fit to $[\pm\theta/89/\pm\theta]$ experimental data with regards to an optimized value for E_1 is presented in Table **4-7**. Compression test data for the 30748 (Table **4-8**), 30917 (Table **4-9**), and EPON 862 (Table **4-10**) fits well with CLPT, (Figs. **4-18**, **4-19**, and **4-20** respectively). When CLPT is applied to the [±16/±60/±16] laminate, with the E_1 found from $[\pm\theta/89/\pm\theta]$ testing, the predicted axial modulus is only slightly different compared to the value found experimentally, indicating that the backed-out value of E_1 applies equally well to a range of laminates for a range of different materials (Table **4-7**). It should also be considered that the RoM prediction for E_1 is significantly higher than the values measured with this specimen design. The RoM prediction

however does not take into account the fiber undulation of the interwoven helical layers. The undulated fibers have a reducing effect on modulus for softer resins.

Table **4-7** CLPT fit to $[\pm\theta/89/\pm\theta]$ laminate comparison with [±16/±60/±16] laminate

Resin Material	(a) Chosen Value of $E_{1,}$ GPa	(b) RoM, GPa ($V_{f,}$ %)	(c) CLPT Prediction of [±16/±60/±16] Laminate Modulus	(d) Experimental Modulus of [±16/±60/±16] laminate	% Difference $\frac{a-b}{b}(100)$	% Difference $\frac{d-c}{c}(100)$
30748	95	149 (59%)	51.9	55.7	-36	7.3
30917	114	157 (64%)	62.7	64.5	-28	2.9
EPON 862	134	176 (72%)	78.3	84.0	-24	7.3

Table **4-8**: Summary of CLPT validation test results for 30748 laminates with [10/5] pattern.

Specimen Name	Specimen Layup	Compressive Modulus, E_x GPa	Avg.	C_v, %	Compressive Strength, F_x MPa	Avg.	C_v, %	Compressive Strain, ε_C, με	Avg.	C_v, %
A16-1	[±16/89/±16]	62.6	64.4	2.0	139	136	5.6	2020	2050	6.3
A16-2		65.2			141			2160		
A16-3		65.4			138			2140		
A16-4		64.2			125			1880		
A31-1	[±31/89/±31]	36.5	36.9	5.0	110	110	2.5	4610	3902	13.0
A31-2		36.4			110			3640		
A31-3		34.9			107			4080		
A31-4		39.9			108			3930		
A31-5		37.0			114			3250		
A45-1	[±45/89/±45]	10.5	10.3	4.5	88.9	84.6	4.3	10500	9560	6.98
A45-2		10.4			84.4			9510		
A45-3		9.7			81.5			9460		
A45-4		10.0			80.7			8630		
A45-5		10.9			87.7			9700		
A16-60-1	[±16/±60/±16]	52.0	55.7	5.1	110	117	5.5	1800	2120	22.5
A16-60-2		57.6			119			2090		
A16-60-3		53.7			112			1860		
A16-60-4		56.1			126			2950		
A16-60-5		59.0			117			1900		

Table **4-9**: Summary of CLPT validation test results for 30917 laminates with [10/5] pattern.

Specimen Name	Specimen Layup	Compressive Modulus, E_x GPa	Avg.	C_v, %	Compressive Strength, F_x MPa	Avg.	C_v, %	Compressive Strain, ε_C, με	Avg.	C_v, %
A16-1	[±16/89/±16]	73.3	79.0	6.3	229	229	5.7	2750	2792	7.7
A16-2		78.1			232			2810		
A16-3		78.8			244			3120		
A16-4		86.9			232			2760		
A16-5		77.7			208			2520		
A31-1	[±31/89/±31]	42.6	46.1	5.2	207	205	3.2	4830	4606	3.3
A31-2		46.1			208			4590		
A31-3		45.8			206			4510		
A31-4		49.3			212			4670		
A31-5		46.6			194			4430		
A45-1	[±45/89/±45]	16.0	16.0	4.3	112	117	4.8	8320	8598	5.6
A45-2		16.4			110			7960		
A45-3		16.2			122			8970		
A45-4		14.8			117			8590		
A45-5		16.5			122			9150		
A16-60-1	[±16/±60/±16]	57.3	64.5	6.9	176	197	7.3	3860	3438	8.1
A16-60-2		63.6			207			3560		
A16-60-3		68.9			212			3360		
A16-60-4		67.0			189			3190		
A16-60-5		65.5			200			3220		

Table **4-10**: Summary of CLPT validation test results for EPON 862 laminates with [10/5] pattern.

Specimen Name	Specimen Layup	Compressive Modulus, E_x GPa	Avg.	C_v, %	Compressive Strength, F_x MPa	Avg.	C_v, %	Compressive Strain, ε_C, με	Avg.	C_v, %
A16-2	[±16/89/±16]	102	102	2.3	419	441	6.8	4380	4580	5.3
A16-3		105			429			4510		
A16-4		100			475			4850		
A31-2	[±31/89/±31]	54	53	5.5	361	368	6.1	7010	6957	9.2
A31-3		50			393			7570		
A31-5		56			350			6290		
A45-1	[±45/89/±45]	24	22	4.9	306	291	4.5	15800	14700	10.2
A45-2		23			295			15300		
A45-3		21			271			13000		
A45-4		23			288			16000		
A45-5		22			295			15700		
A16-60-1	[±16/±60/±16]	92	84	8.8	411	413	6.1	4950	5018	16.8
A16-60-2		88			387			4300		
A16-60-4		80			407			4600		
A16-60-5		76			447			6220		

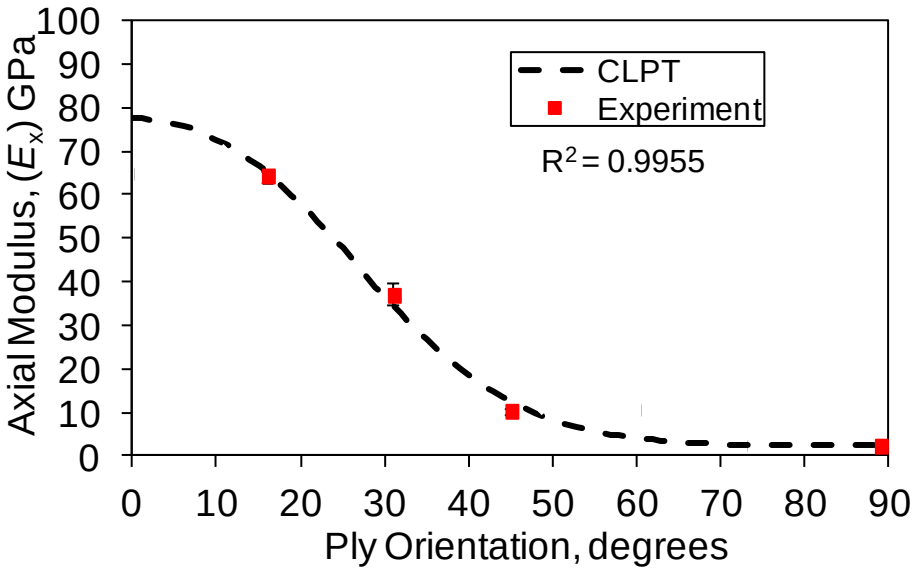

Figure **4-18**: Axial modulus versus helical ply orientation, θ, in $[\pm\theta/89/\pm\theta]$ 30748 tubes. CLPT fit is made with optimal E_1 = 95 GPa.

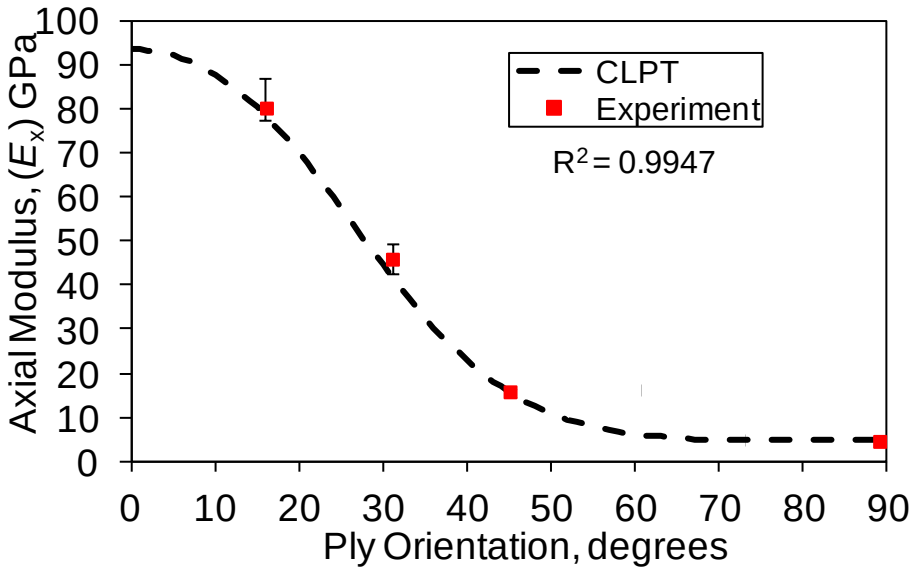

Figure **4-19**: Axial modulus versus helical ply orientation, θ, in $[\pm\theta/89/\pm\theta]$ 30917 tubes. CLPT fit is made with optimal E_1 = 114 GPa.

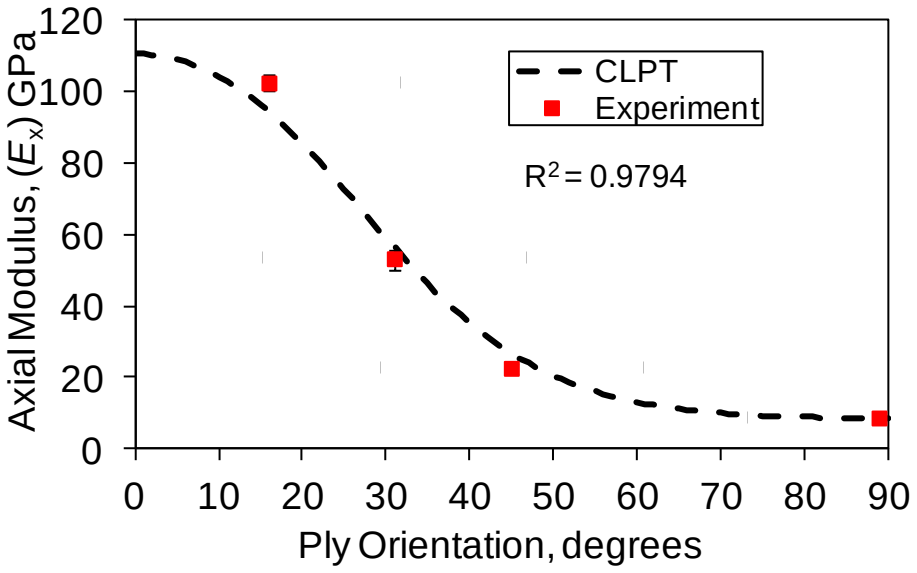

Figure **4-20**: Axial modulus versus helical ply orientation, θ, in $[\pm\theta/89/\pm\theta]$ EPON 862 tubes. CLPT fit is made with optimal E_1 = 134 GPa.

4.2.6 Longitudinal Compression Strength of Composite

The objective of this section is to find the fiber direction compression strength, F_{1C}, of the composite tubes in Section 4.3.5. A value for the fiber direction compressive strength, F_{1c}, for the tubes is found by calculating the ply-level stresses $\sigma_1, \sigma_2,$ and τ_{12} at failure for the strength-governing helical plies of the $[\pm\theta/89/\pm\theta]$ laminates. This is done using CLPT with the material parameters in Table **4-5** and Table **4-7,** the tube geometric parameters in Table **2-7**, and the tube compressive strengths in Tables **4-6, 4-8, 4-9,** and **4-10**. A bi-quadratic function in the form of equation (28) is proposed for fitting to the calculated longitudinal and shear stresses at compressive failure of the laminates.

$$\left(\frac{\sigma_1}{F_{1c}}\right)^2 + \left(\frac{\tau_{12}}{F_6}\right)^2 = 1 \tag{28}$$

Once three different (σ_1, τ_{12}) failure points are plotted as in Fig. **4-21** for the three different laminates designed to fail at the onset of fiber microbuckling in the helical plies, equation (28) is fitted to the points using the Solver optimization function in Microsoft Excel. Then, F_{1c} can be determined from the intersection of the ellipse with the σ_1 axis, which is presumably where the strength of a $[0/89/0]$ laminate would be plotted if such a laminate could be manufactured by filament winding. The intersection of the function with the τ_{12} axis is of no practical significance, since no laminates of the $[\pm\theta/89/\pm\theta]$ family have only shear stress without longitudinal stress at the ply level.

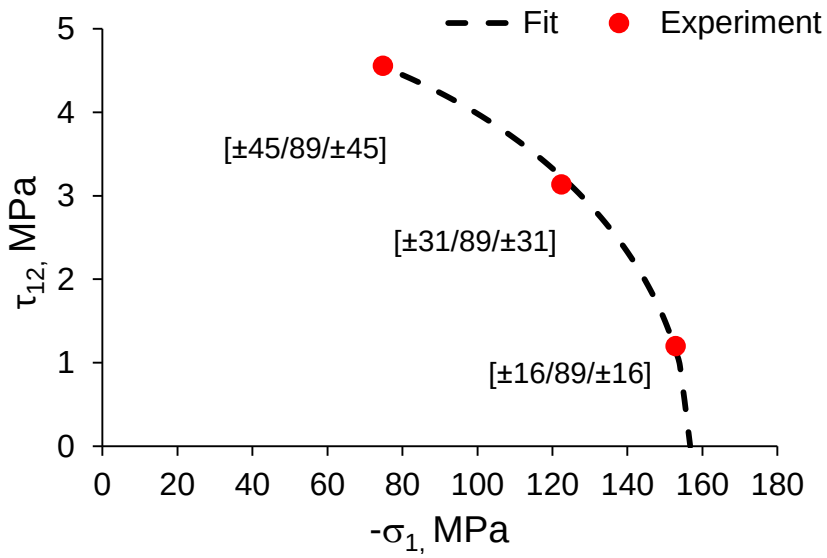

Figure **4-21**: Ply stresses τ_{12} and σ_1 at compressive failure of LF750 $[\pm\theta/89/\pm\theta]$ laminates

Based on Fig. **4-21**, F_{1c} is 157 MPa for LF750. When ply-level stresses are calculated in the [±16/±60/±16] tube at failure, the predicted stress, σ_1 , is -151 MPa in the ±16-deg. plies, which is 1.2 % lower than its $[\pm\theta/89/\pm\theta]$ counterparts. This close correspondence in F_{1C} indicates satisfactory generality of the extracted F_{1C} value for practical laminates used for shafts. The values found during optimization are summarized in Table **4-11**.

Table **4-11** Back-calculated F_{1C} and F_6 fit values

Resin Material	F_{1C}, MPa	F_6, MPa
LF750	157	5.2
30748	178	32
30917	326	30
EPON 862	556	155

The failure space for the 30748, 30917, and EPON 862 are plotted together with LF750 in Fig. **4-22**. When the critical fiber direction stresses, σ_1, are calculated in the [±16/±60/±16] tubes at failure, the stress is, within 13 % of the value extracted optimally from all the $[\pm\theta/89/\pm\theta]$ laminates (Table **4-12**). This is a reasonably small difference, considering the slight variability in strength and the small number of tested tubes. However, the conclusion that lamination arrangement does not significantly affect the back calculated F_{1c} applies equally well to all materials tested with the evaluated family of laminates.

Table **4-12** Back-calculated σ_1 values for different laminates

Resin Material	F_{1C}, MPa	(a) Stress σ_1 in ±16 plies of [±16/89/±16] Laminate at failure	(b) Stress σ_1 in ±16 plies of [±16/±60/±16] Laminate at Failure	% Difference, $\frac{b-a}{a}(100)$
30748	178	-178	-189	6.2
30917	326	-296	-317	7.1
EPON 862	556	-556	-630	13.3

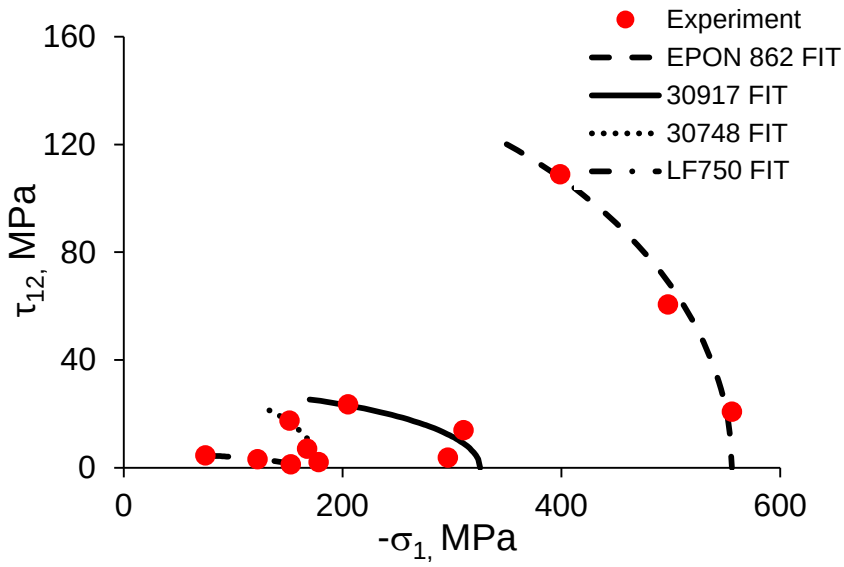

Figure **4-22**: Ply stresses τ_{12} and σ_1 at compressive failure for all resins

4.3 Estimating Ply Failure Criteria and Elastic Properties with Matrix Modulus

Evaluating a potential resin for use in a helicopter driveshaft involves a large amount of testing. Traditional micromechanical models such as the RoM and semi-empirical models do not work well for predicting the ply strength and elastic properties in filament wound composites or FMCs (Crane and Ratcliffe, 1993; Shan and Bakis, 2002; Sollenberger 2010), which leaves experimentation as the only viable alternative. In order to circumvent the need for extensive fabrication and testing of composites with new prospective resin systems, an effort was made to find a simple power law relationship between the neat resin modulus, E_m, and ply elastic properties and strengths of the form of equation (29),

$$X = C_1 E_m^{C_2} \tag{29}$$

where X is the ply elastic property that is being fit to E_m and C_1 and C_2 are constants to be found by using Solver optimization function in Microsoft Excel . Equation (29) was applied to

experimental data from LF750, 30748, 30917, and EPON 862 composites. LF750 data other than F_{1C} and E_1 were taken from Sollenberger (2010). Equation (29) is shown to have good agreement with experimental F_{2T} results reported in Section 4.2.1, with an R^2 of 0.9969 (Fig. **4-23**). Suprisingly, as the resin modulus increases so does the strength of the composite in the transverse direction.

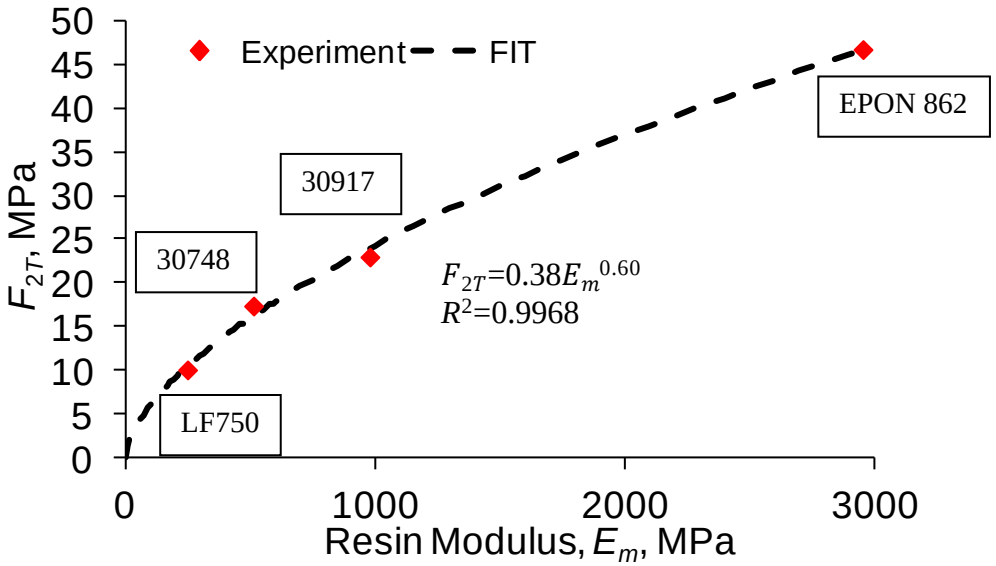

Figure **4-23**: Ply transverse tensile strength, F_{2T}, vs. resin modulus, E_m

The power law relationship also fits equally well for F_6 vs. E_m (Fig. **4-24**) and G_{12} vs. E_m (Fig. **4-25**), F_{2C} vs. E_m (Fig. **4-26**) and E_2 vs. E_m (Fig. **4-27**), and F_{1C} vs. E_m (Fig. **4-28**) and E_1 vs. E_m (Fig. **4-29**). The strength and modulus data were taken from Sections 4.2.2, 4.2.3, and 4.2.4. It should be noted that by including EPON 862 with an E_m of 2954 MPa, the fitted power laws span over a wide range of material stiffnesses and chemical makeups, including polyurethanes and epoxies. The power law fits least well for experimental values of E_1. This is likely due to E_1 being a fiber dominated property as well as effect of fiber undulations which are still under investigation and variations in fiber volume fraction. With these useful relationships between ply elastic properties and strengths with resin modulus, only a neat resin dogbone test needs to be

completed to get a rough idea of the properties of the composite. As the resin modulus increases the other properties do as well.

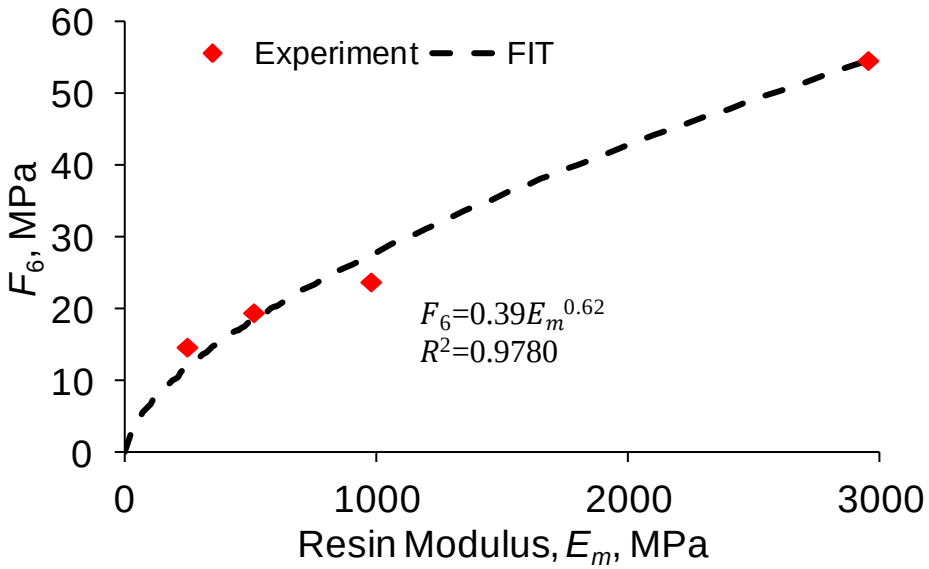

Figure **4-24**: Ply shear strength, F_6, vs. resin modulus, E_m

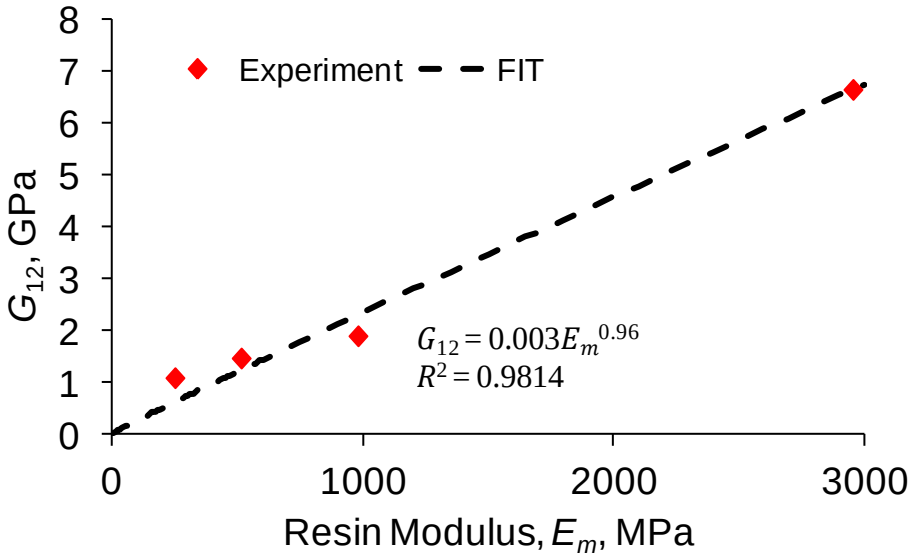

Figure **4-25**: Ply shear modulus, $G_{12,}$ vs. resin modulus, E_m

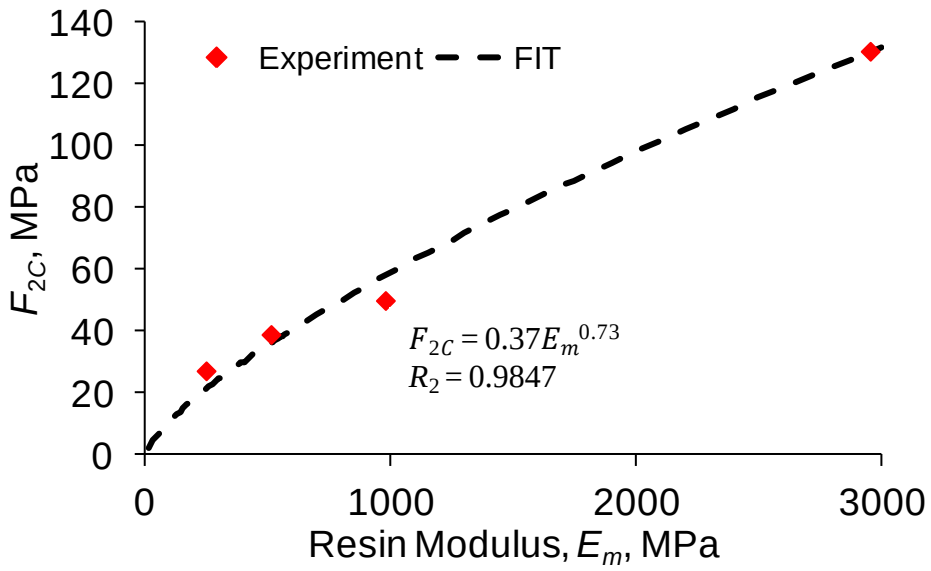

Figure **4-26**: Ply transverse compression strength, F_{2C}, *vs*. resin modulus, E_m

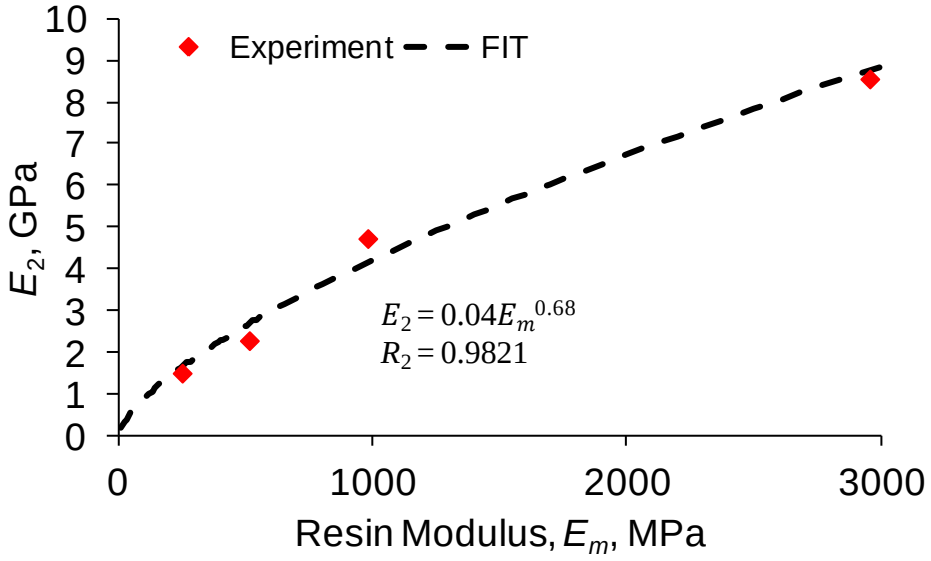

Figure **4-27**: Ply transverse modulus, E_2, vs. resin modulus, E_m

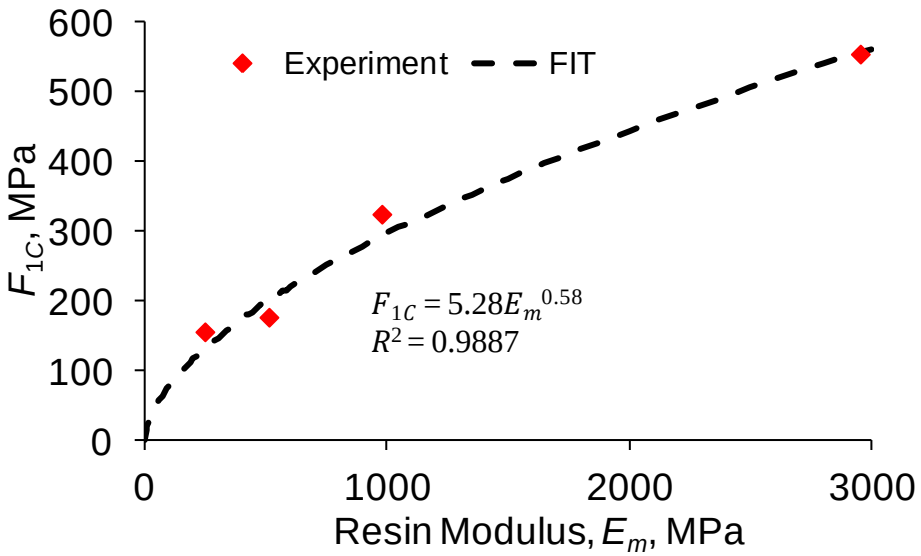

Figure **4-28**: Ply longitudinal compressive strength, F_{1C}, *vs.* resin modulus, E_m

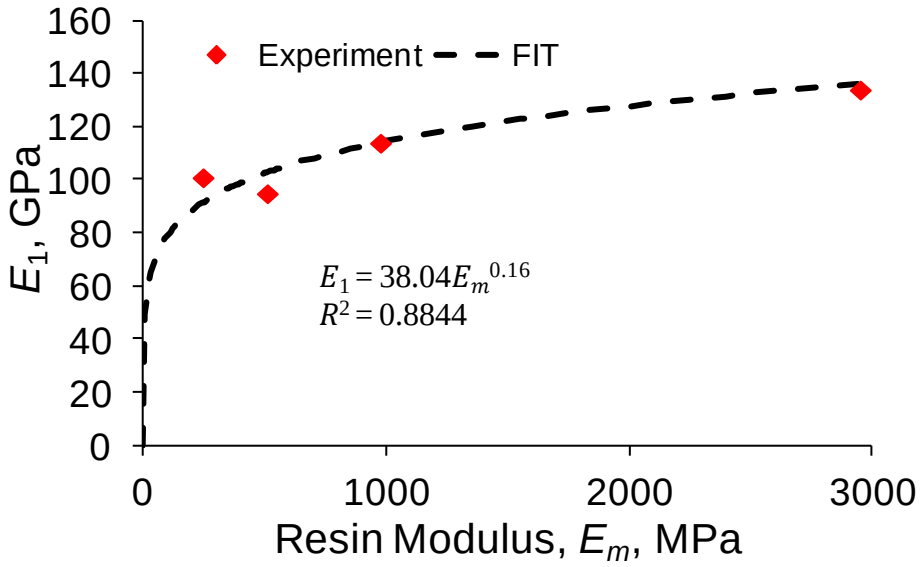

Figure **4-29**: Ply longitudinal modulus, $E_{1,}$ vs. resin modulus, E_m

Chapter 5

Dynamic Test Results

5.1 Dynamic Transverse Flexure of Composite

The composite material properties under investigation are sensitive to temperature as well as loading frequency. Test results presented in this section were conducted using the process outlined in Section 3.2.1. Curve fitting and the creation of a master curve was done according to Section 1.2 in a manner identical to that of Shan and Bakis (2009). The materials under investigation are also sensitive to strain amplitude as demonstrated in Section 4.1 by there being a change in modulus depending on the strain range used. The strain transverse to the fibers in a typical helicopter driveshaft could be anywhere from 1500 – 1800 με (Mayrides, 2005; Roos and Bakis, 2011). This value is found by using the optimization code developed by Roos and Bakis (2011) and finding the maximum ε_2 in the optimized shaft. Considering applicability to a real design case, and physical constraints of the bending DMA, 1700 με was chosen as the strain amplitude for the dual cantilever DMA test. In order to gain a broader understanding of the dynamic response of the composite, bending DMA tests were also conducted at a strain amplitude of 200 με as in a previous investigation of AS4D/LF750 (Sollenberger, 2010).

5.1.1 Unshifted Data

Storage modulus and loss factor results from the bending DMA run at 1700 με for the LF750 composite are shown in Figs. **5-1** and **5-2**, respectively. The effect of temperature is evident by the decreasing storage modulus and increasing loss factor as temperature increases—

i.e., as the material heats up it becomes softer and more damped. Increasing the frequency has the opposite effect—i.e., increasing storage modulus and decreasing loss factor. For the testing conditions evaluated the loss factor varies between 0.10 and 0.45.

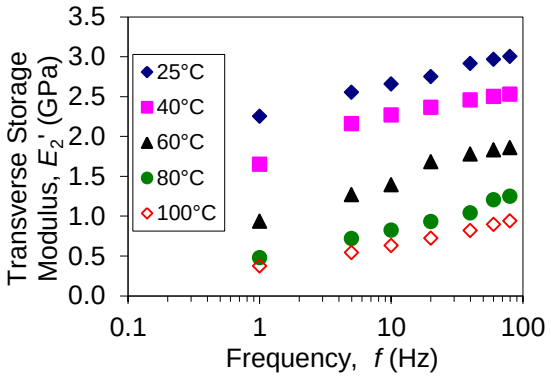

Figure **5-1**: Transverse storage modulus vs. frequency — LF750, 1700 με

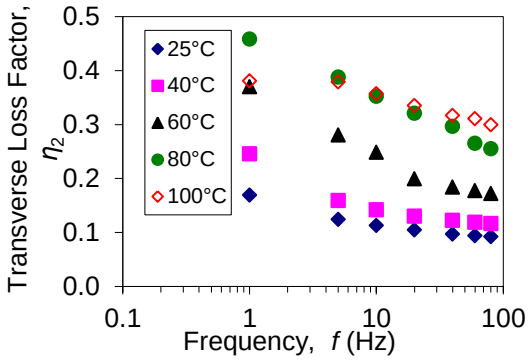

Figure **5-2**: Transverse loss factor vs. frequency — LF750, 1700 με

Bending DMA transverse storage and loss factor data were also collected for 30748 (Figs. **5-3, 5-4**), 30757 (Figs. **5-5, 5-6**), 30917 (Figs. **5-7, 5-8**), and EPON 862 (Figs. **5-9, 5-10**) composites.

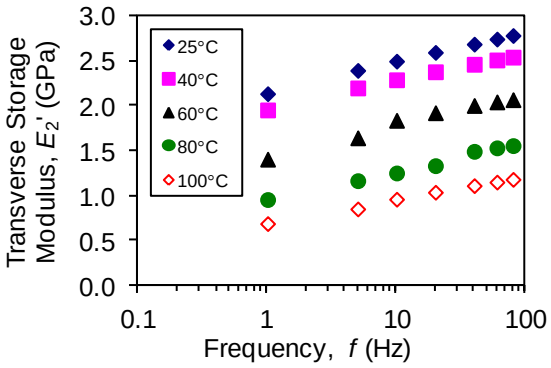

Figure **5-3**: Transverse storage modulus vs. frequency — 30748, 1700 με

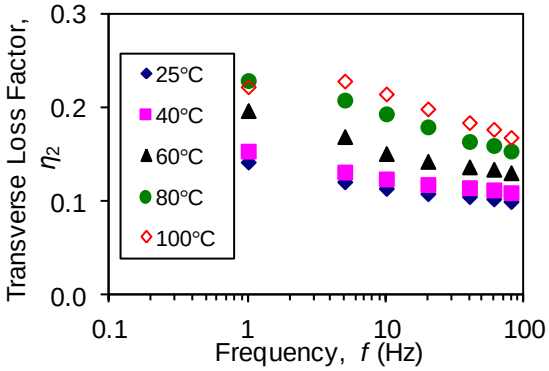

Figure **5-4**: Transverse loss factor vs. frequency — 30748, 1700 με

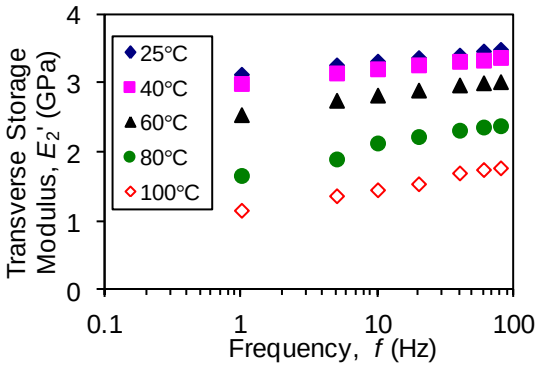

Figure **5-5**: Transverse storage modulus vs. frequency — 30757, 1700 με

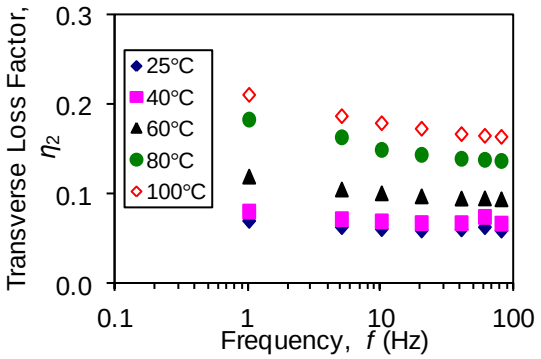

Figure **5-6**: Transverse loss factor vs. frequency — 30757, 1700 με

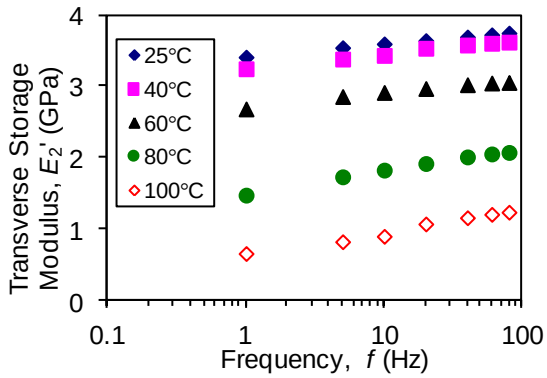

Figure **5-7**: Transverse storage modulus vs. frequency — 30917, 1700 με

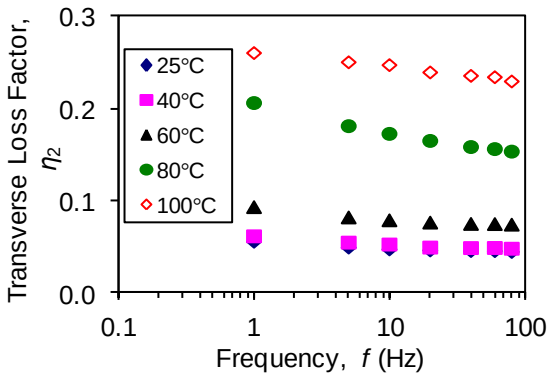

Figure **5-8**: Transverse loss factor vs. frequency — 30917, 1700 με

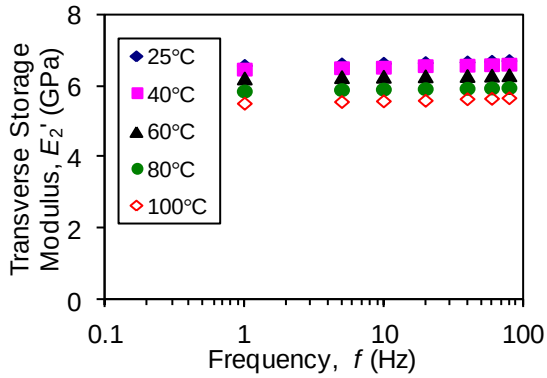

Figure **5-9**: Transverse storage modulus vs. frequency — EPON 862, 1700 με

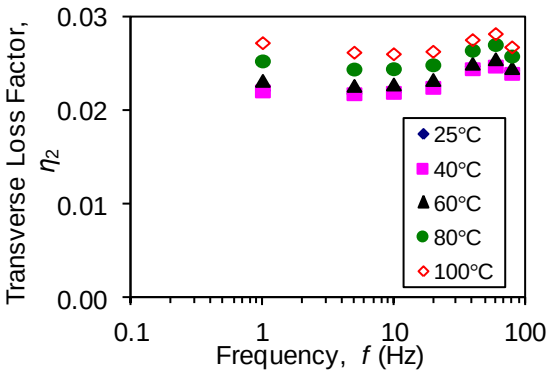

Figure **5-10**: Transverse loss factor vs. frequency — EPON 862, 1700 με

The Conathane series polyurethanes, 30748, 30757, and 30917 have identical dependencies on temperature and frequency as LF750. The transverse loss factor of these resins is, however, lower in the range of 0.05-0.25. This trend is favorable because the transverse storage moduli of the four polyurethane resins are similar to each other meaning that the loss moduli and potentially self-heating will be lower as well. The resin which is best suited to a helicopter driveshaft design case will have the smallest loss modulus (Fig. **5-11**). The material best suited based on this criterion is EPON 862. The best polyurethane would be 30917 for temperatures up to 70 °C. It should be noted that because 30748 has a decreasing loss modulus with increasing temperature, the self-heating behavior of 30748 should be self-stabilizing in that as the FMC gets hotter it generates less heat.

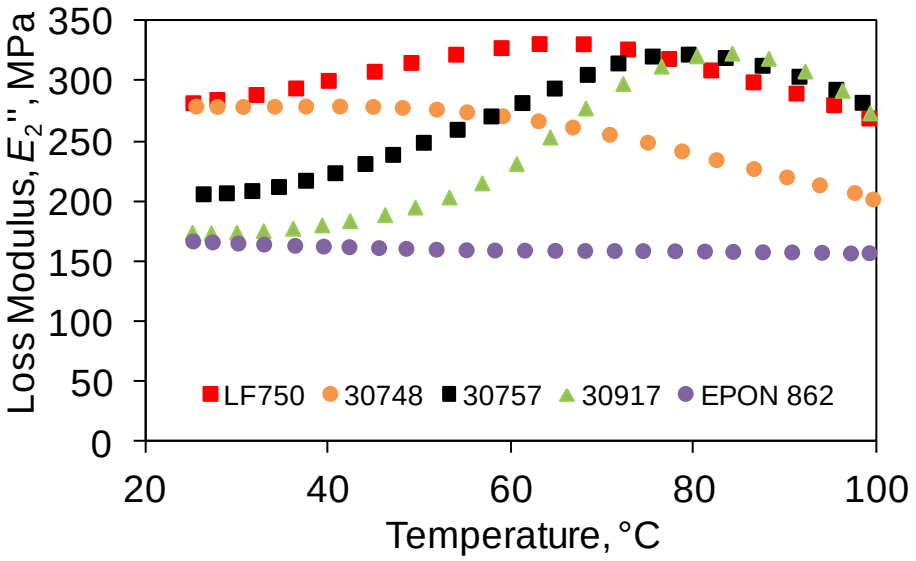

Figure **5-11**: Transverse loss modulus vs. temperature for five composites at 40 Hz

5.1.2 Curve Fitting and Creating a Master Curve

The dynamic data collected in Section 5.1.1 were adjusted along the horizontal axis using temperature-based shifting factors with a reference temperature of 60 °C. A shifting factor is unique to each temperature and is determined by eye for each temperature investigated (Fig. **5-12** and **5-13**). Each shifting factor is used for both the storage modulus and loss factor, with a unique set of shifting factors for each of the materials. A WLF function (described in detail in Section 1.2) was used to fit a curve to the shifting factors for a given material. This allows for finding the shifting factor based on any temperature, not just those tested. The Solver add-on in Excel was used to optimize the R^2 fit of the WLF function to the data by manipulating the constants C_1 and C_2 (Fig. **5-14**).

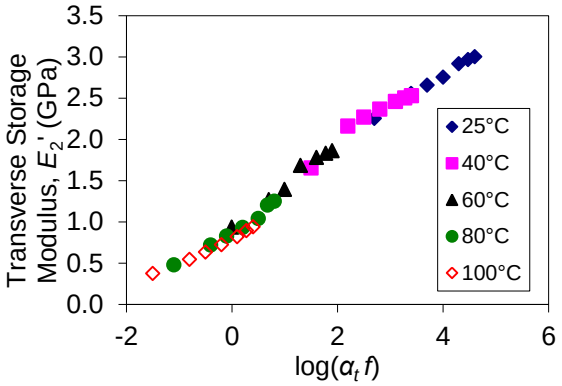

Figure **5-12**: Transverse storage modulus vs. log reduced frequency — LF750

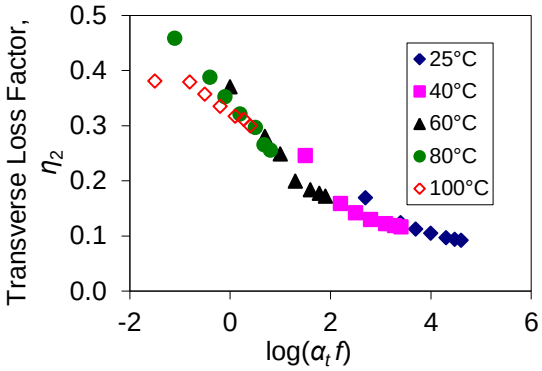

Figure **5-13**: Transverse loss factor vs. log reduced frequency — LF750

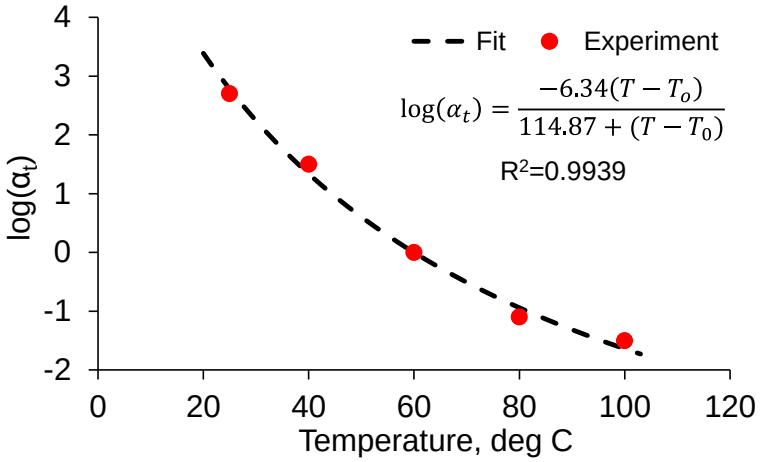

Figure **5-14**: Log temperature shift factor vs. temperature — E_2'' and η_2, LF750

The Solver add-on in Excel is also used to optimize the R^2 fit of the fractional derivative model (Shan and Bakis, 2009), equations (6) and (8), to the shifted storage modulus and loss factor data by manipulating constants E, b_1, β_1, b_2, β_2, a_1, and a_2 (Fig. **5-15** and Fig. **5-16**).

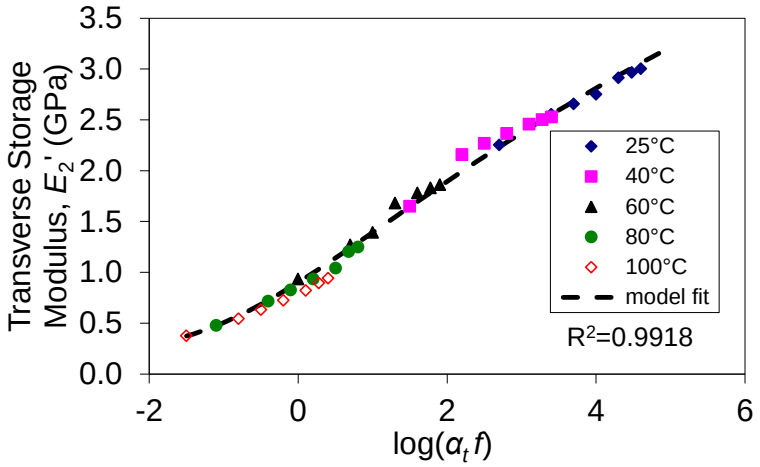

Figure **5-15**: Experimental and modeled transverse storage modulus vs. log reduced frequency — LF750

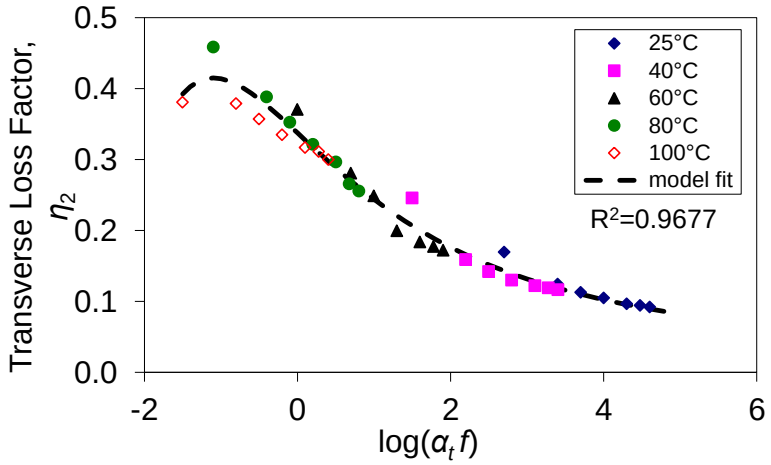

Figure **5-16**: Experimental and modeled transverse loss factor vs. log reduced frequency — LF750

The temperature shifting and master curve creation technique was carried out on 30748 (Fig. **5-17**, Fig. **5-18**, and Fig. **5-19**), 30757 (Fig. **5-20**, Fig. **5-21**, and Fig. **5-22**), 30917 (Fig. **5-23**, Fig. **5-24**, and Fig. **5-25**), and EPON 862 (Fig. **5-26**, Fig. **5-27**, and Fig. **5-28**) in the same manner as for LF750.

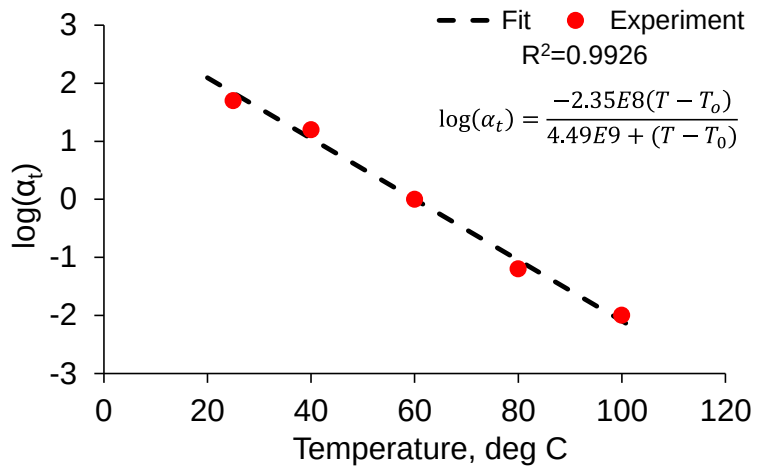

Figure **5-17**: Log temperature shift factor vs. temperature for E_2'' and η_2 — 30748

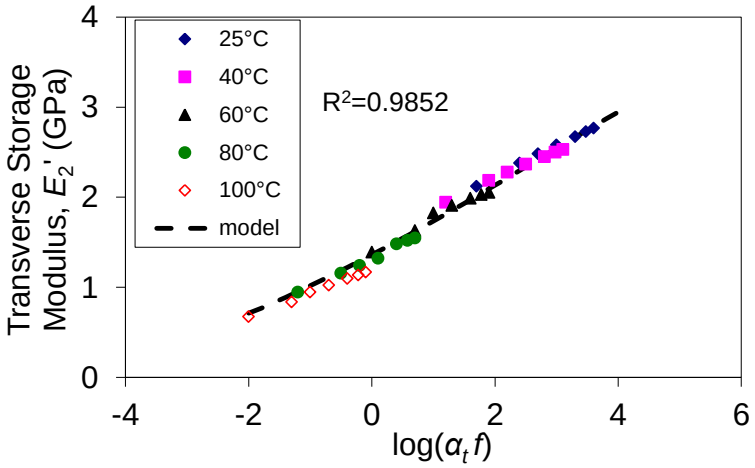

Figure **5-18**: Experimental and modeled transverse storage modulus vs. log reduced frequency — 30748

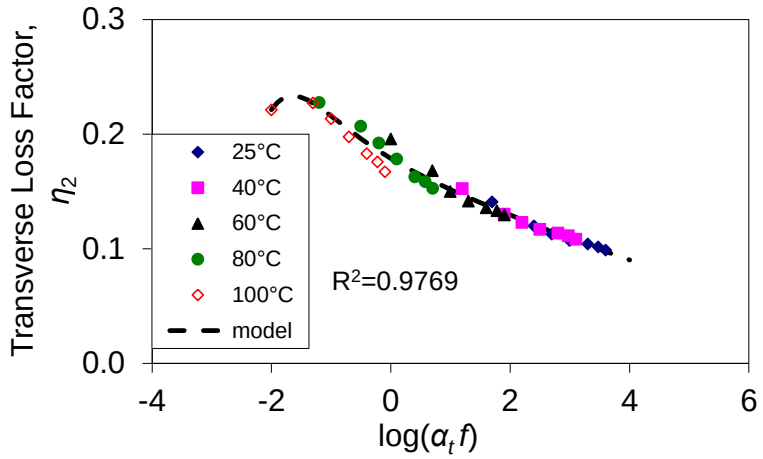

Figure **5-19**: Experimental and modeled transverse loss factor vs. log reduced frequency — 30748

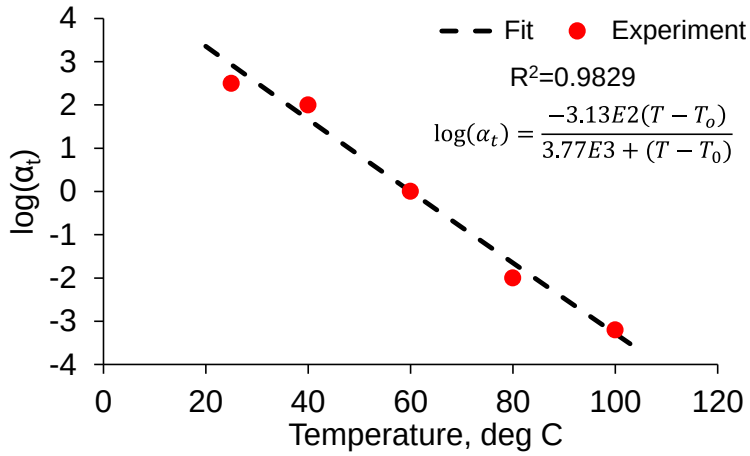

Figure **5-20**: Log temperature shift factor vs. temperature for E_2'' and η_2 — 30757

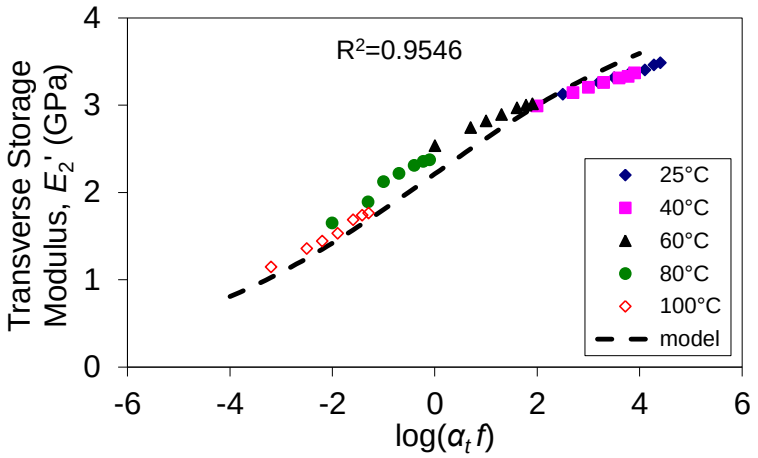

Figure **5-21**: Experimental and modeled transverse storage modulus vs. log reduced frequency — 30757

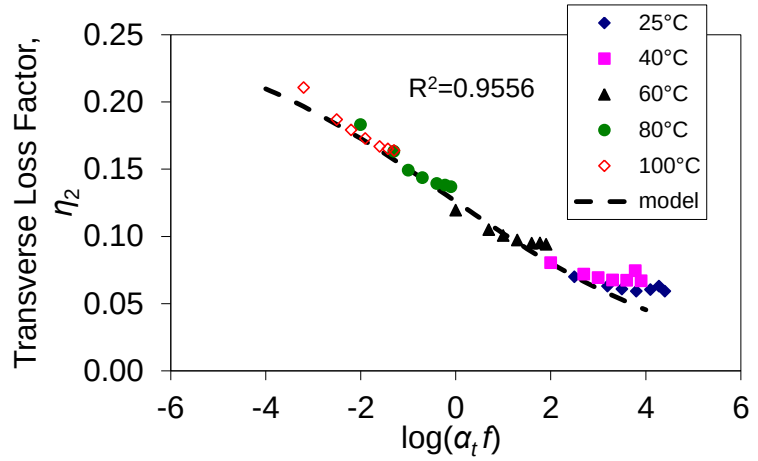

Figure **5-22**: Experimental and modeled transverse loss factor vs. log reduced frequency — 30757

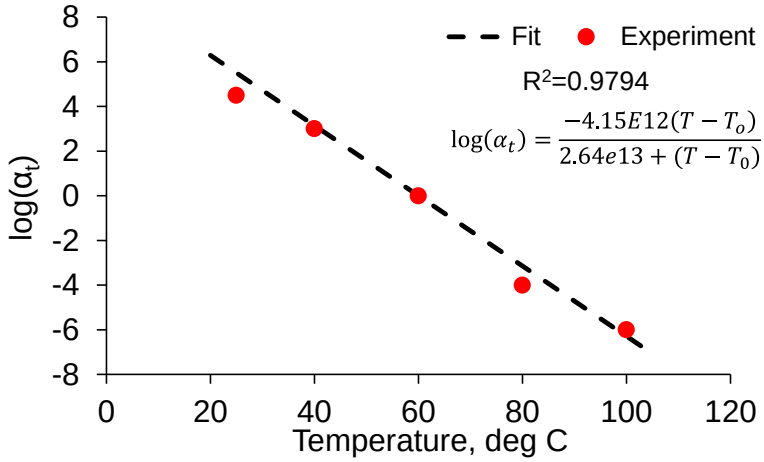

Figure **5-23**: Log temperature shift factor vs. temperature for $E_2^{''}$ and η_2 — 30917

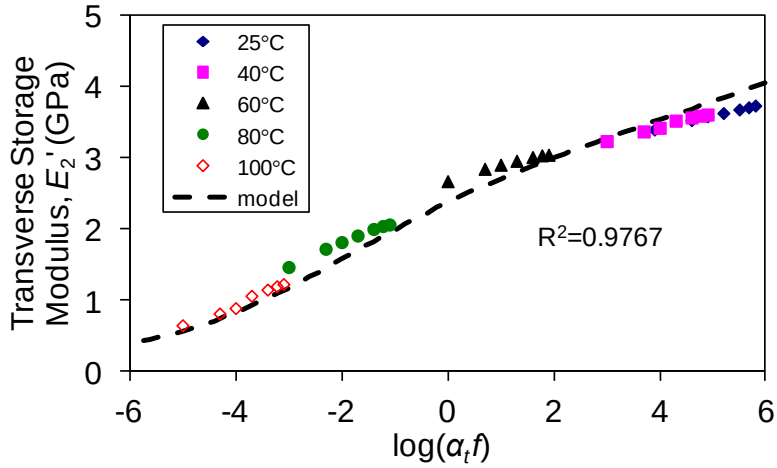

Figure **5-24**: Experimental and modeled transverse storage modulus vs. log reduced frequency — 30917

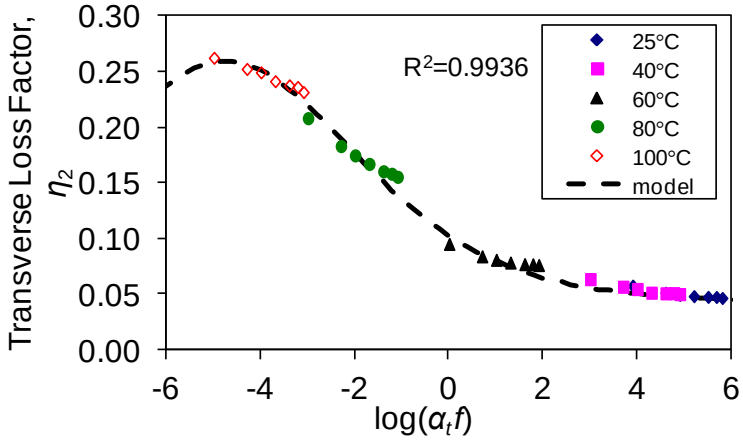

Figure **5-25**: Experimental and modeled transverse loss factor vs. log reduced frequency — 30917

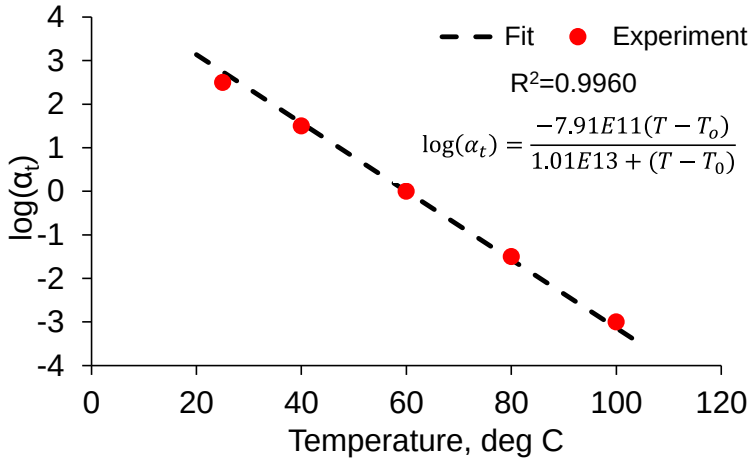

Figure **5-26**: Log temperature shift factor vs. temperature for $E_2^{''}$ and η_2 — EPON 862

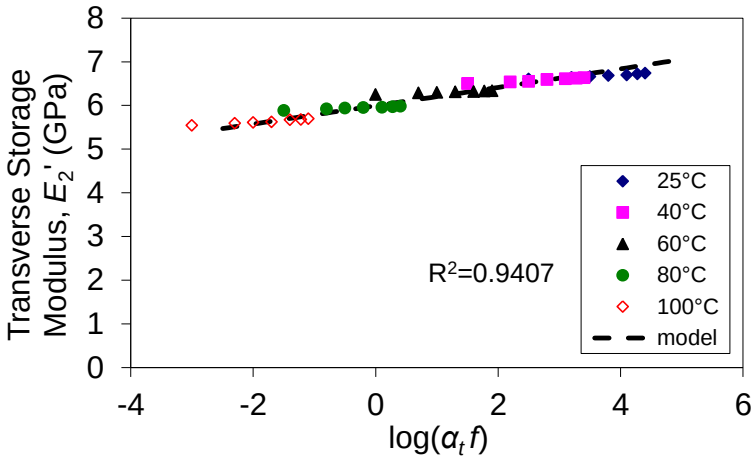

Figure **5-27**: Experimental and modeled transverse storage modulus vs. log reduced frequency — EPON 862

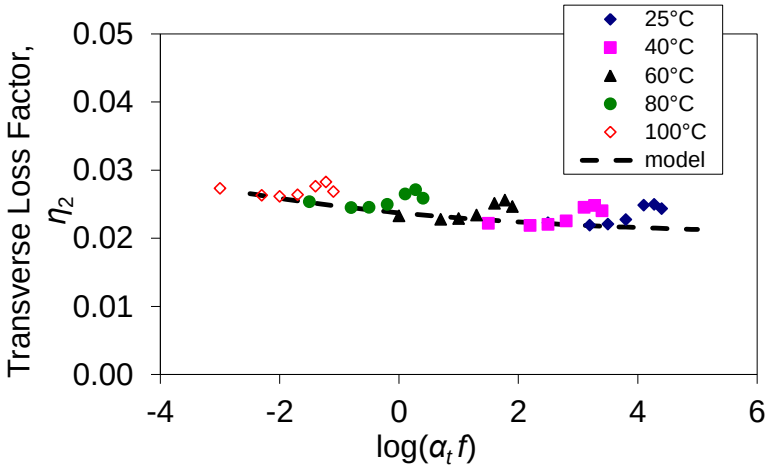

Figure **5-28**: Experimental and modeled transverse loss factor vs. log reduced frequency — EPON 862

The WLF equation and the fractional derivative model (Shan and Bakis, 2009) fit fairly well to the experimental data. The R^2 value fit to the WLF equation are above 0.98 and for most cases the fractional derivative model R^2 is above 0.97. All of the curve-fit constants for the WLF function and the fractional derivative model are listed in Table **5-1**.

Table **5-1** Fractional derivative model and WLF equation constants for bending DMA—1700 με

Parameter \ Resin	LF750	30748	30757	30917	EPON 862
E_2	5.58E-01	6.52E-01	7.29E-02	1.60E-01	1.44E+00
a_1	7.35E-01	3.81E+01	1.31E+03	4.85E+00	3.71E+01
b_1	-2.51E+01	-1.08E+01	-6.96E-03	1.58E-07	6.11E-03
β_1	2.81E-01	6.25E-01	-1.14E-01	2.45E-01	1.14E-01
a_2	2.18E+00	1.66E+01	1.34E+03	2.95E-12	2.02E-05
b_2	3.05E+01	1.27E+02	8.05E+04	8.54E+01	1.58E+02
β_2	3.24E-01	7.61E-01	4.83E-02	2.72E-01	1.27E-01
C_1	-6.34E+00	-2.35E+08	-3.13E+02	-4.15E+12	-7.91E+11
C_2	1.15E+02	4.49E+09	3.77E+03	2.64E+13	1.01E+13

Bending DMA tests were also conducted for the five materials at 200 με for comparison. For reasons of brevity, WLF and fractional derivative model curve fits are given in the Appendix A. The dynamic response of the material varies when different strain amplitudes are considered (Fig. **5-29**, **5-30**). In quasi-static testing on FMCs discussed earlier, increasing the strain when fitting modulus resulted in a lower value of modulus. In Figure **5-29** the opposite trend is observed in the dynamic storage modulus data. However, it should be kept in mind that determining the effect of strain amplitude on dynamic response using an apparatus like a bending DMA or torsional rheometer is not straight forward. Both of these machines measure displacement responses that include the deformation of the actuator and specimen support points. These unwanted machine displacements are normally calibrated out of the results for a specimen

of a certain known dynamic stiffness. However, when the dynamic stiffness of the specimen varies significantly due to strain amplitude, frequency, and temperature, as we have seen with FMC composites, it is practically impossible to calibrate out machine deformation effects for the full range of testing conditions. This fact complicates the comparison of DMA results for different strain amplitudes.

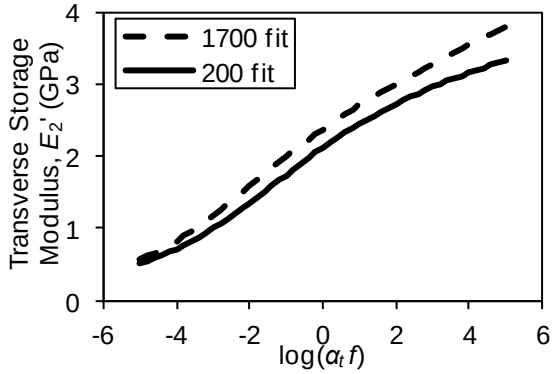

Figure **5-29**: Fractional derivative model comparison of transverse storage modulus at 200 and 1700 με

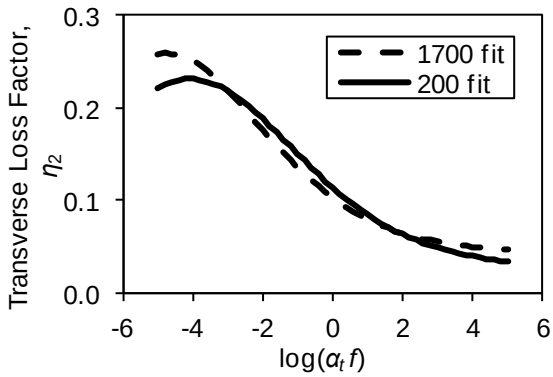

Figure **5-30**: Fractional derivative model comparison of transverse loss factor at 200 and 1700 με

5.2 Dynamic Shear of Composite

Test results presented in this section were conducted using the procedure outlined in Section 3.2.2. Shear storage modulus and shear loss factor data were collected versus frequency at various temperatures and shifted (5000 με). The fractional derivative model and WLF equation were fit to the experimental data in a manner identical to Section 5.1 for LF750 (Fig. **5-31**, Fig. **5-32**), 30748 (Fig. **5-33**, Fig. **5-34**), 30757 (Fig. **5-35**, Fig. **5-36**), 30918 (Fig. **5-37**, Fig. **5-38**), 30917 (Fig. **5-39**, Fig. **5-40**), and EPON 862 (Fig. **5-41**, Fig. **5-42**). WLF equation curve fits are omitted for brevity (Appendix A), although the constants C_1 and C_2 are listed along with the fractional derivative model parameters in Table **5.2**.

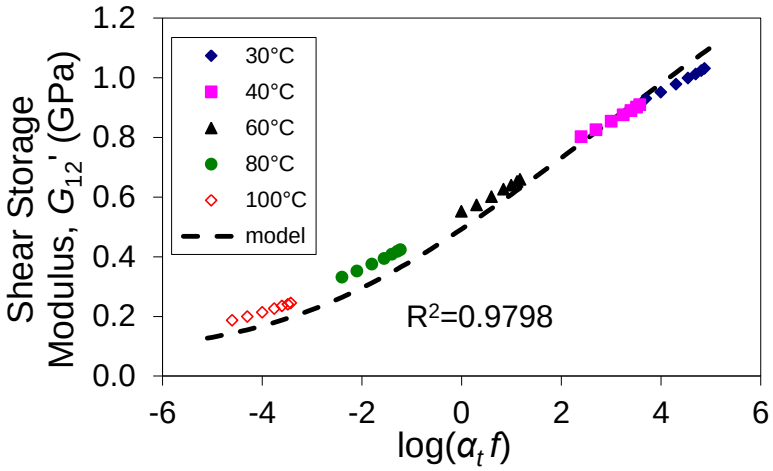

Figure **5-31**: Experimental and modeled shear storage modulus vs. log reduced frequency — LF750

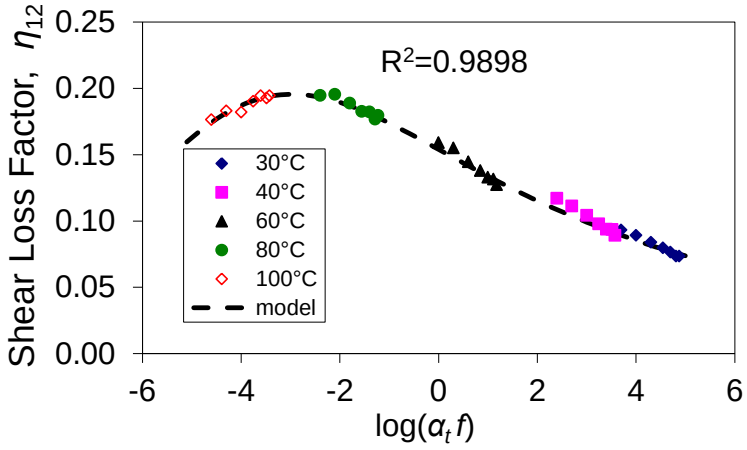

Figure **5-32**: Experimental and modeled shear loss factor vs. log reduced frequency — LF750

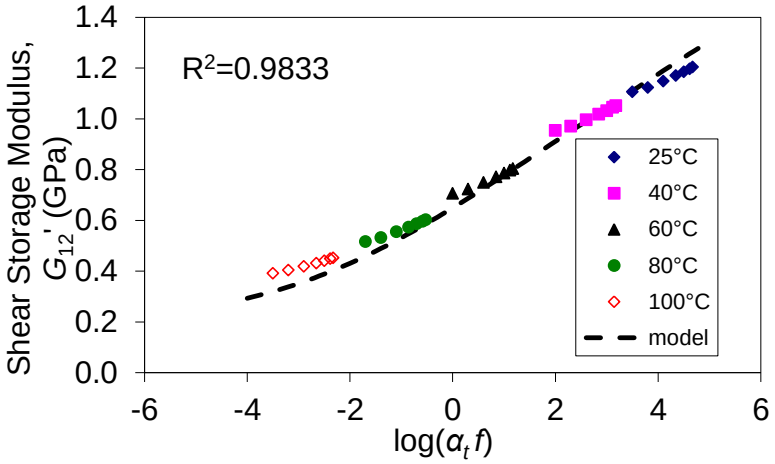

Figure **5-33**: Experimental and modeled shear storage modulus vs. log reduced frequency — 30748

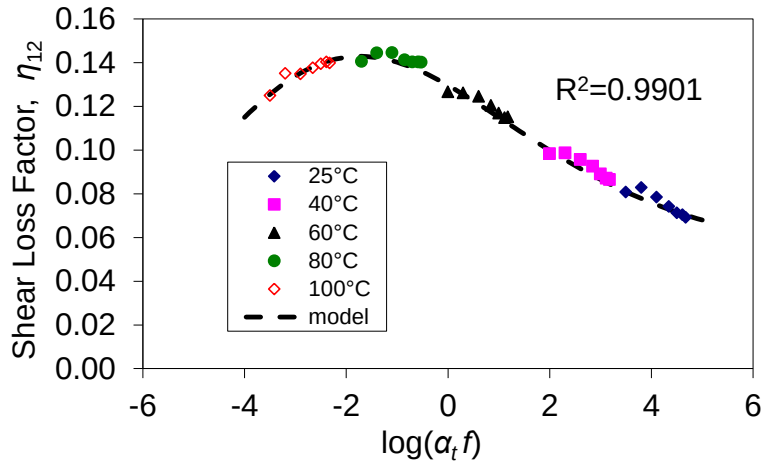

Figure **5-34**: Experimental and modeled shear loss factor vs. log reduced frequency — 30748

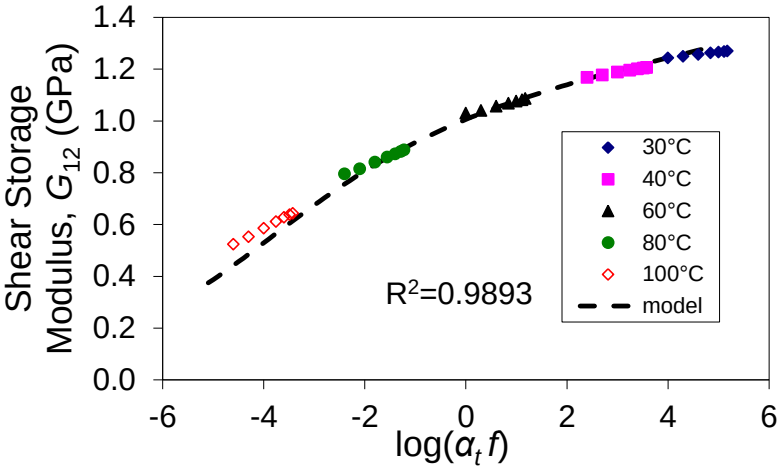

Figure **5-35**: Experimental and modeled shear storage modulus vs. log reduced frequency — 30757

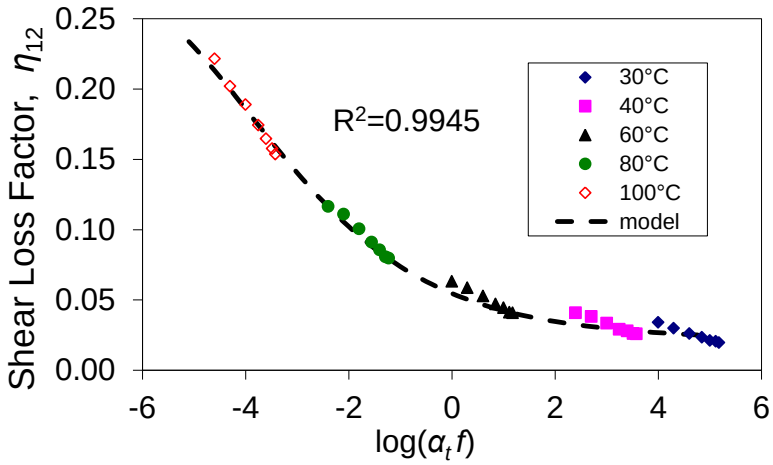

Figure **5-36**: Experimental and modeled shear loss factor vs. log reduced frequency — 30757

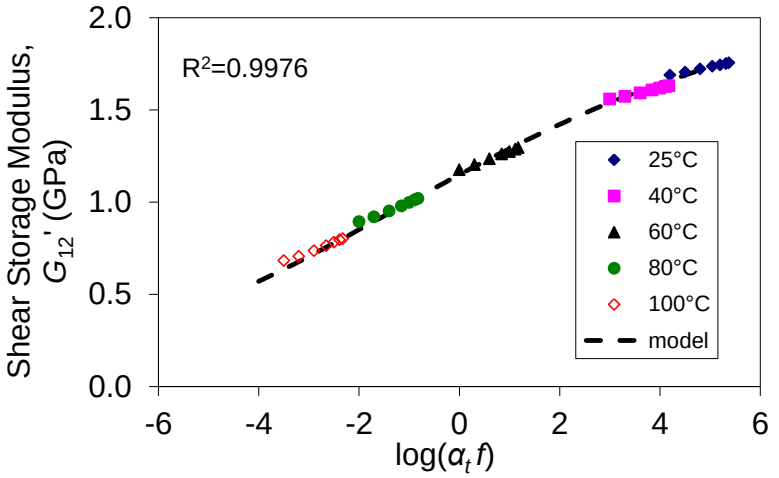

Figure **5-37**: Experimental and modeled shear storage modulus vs. log reduced frequency — 30918

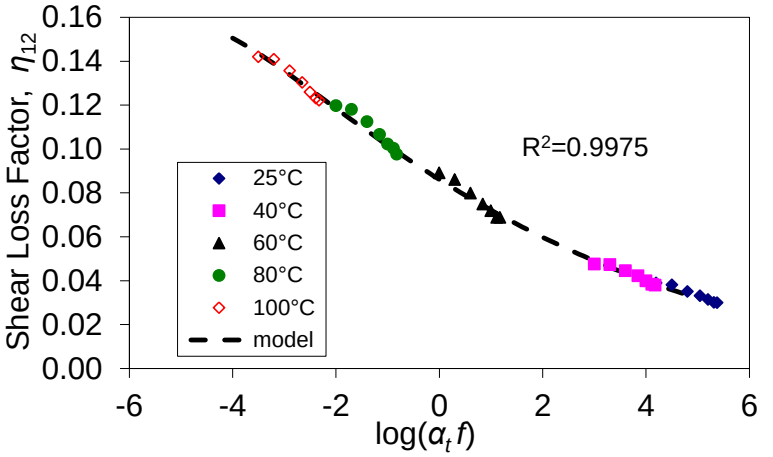

Figure **5-38**: Experimental and modeled shear loss factor vs. log reduced frequency — 30918

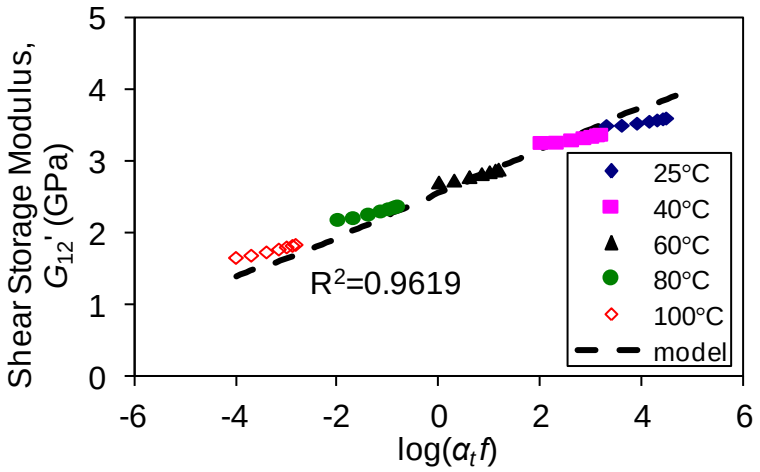

Figure **5-39**: Experimental and modeled shear storage modulus vs. log reduced frequency — 30917

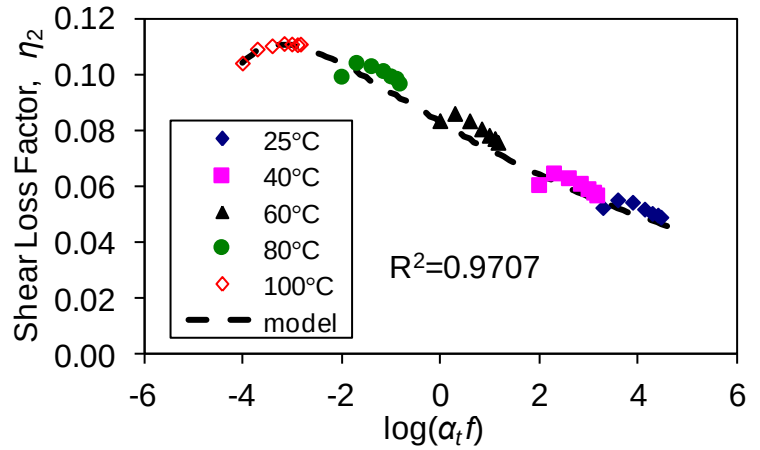

Figure **5-40**: Experimental and modeled shear loss factor vs. log reduced frequency — 30917

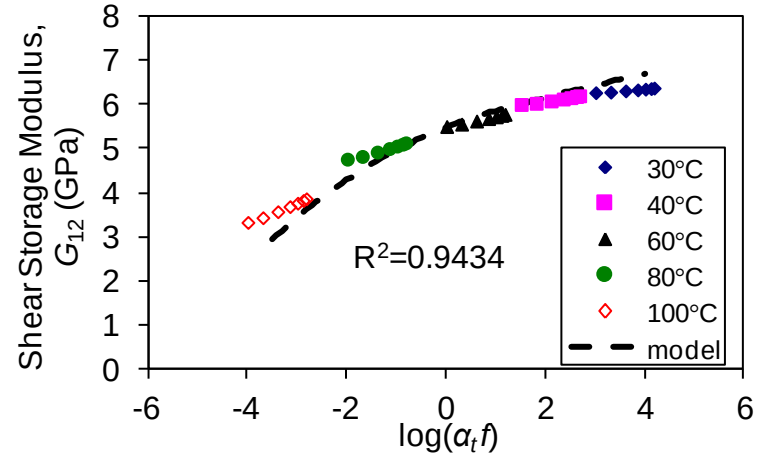

Figure **5-41**: Experimental and modeled shear storage modulus vs. log reduced frequency — EPON 862

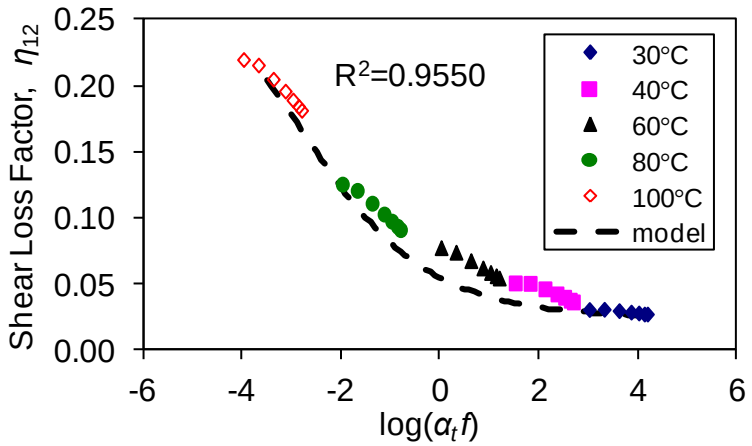

Figure **5-42**: Experimental and modeled shear loss factor vs. log reduced frequency — EPON 862

Table **5-2** Fractional derivative model and WLF equation fit constants for torsional DMA

Parameter \ Resin	LF750	30748	30757	30918	30917	EPON 862
G_{12}	7.28E-02	1.83E-01	4.35E-02	2.41E-01	3.43E00	7.27-01
a_1	9.32E-01	1.47E+00	4.62E+00	2.02E+01	7.24E+01	-2.89E-00
b_1	2.76E+01	2.52E-02	2.90E+02	0.00E+00	-4.79E+01	9.57E+01
β_1	2.49E-01	1.84E-01	2.61E-01	1.87E-01	2.31E-01	3.20E-01
a_2	2.27E+00	4.92E-02	7.02E+00	2.52E+01	8.96E+01	1.48E+01
b_2	8.81E-04	7.94E+00	8.82E-04	2.20E+02	1.68E+02	-4.10E-01
β_2	1.62E-01	2.18E-01	2.33E-01	3.01E-01	2.95E-01	3.28E-01
C_1	-1.31E+02	-2.46E+01	-6.70E+01	-1.61E+01	-9.30E+01	-4.57E+10
C_2	1.10E+03	2.47E+02	5.43E+02	140.23349	8.95E+02	4.64E+11

As with the bending DMA test results, as temperature goes down and frequency goes up, storage modulus increases and loss factor decreases. Some of the materials such as LF750, 30748, and 30917 show a decreasing loss modulus with increasing temperature (Fig. **5-43**). This behavior is advantageous in that it promotes self-stabilizing heating during cyclic loading. 30757 has the lowest loss modulus at temperatures a driveshaft might encounter. EPON 862 is excluded

from Fig. **5-43** because EPON 862 has a loss modulus of up to four times that of the polyurethanes which would obscure these trends. Fig. **5-44** shows all the data together. On a reduced frequency scale, higher temperatures are more negative numbers. Clearly, the epoxy composite has a much higher shear loss modulus than any of the polyurethane composites at higher temperatures.

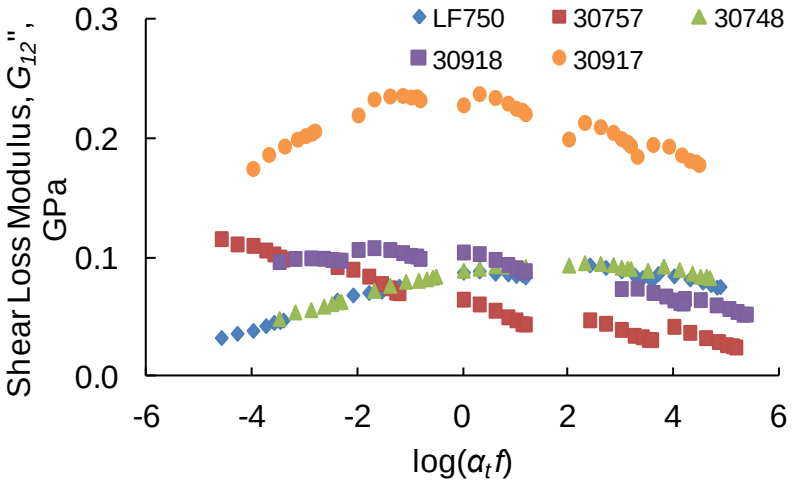

Figure **5-43**: Shear loss modulus vs. log reduced frequency comparison

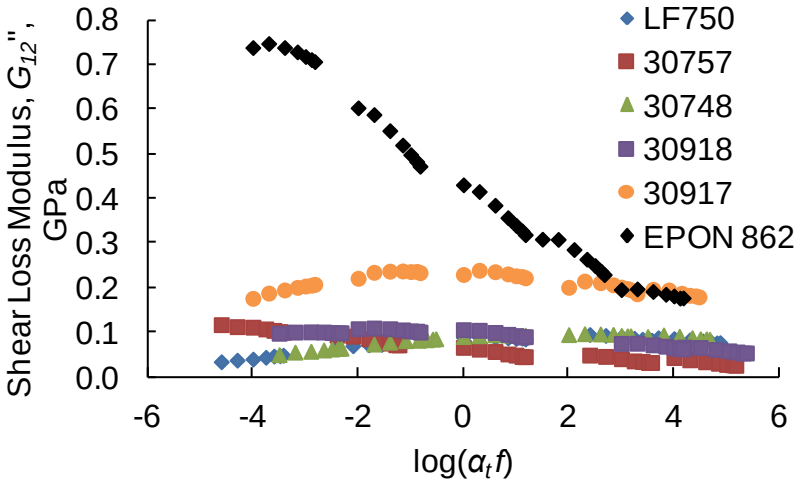

Figure **5-44**: Shear loss modulus vs. log reduced frequency comparison with EPON 862

5.3 Spin Testing of Shafts

A viscoelastic self-heating model of a spinning composite shaft was created by Shan and Bakis (2009) to predict the steady state temperature of a spinning shaft under the condition of uniform bending strain with no applied torque. Among the inputs are the inner and outer diameter of the shaft (Table **2-19**), laminate layup, applied flexural strain, rotation speed, and ambient temperature. The longitudinal ply modulus, E_1, is considered constant (Table **4-7**), as is the longitudinal Poisson's ratio, ν_{12} (Table **4-5**). The fiber direction loss factor, η_1, was found by using 0.0015 from Gibson (2007) in a RoM approach. The shaft is modeled as a layered medium, with discrete $+\theta$ and $-\theta$ plies, each of which is transversely isotropic and homogeneous. The out-of-plane Poisson's ratio, ν_{23}, is estimated in terms of the quasi-static transverse modulus, E_2, using the empirical relationship developed by Sollenberger (2010),

$$\nu_{23} = 0.0397E_2 + 0.9322 \tag{30}$$

The quasi-static values of E_2 used in equation (30) are given in Table **4-5**. The transverse shear modulus, G_{23}, is calculated using the usual expression for transversely isotropic media,

$$G_{23} = \frac{E_2}{2(1+\upsilon_{23})} \tag{31}$$

The out-of-plane properties E_3 and G_{13} are assumed to be equal to their 2-direction counterparts. Finally, the dynamic transverse and shear storate moduli and loss factors as functions of temperature and loading frequency are described in Tables **5.1** and **5.2**, respectively. Sollenberger (2010) modified the shaft heating analysis of Shan and Bakis (2009) to include multi-angle laminates. This modified analysis is used in the present investigation for comparison to the spin test results.

Before running a spin test, the maximum tensile and compressive flexural strains applied to the shaft were measured as described in Section 3.2.3 for several different pin positions of the tailstock of the spin rig. The results of a set of strain measurements for a [±45/±45] LF750 shaft

are given in Fig. **5-45**. The average coefficient of variation for the four strain levels shown was less than 5 %. The magnitudes of the compressive and tensile strains were approximately equal, with compressive strains around 2-3 % higher than tensile strains, on average, for all pin locations. The flexural strain used as input to the self-heating code for a particular pin location of the tailstock is equal to the average of the absolute value of tensile and compressive strains at all measurements positions along the length of the shaft. The strain measurements for other shafts under investigation in this research had very similar uniformity conditions along the length of the shafts, with compressive strains around 2-4 % higher than tensile strains and the coefficients of variation in the average strain measurements being no larger than 7 %.

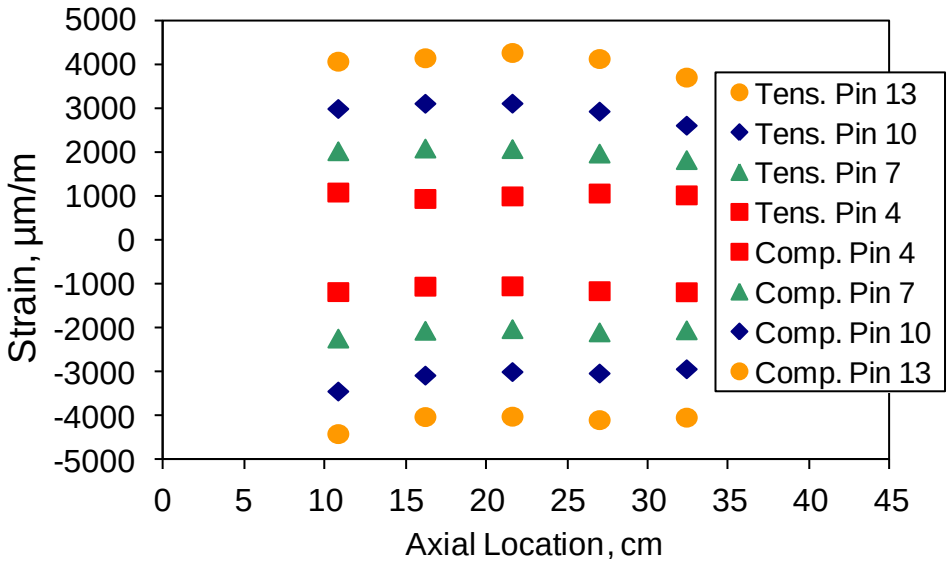

Figure **5-45**: Strain vs. axial location for [±45/±45] LF750 shaft

Each pin hole location has a specific uniform strain pattern associated with it (Appendix C). Unfortunately, as stiffer materials are tested in the rig, they resist the misalignment and carry a strain that is lower than mathematical theory would suggest. Shafts tested with 45° plies deviate from the theoretical strain less than 30° plies. For the shafts in this investigation, the experimentally determined strain was, on average, between 1-15 % lower than theory for LF750,

between 8-18 % lower than theory for 30917, and between 7-28 % lower than theory for EPON 862.

The temperature of the tubes was measured using three IR thermocouples. Two of the thermocouples measured the temperature at the left quarter-span location and the midspan location. A third, mobile thermocouple measured the temperature at 3*L*/8, 5*L*/8, and 3*L*/4, measuring from the left end, where shaft length L = 18 cm. The temperature of representative shaft over time is presented in Fig. **5-46**. The initial warm-up of the shaft and thermal equilibration are shown. The mobile thermocouple was positioned in the three locations labeled by distance from the left end (corresponding to the 3*L*/8, 5*L*/8, and 3*L*/4 positions mentioned previously). The ambient temperature in the room where the spin testing was run is indicated by the RT thermocouple.

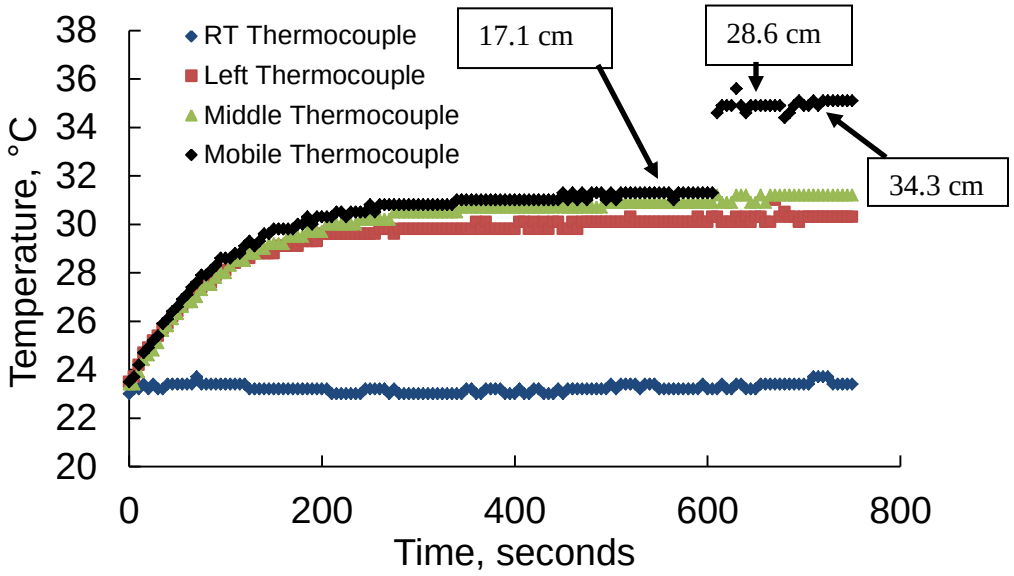

Figure **5-46**: Temperature vs. time [±45/±45] 30917 shaft, 2731 με, 1200 RPM

The temperature, as mentioned in Section 3.2.3, is measured at four different strains and three different speeds. Measurements of steady-state temperature change (versus room temperature) for a [±45/±45] LF750 shaft are presented in Fig. **5-47**. The temperature change

increases with increasing strain amplitude and increasing speed. The temperature versus axial location graphs in Fig. **5-47** show that the uniform strain shown in Fig. **5-45** resulted in a uniform temperature distribution at the investigated shaft speeds and flexural strain amplitudes.

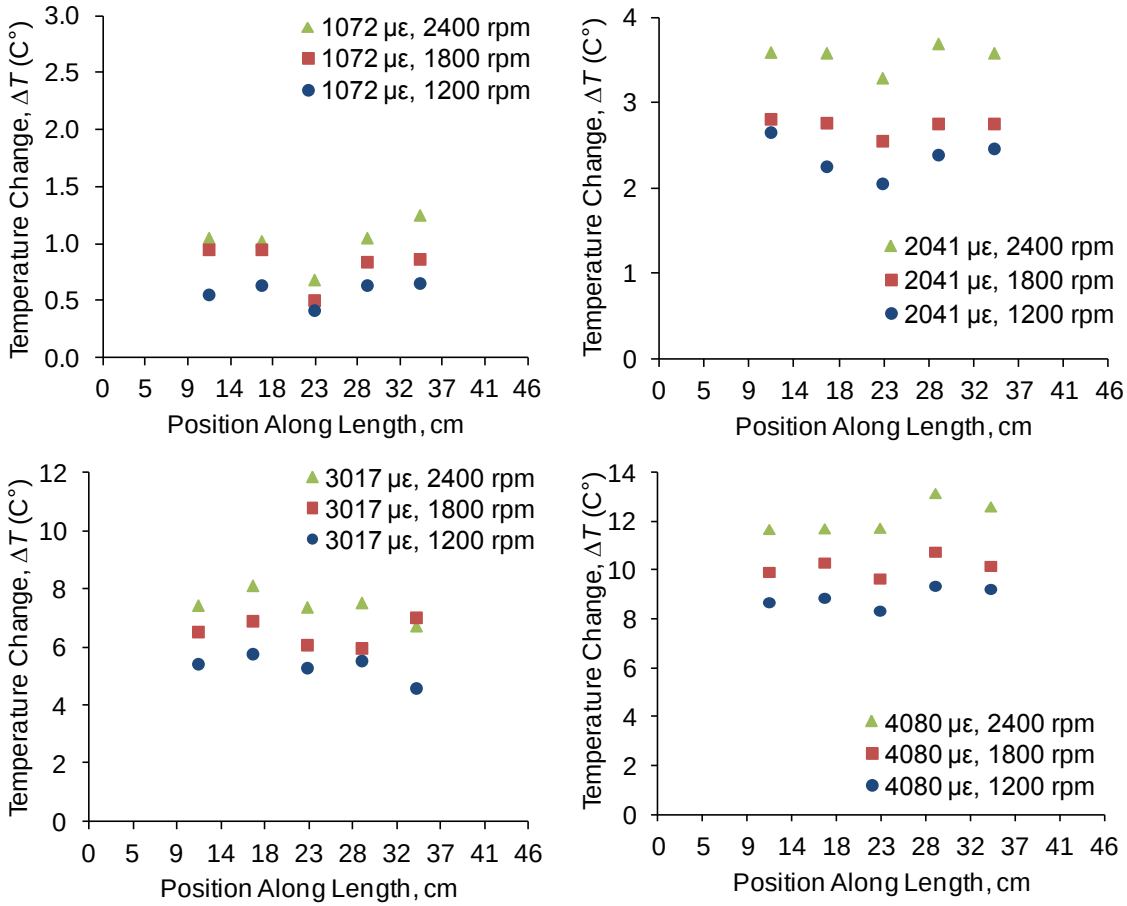

Figure **5-47**: Temperature change vs. axial position, [±45/±45] LF750

The average temperature change, Δ*T,* along the length for a given strain and speed is compared against the model prediction in Fig. **5-48**. The model prediction is, on average, higher than the average shaft temperature by less than 1 °C, with the highest discrepancy at the highest flexural strain. It is important when comparing the self-heating model to the experiment to make sure that the shear and transverse strain amplitudes are similar to those used to generate the model parameters in Tables **5-1** and **5-2**. In a [±45/±45] shaft, a flexural strain of 2500 με will cause

very little strain in the 2-direction but about 5000 με in shear, and also the shear loss factor is two orders of magnitude larger than all other loss factors, longitudinal and transverse, for a [±45/±45] shaft. That means that the amount of heat generated by the shaft should be dominated by dynamic shear losses. Based on the DMA test parameters, the self-heating model should be most accurate at a flexural strain of around 2500 με. The measured temperature changes in Fig. **5-47** are within 0.5 °C of the self-heating model until flexural strains exceed 3000 με, supporting this explanation.

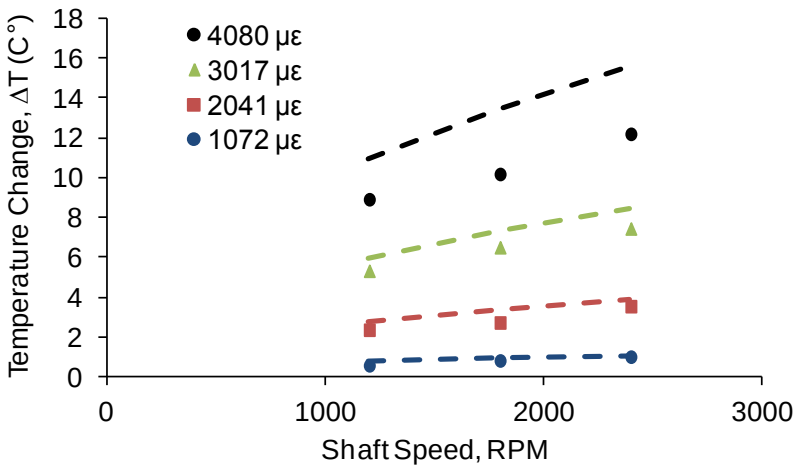

Figure **5-48**: Temperature change vs. shaft speed, [±45/±45] LF750

Two multi-angle laminates were investigated in this research, [±45/±30] and [±30/±45]. In these laminates, a flexural strain of 1200 με in the 30 deg. ply results in a 2-direction strain of 1700 με and a shear strain of 3300 με. In a multi-angle laminate such as [±45/±30] (Fig. **5-49**) or [±30/±45] (Fig. **5-50**) the model should match the self-heating in a 45 deg. ply best at a flexural strain of 2500 με and the 30 deg. ply best at 1200 με. The theoretical predictions for those two shafts were on average low by less than 2 °C. The heating model predictions for the [±30/±30] laminate (Fig. **5-51**) were on average less than 0.5 °C high. The temperature predictions do not greatly vary from the experimental results until after 1200 με which makes sense because at that

strain the DMA data should be the most accurate for the ±30 deg. plies. The heating prediction is more accurate for angle ply laminates than multi-angle laminates for LF750.

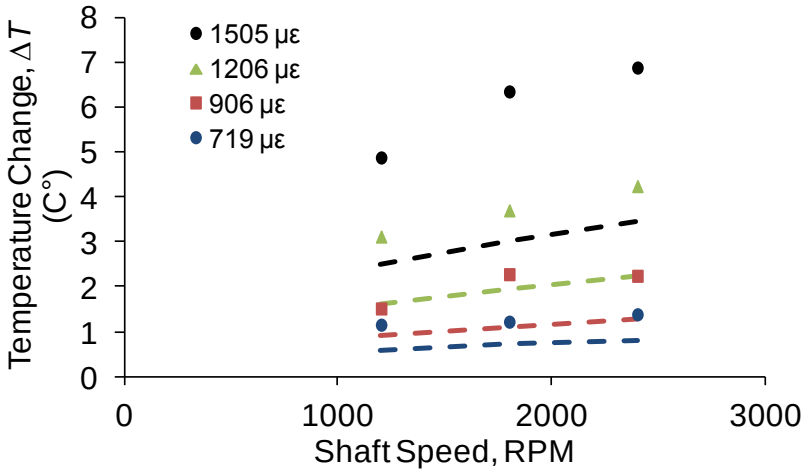

Figure **5-49**: Temperature change vs. shaft speed, [±45/±30] LF750

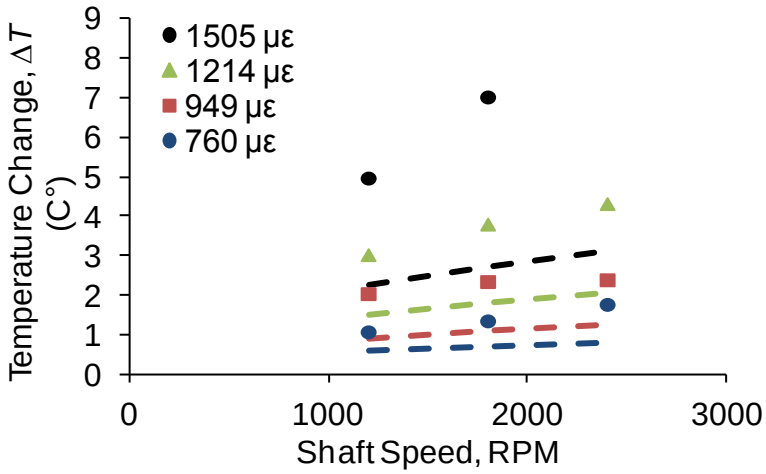

Figure **5-50**: Temperature change vs. shaft speed, [±30/±45] LF750

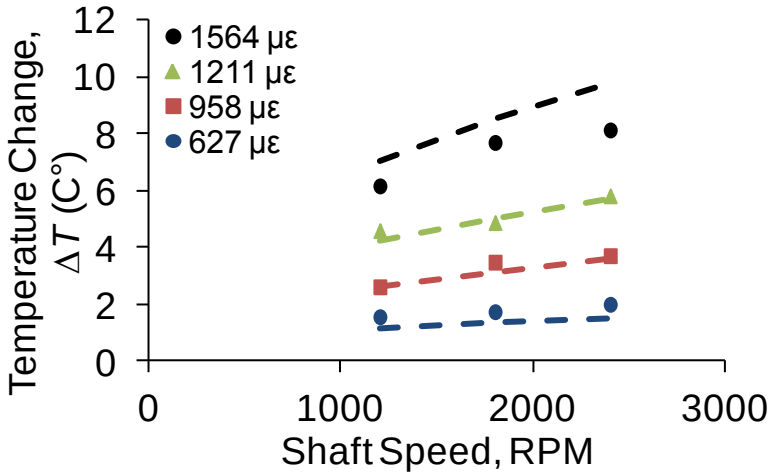

Figure **5-51**: Temperature change vs. shaft speed, [±30/±30] LF750

The polyurethane resin 30917 was chosen because of its relatively low transverse loss modulus compared to the other resin systems from room temperature to 70 °C. 30917 also has higher values for fiber direction compression strength and transverse direction tensile strength which are limiting factors in driveshaft design. For this material system, the self-heating model under-predicts the heating of the 30917 shaft by 0.5 °C on average (Fig. **5-52a**). A bending strain of 1500 με in a 30° ply results in a transverse strain of 1700 με and a shear strain of 3700 με, which are both very close to the respective strain amplitudes used in the DMA tests. For the strains and speeds tested, the heating model is able to predict the heating of several additional laminates (Fig. **5-52b, c, and d**) up to at least a strain of around 2400 με.

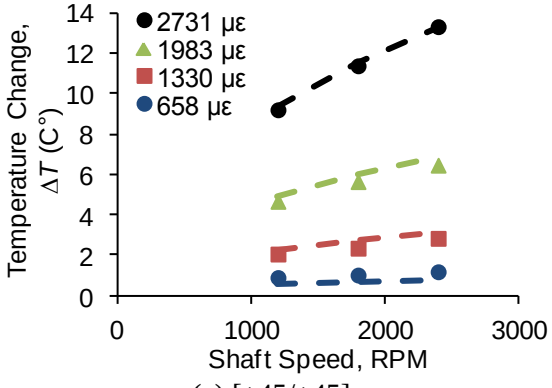

(a) [±45/±45]

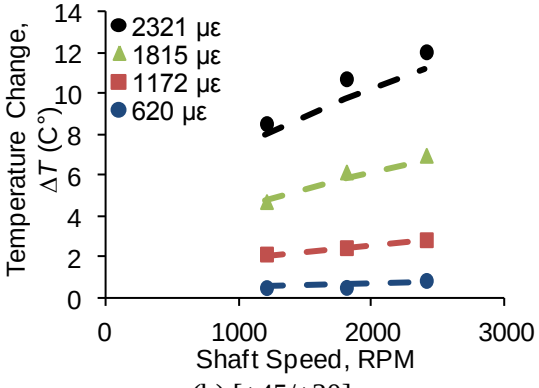

(b) [±45/±30]

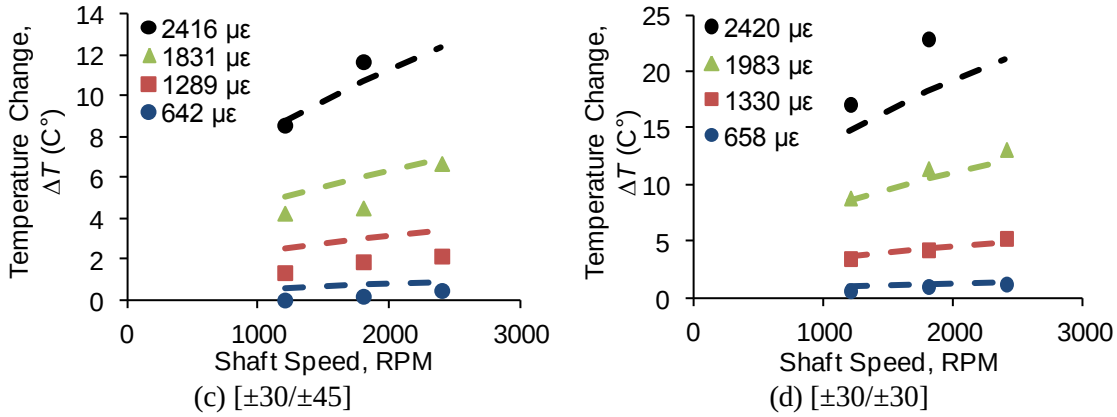

Figure **5-52**: Temperature change vs. shaft speed, 30917

The final material tested in the spin rig was EPON 862 (Fig. **5-53**). EPON 862 is interesting because of the low transverse loss modulus but also high shear loss modulus behavior it exhibits relative to polyurethanes. This could cause composite shafts with EPON 862 resin to have unstable heating when their generated heat is shear dominated. It was found out during testing shafts that EPON 862 exhibit non-stable self-heating which results in failure of the shaft at strains above 2000 με. Spinning at a higher RPM, around 2400 RPM, rapidly accelerates this instability. A flexural strain of 2400 με corresponds to a transverse strain of 1700 με and a shear strain of 4800 με in a 30 deg. ply and a shear strain of 3000 με in a 45 deg. ply. The model should then be accurate for a flexural strain of 2400 με, but the material does not exhibit stable heating at this strain. For instances where the shafts heating was stable at strains higher than 2000 με (Fig. **5-53c**) the temperature increase is highly under predicted by the heating code. The heating model on average under-predicts the heating of the epoxy tubes by less than 1-2 °C for flexural strains less than 2000 με, on average.

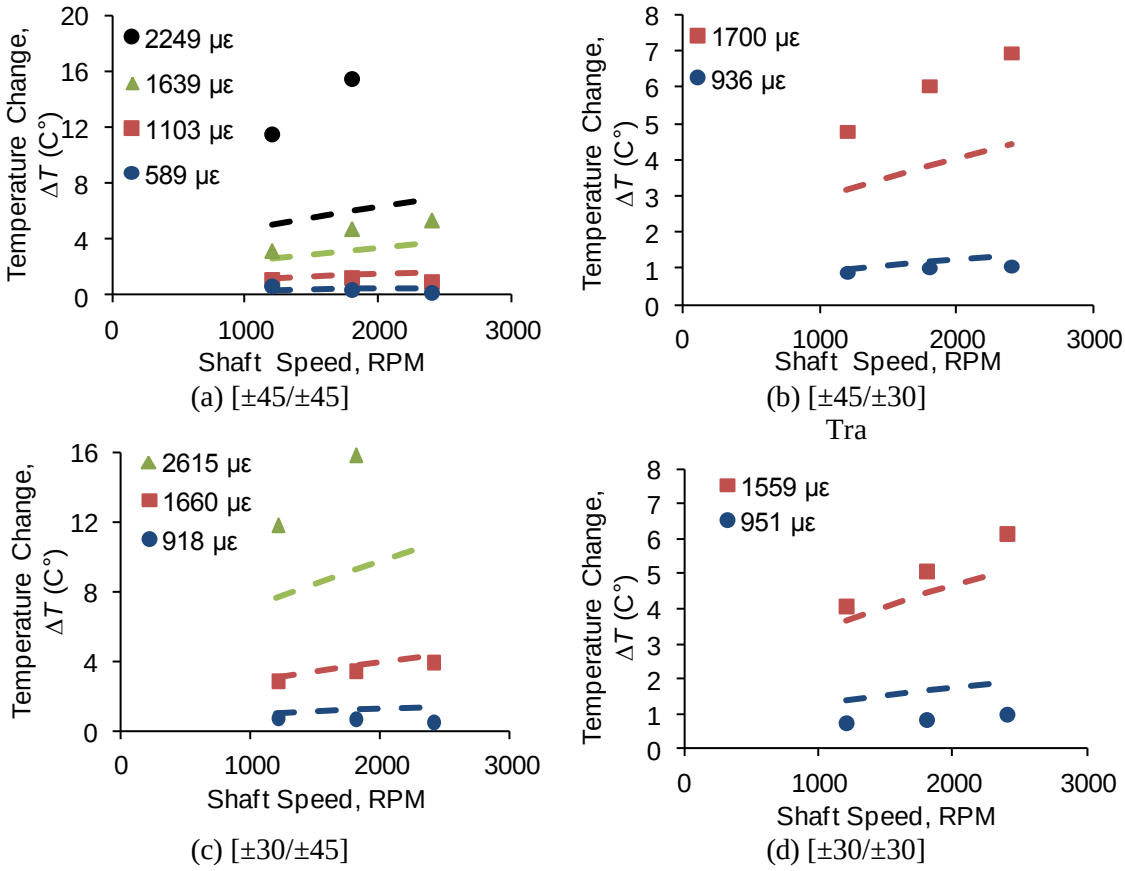

Figure **5-53**: Temperature change vs. shaft speed, EPON 862

The spin tests have shown that for different materials, different laminates, and different speeds, and different strains the heating model can predict the temperature increase within about 1.1 °C (Table **5-3**) on average. In the strain range that a helicopter driveshaft might experience (less than 1500 με) the heating model prediction is accurate to 0.7 °C on average. This is important because it gives confidence in using the dynamic values gathered in Sections 5.1 and 5.2 for use in designing a helicopter driveshaft.

Table **5-3** Absolute difference in temperature change between experiment and model

Resin Material	Laminate	Avg. Temp. Change Difference, $\Delta\Delta T$	
		0-2000 με	All Strains
LF750	[±45/±45]	0.3	1.1
	[±45/±30]	1.6	1.6
	[±30/±45]	1.7	1.7
	[±30/±30]	0.5	0.5
30917	[±45/±45]	0.3	0.3
	[±45/±30]	0.1	0.3
	[±30/±45]	0.8	0.8
	[±30/±30]	0.4	0.9
EPON 862	[±45/±45]	0.6	1.9
	[±45/±30]	1.1	1.1
	[±30/±45]	0.4	1.7
	[±30/±30]	0.7	0.7
Average		0.7	1.1

Chapter 6

Conclusions and Recommendations

6.1 Conclusions

- The transverse compression and tension moduli measured from a four-point bend test are approximately the same within the margin of data scatter. It should be noted that the transverse compression modulus of a hoop wound tube was around 5% smaller than the four-point compression modulus. It is therefore likely that the tension strength and modulus of a hoop wound tube may not be identical to the values found in four-point bending. A hoop wound tube test may be a more accurate representation of a composite driveshaft but the test requires expensive collet grips or the tube to bonded or faceted to end fixtures.

- It was found that winding pattern did not significantly affect the axial modulus of elasticity of laminated tubes, but did have a profound effect on the compressive strength. Using different fiber winding patterns through the thickness of the laminate prevents the formation of bands of microbuckled fibers at coincident locations through the wall thickness of the tubes, thereby increasing compressive strength.

- A tubular $[\pm\theta/89/\pm\theta]$ specimen for determining the fiber-direction modulus (E_1) and compressive strength (F_{1c}) including the effects of fiber undulation was developed. The key feature of the specimen is that the longitudinal Poisson's ratio is limited to a small value to eliminate specimen "barreling" during compression testing so that the stresses

and strains can be predicted by classical laminate plate theory (CLPT). Control of the deformed shape is accomplished by introducing a single hoop-wound ply to the angle-ply laminate. Once the ply elastic properties besides E_1 have been determined by other tests, E_1 can be backed out using CLPT. As well, a value of F_{1c} that is independent of shear stress can be backed out by extrapolating the tube strength results to the case where $\theta = 0$ degrees. The E_1 value determined by this method was found to apply to a wide range of laminates and is therefore considered useful for design purposes. On the other hand, the F_{1c} values depended on winding pattern, and therefore cannot be applied to general laminates without further investigation.

- Power law relationships were used to fit the matrix-influenced ply strengths and elastic moduli (longitudinal compression, transverse compression and tension, and longitudinal shear) for various flexible and rigid resins. It was found that the power law expressions fit reasonably well to the experimental data for resin moduli ranging from 245 MPa to 2950 MPa. These empirically derived equations are of high value because they allow for new potential resins to be evaluated without large expenditures of time invested in experimentally determining the failure strengths and elastic moduli.

- The transverse and shear dynamic properties of several resins were characterized for a wide range of temperatures and frequencies. A WLF shifting equation and fractional derivative model were successfully used to shift the DMA data into master curves. It was found that the measured dynamic stiffness of the material is dependent on the strain amplitude in the test. No clear relationship was found between the neat resin modulus and the dynamic response of the material, or between the strain amplitude and the

dynamic response. It is therefore vital that the strain amplitude be chosen such that is matches as closely as possible with the design case in mind.

- The dynamic shear loss modulus for a composite with EPON 862 resin was found to be up to four times higher than polyurethane with the opposite trend for dynamic transverse loss modulus. Composite shafts made of EPON 862 resin were found to overheat, often unstably, resulting in failure of the shaft at strains above 2000 με.

- It was found that the heating model best agrees with the experimental data in the strain range of which the dynamic tests were conducted. Various laminates and resin systems were tested with the prediction on average within 1.1 ℃ of the experiment. Overall the composite shafts were poorly modeled at strains above 2000 με depending somewhat on laminate. This result is valuable because it supports the experimental values collected which can then be used in design codes to determine whether a FMC class material can replace a segmented metallic driveline.

6.2 Recommendations for Future Work

Future work should focus on developing a better understanding of the effect of fiber undulations and filament winding pattern on the fiber direction compression strength and modulus of a tube. The weight of an optimized driveline is influenced by the fiber direction compressive strength of the composite. The investigation of the effects of filament winding pattern was developed in this research was preliminary. In this investigation, an inside/outside winding pattern ratio of 2/1 was used but other pattern ratios should be investigated.

Working with industry partners to develop a resin system that has a larger neat resin modulus than 30917 and a smaller transverse and shear loss modulus will result in a lighter driveshaft. Also it is important to gather DMA data at the strain amplitude that is going to be present in a design case. For that reason the accuracy of the heating model could be increased by developing a relationship between the dynamic response of the material and the strain amplitude. For torsional DMA testing a strain amplitude of 5000 με was used because of the frequency limitations of the RDS-II. The heating model would be more accurate if the data was collected by another instrument at the proper strain amplitude, 3000-4000 με shear and 1500-2000 με transverse, and proper frequency. To increase the accuracy of the torsional DMA, the RDS-II more readily accepts a specimen that is more like a disk as opposed to a rod. By using a thin disk instead of a rod, the shear strain amplitude can be increased for the same angle of rotation, and more importantly the gap distance can be more exactly measured. Investigating sub-ambient temperatures which a helicopter might experience would also be of interest in DMA testing.

References

Adams, D.F., and Welsh, J.S., 1997, "The Wyoming Combined Loading Compression (CLC) Test Method," *Journal of Composites Technology and Research*, Vol. 19, No. 3, pg. 123-133

Adams, R.D., and Bacon, D.G.C., 1973, "The Dynamic Properties of Unidirectional Fibre Reinforced Composites in Flexure and Torsion," *Journal of Composite Materials*, Vol. 7, pg 53-67

ASTM Standard D 6272, 2010, "*Standard Test Method for Flexural Properties of Unreinforced and Reinforced Plastics and Electrical Insulating Materials by Four-Point Bending*," ASTM International, West Conshohocken, PA

Bagley, R.L., and Torvik, P.J., 1979, "A Generalized Derivative Model for an Elastomeric Damper," *Shock and Vibartion Bulletin*, Vol. 49, pg. 135-143

Claus, S.J., 1994, "Manufacture-Structure-Performance Relationships for Filament-Wound Composite Shells." PhD Dissertation, Department of Engineering Science and Mechanics, The Pennsylvania State University, University Park, PA

Crane, R.M., Ratcliffe, C., July 1993,"Graphite/Polyurethane Flexible Composites – Mechanical and Vibration Damping Properties," *Survivability, Structures, and Materials Directorate Research and Development Report*

Daniel, I., and Ishai, O., 2006, *Engineering Mechanics of Composite Materials*, 2nd Edition, New York: Oxford University Press

Darlow, M. S., and Creonte, J., 1995, "Optimal Design of Composite Helicopter Power Transmission Shafts with Axial Varying Fiber Layup." *Journal of the American Helicopter Society*, Vol. 40, No. 2, pg. 50-56

Ferry, J.D., 1970, *Viscoelastic Properties of Polymers*, 2nd Edition., Wiley, NY.

Gibson, R.F., 2007, *Principles of Composite Material Mechanics*, 2nd Edition, Boca Rotan, FL: CLC Press

Hannibal, A.J., and Avila, J. A., January 1984, "A Torsionally Stiff-Bending Soft Driveshaft," Prof. Reinforced Plastics/Composites Institute 39th Annual Conference, The Society of the Plastics Industry, Inc.

Hetherington, P., Kraus, R., and Darlow, M., 1990, "Demonstration of a supercritical composite helicopter power transmission shaft," *Journal of American Helicopter Society*, Vol. 35, No. 1, pg. 23-28

Ishikawa, T., Chou, T., 1982, "Stiffness and Strength Behavior of Woven Fabric Composites," *Journal of Materials Science*, Vol. 12, pg. 3211-3220

Jensen, D., and Pai, S., 1993, "Influence of Local Fiber Undulation on the Global Buckling of Filament-Wound Cylinders" *Journal of Reinforced Plastics and Composites*. Vol. 12, pg. 865-875

Jolicoeur, C. and Cardou, A., 1994, "Analytical Solution for bending of Coaxial Orthotropic Cyclinders," *Journal of Engineering Mechanics*, Vol. 120, No. 12, pg. 2556-2574

Mayrides, B., Wang, K.W., and Smith, E.C., June 2005, "Anaylsis and Synthesis of Highly Flexible Helicopter Drivelines with Flexible Matrix Composite Shafting," *Proc. 61st Forum*, Grapevine, Texas, American Helicopter Society. pg. 1-3

Ocalan, M., March 2002, "High Flexibility Rotorcraft Driveshafts Using Flexible Matrix Composites and Active Bearing Control," M.S. Thesis, The Pennsylvania State University

Roos, C., and Bakis, C.E., 2011, "Multi-Physics Design and Optimization of Flexible Matrix Composite Driveshafts," *Composite Structures* Vol. 93, pg. 2231-2240

Shan, Y., and Bakis, C.E., June 11-13 2002, "Static and Dynamic Characterization of a Flexible Matrix Composite Material," *Proc. 58th Annual Forum*, American Helicopter Society, Montreal, Canada

Shan, Y., and Bakis, C.E., June 1-3 2005, "Internal Heating Behavior of Flexible Matrix Composite Driveshaft," *Proc. 61st Annual Forum*, American Helicopter Society, Grapevine TX

Shan, Y., 2006, "Flexible Matrix Composites: Dynamic Characterization, Modeling, and Potential for Driveshaft Applications", Ph.D. Thesis, Department of Engineering Science and Mechanics, Penn State. University Park, PA

Shan, Y., and Bakis, C.E., 2009, "Viscoelastic Characterization and Self-Heating Behavior of a Flexible Matrix Composite Driveshaft," *Journal of Composite Materials*, Vol. 43, No. 12, pg. 3053-306

Shin, E., Wang, K. K., and Smith, E.C., May 2003, "Characterization of Flexible Matrix Composite Rotorcraft Driveshafts," *Proc. 59th Forum*, American Helicopter Society

Singh, S. P., Grubran, H.B.H., and Gupta, K., 1997, "Developments in Dynamics of Composite Material Shafts," *International Journal of Rotating Machinery*, Vol. 3, No. 3, pg. 189-198

Sollenberger, S., 2010, "Characterization and Modeling of a Flexible Matrix Composite Material for Advanced Rotorcraft Drivelines," MS Thesis, Department of Engineering Science and Mechanics, The Pennsylvania State University, University Park, PA

TA Instruments, 2010, *TA Instruments Dynamic Mechanical Analyzer*, Accessed from www.tainstruments.com

Zinberg, H., 1970 "The Development of an Advanced Composite Tail Rotor Driveshaft," *Proc. 26th Forum*, American Helicopter Society, pg. 1-14

Zindel, D., and Bakis, C.E., 2011, "Nonlinear Micromechanical Model of Filament-Wound Composites Consdiering Fiber Undulation," *Mechanics of Composite Materials*. Vol. 47, pg. 73-94

Appendix A: Auxiliary Data

Table **A-1**: Strength and modulus results from the investigation of winding pattern [±21/89/±21]

Specimen Name	Winding Pattern	Axial Modulus, E_x, GPa	Avg.	C_v (%)	Axial Compressive Strength, F_x, MPa	Avg.	C_v (%)	Strain at F_x, με	Avg.	C_v (%)
A21-P2-1	[2/2]	57	56	3.6	51	55	9.8	1100	1233	18.7
A21-P2-2		58			52			1100		
A21-P2-3		54			61			1500		
A22-P10-1	[10/10]	50	53	5.3	67	70	3.1	1800	1600	12.5
A22-P10-2		55			72			1600		
A22-P10-3		55			70			1400		
A22-P10_P5-1	[10/5]	61	60	11.2	74	75	6.6	1100	1400	21.4
A22-P10_P5-2		66			71			1400		
A22-P10_P5-3		53			81			1700		

Table **A-2**: Fractional derivative model and WLF equation fit constants for bending DMA — 200 με

Parameter/Resin	LF750	30748	30757	30918	30917	EPON 862
E_2	2.42E-02	3.39E-01	2.11E-01	1.57E-01	1.86E-01	5.58E+00
a_1	1.18E+00	2.75E+00	1.60E+00	1.94E-10	1.97E+00	6.26E-01
b_1	5.12E+01	1.23E+01	3.20E+01	5.50E+00	4.00E+00	1.14E+00
β_1	3.02E-01	3.34E-01	1.66E-01	2.38E-01	2.23E-01	2.42E-02
a_2	1.63E-01	4.81E-01	1.20E-04	1.29E+00	8.64E-01	8.37E-01
b_2	2.15E+01	4.74E+00	1.40E-02	2.75E+01	3.85E+01	2.79E-08
β_2	5.74E-01	6.05E-01	6.06E-01	1.71E-01	2.53E-01	9.79E-05
C_1	-1.33E+01	-1.96E+02	-3.23E+02	-1.31E+09	-3.37E+01	-4.12E+01
C_2	1.91E+02	3.78E+03	3.77E+03	1.346E+10	2.61E+02	3.18E+02

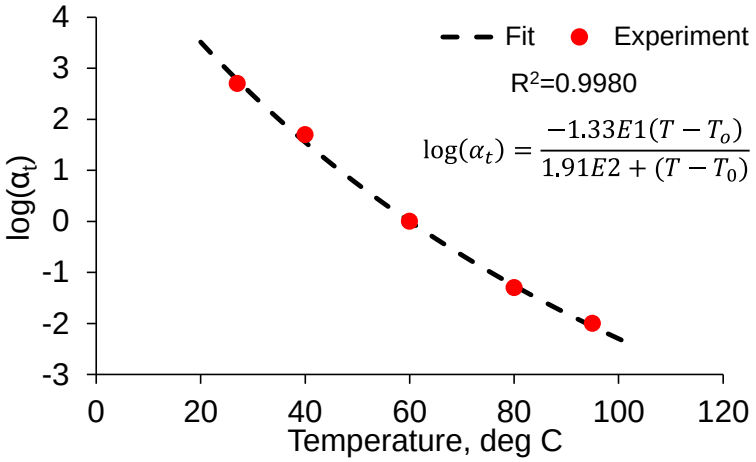

Figure **A-1**: Log temperature shift factor vs. temperature for E_2'' and η_2 — LF750, 200 με

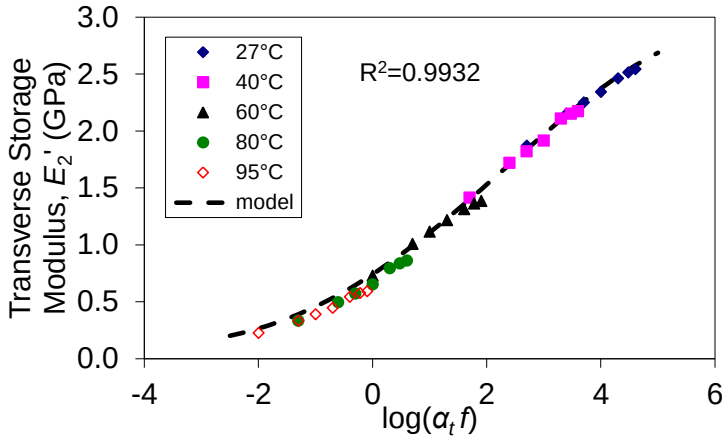

Figure **A-2**: Experimental and modeled transverse storage modulus vs. log reduced frequency — LF750, 200 με

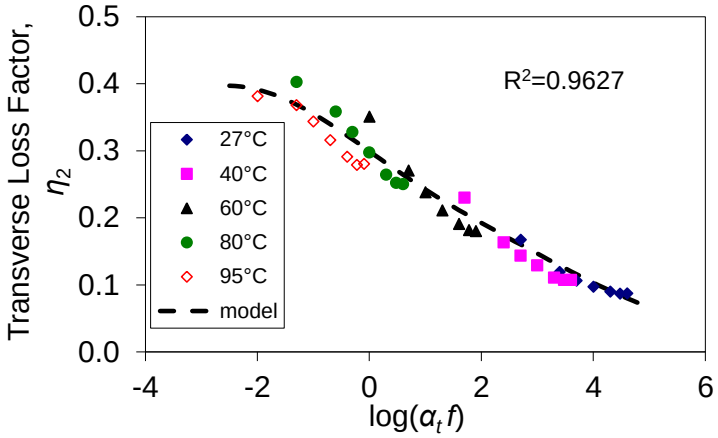

Figure **A-3**: Experimental and modeled transverse loss factor vs. log reduced frequency — LF750, 200 με

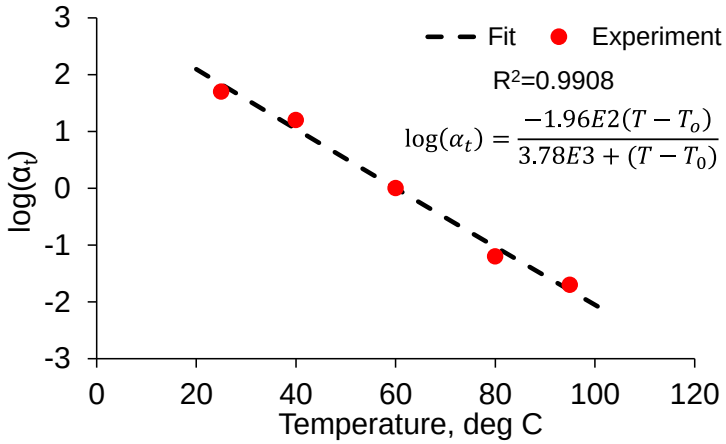

Figure **A-4**: Log temperature shift factor vs. temperature for E_2'' and η_2 — 30748, 200 με

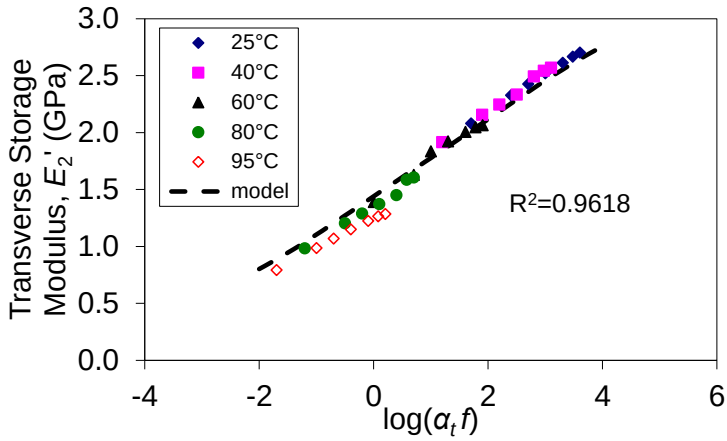

Figure **A-5**: Experimental and modeled transverse storage modulus vs. log reduced frequency — 30748, 200 με

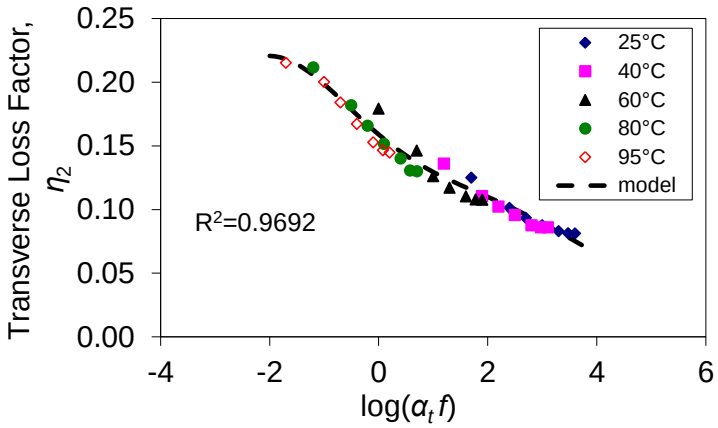

Figure **A-6**: Experimental and modeled transverse loss factor vs. log reduced frequency — 30748, 200 με

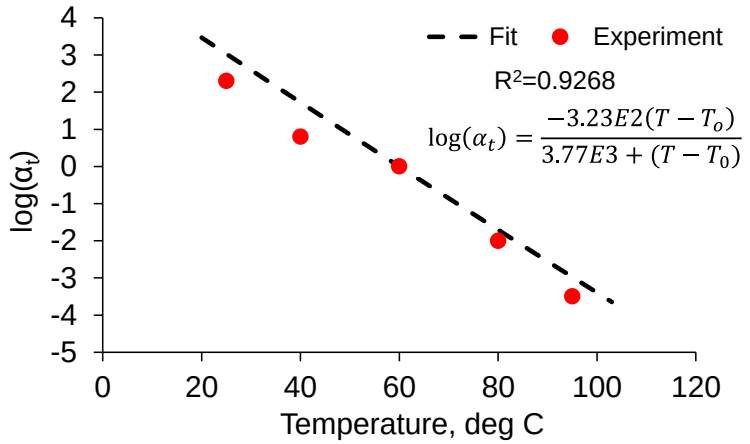

Figure **A-7**: Log temperature shift factor vs. temperature for E_2'' and η_2 — 30757, 200 με

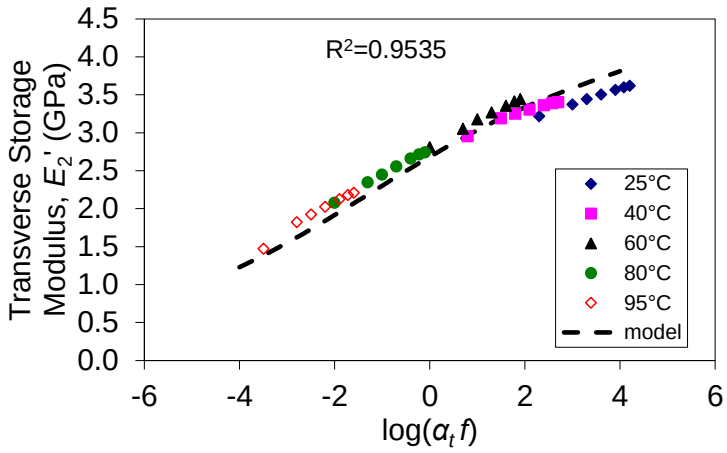

Figure **A-8**: Experimental and modeled transverse storage modulus vs. log reduced frequency — 30757, 200 με

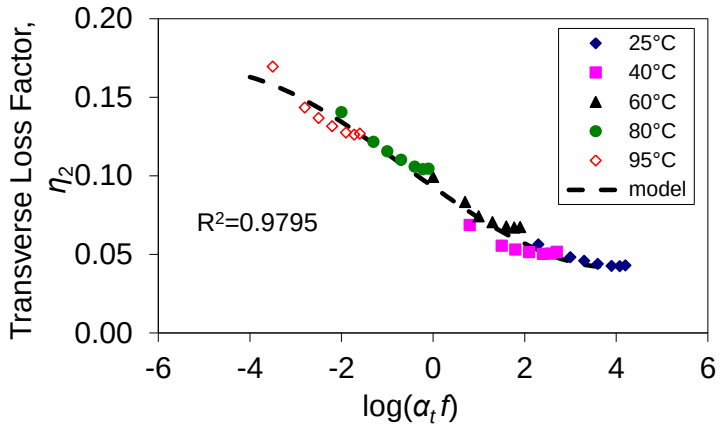

Figure **A-9**: Experimental and modeled transverse loss factor vs. log reduced frequency — 30757, 200 με

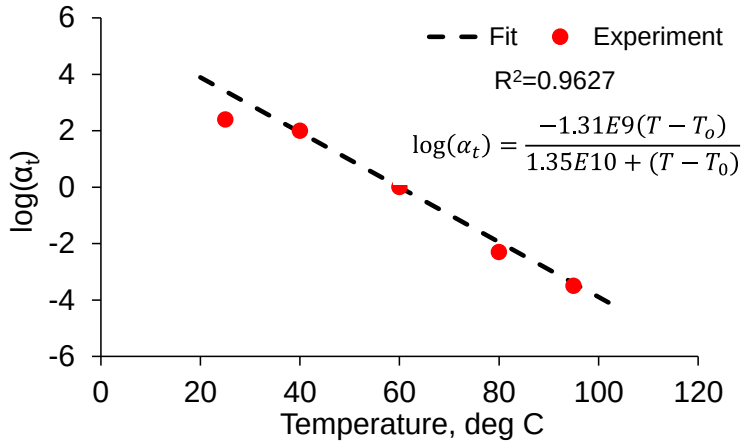

Figure **A-10**: Log temperature shift factor vs. temperature for E_2'' and η_2 — 30918, 200 με

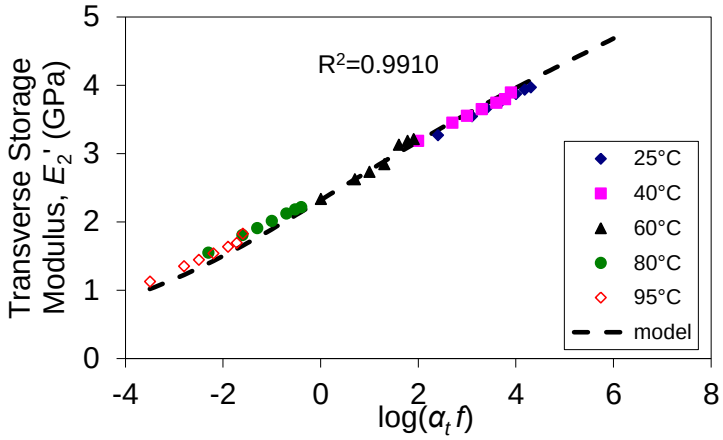

Figure **A-11**: Experimental and modeled transverse storage modulus vs. log reduced frequency — 30918, 200 με

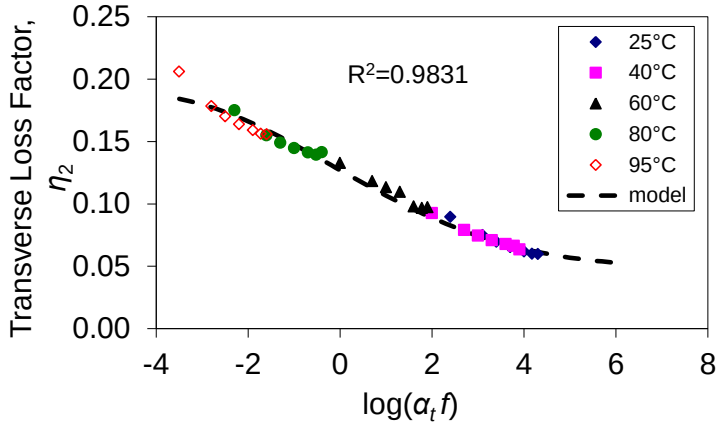

Figure **A-12**: Experimental and modeled transverse loss factor vs. log reduced frequency — 30918, 200 με

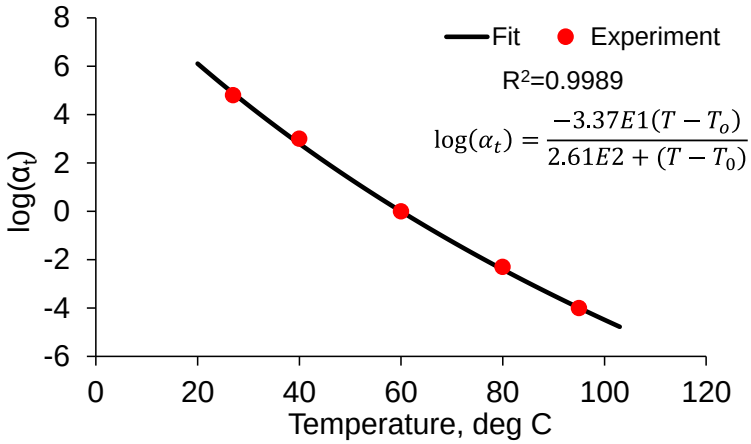

Figure **A-13**: Log temperature shift factor vs. temperature for E_2'' and η_2 — 30917, 200 με

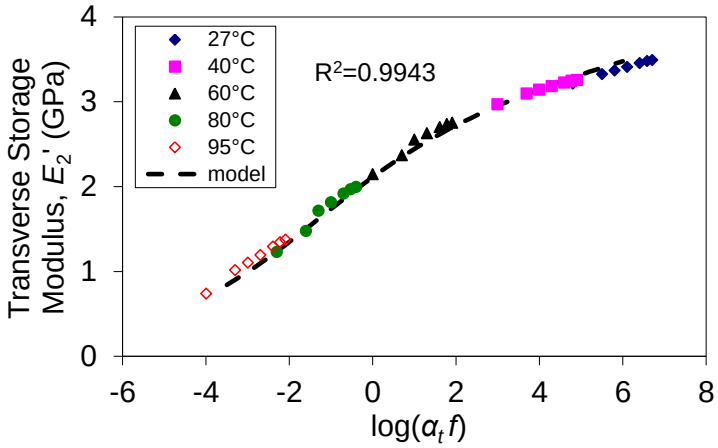

Figure **A-14**: Experimental and modeled transverse storage modulus vs. log reduced frequency — 30917, 200 με

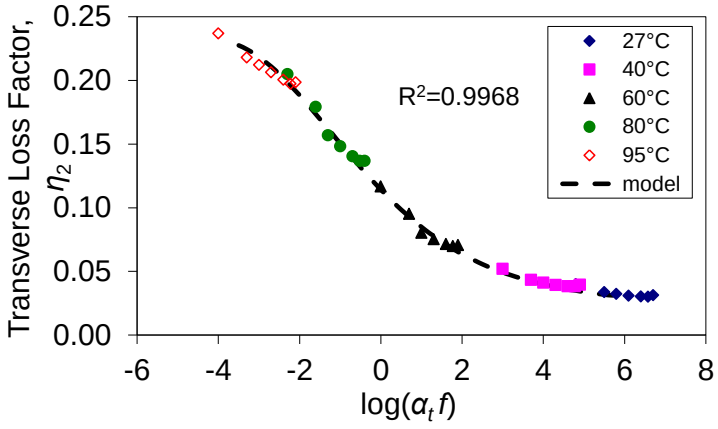

Figure **A-15**: Experimental and modeled transverse loss factor vs. log reduced frequency — 30917, 200 με

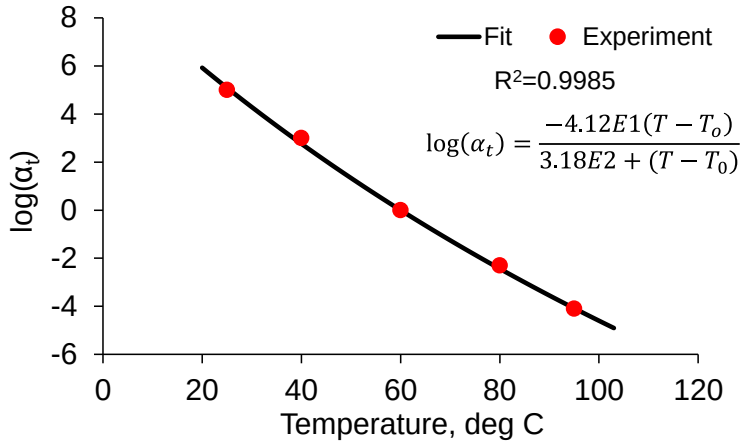

Figure **A-16**: Log temperature shift factor vs. temperature for E_2'' and η_2 — EPON 862, 200 με

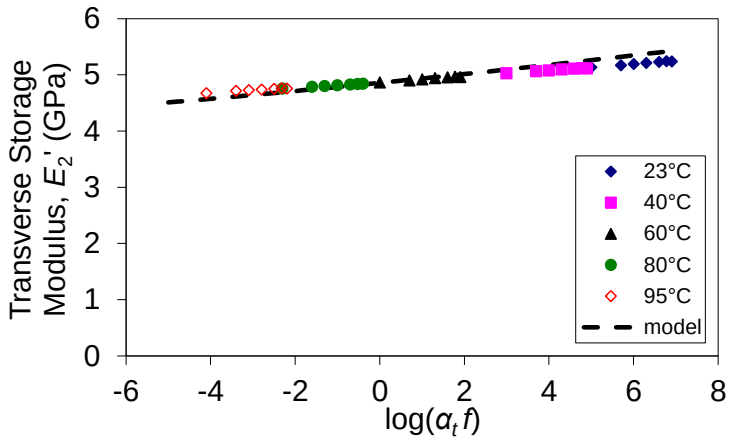

Figure **A-17**: Experimental and modeled transverse storage modulus vs. log reduced frequency — EPON 862, 200 με

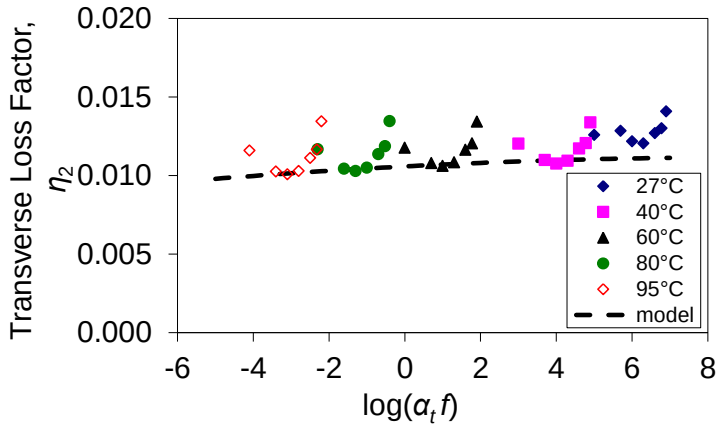

Figure **A-18**: Experimental and modeled transverse loss factor vs. log reduced frequency — EPON 862, 200 με

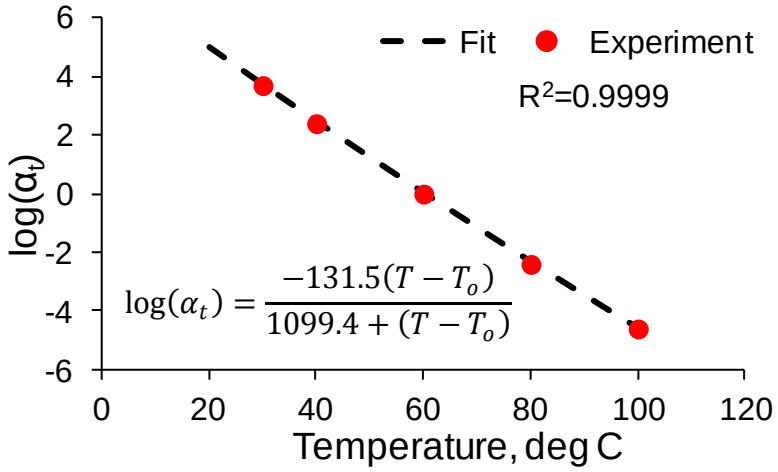

Figure **A-19**: Log temperature shift factor vs. temperature for G_{12}'' and η_{12} — LF750

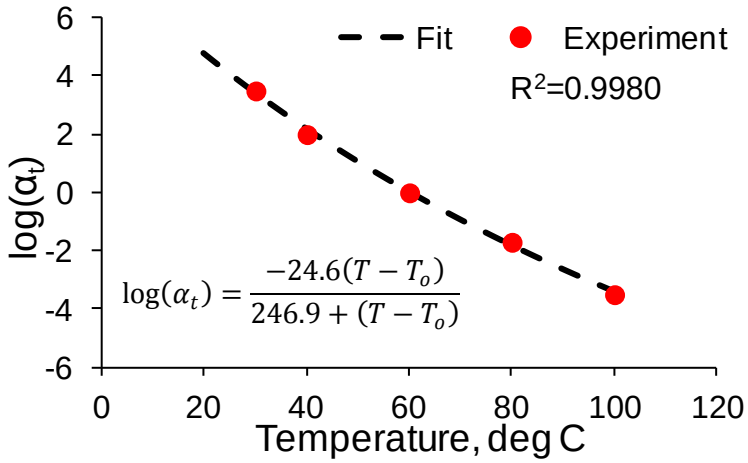

Figure **A-20**: Log temperature shear shift factor vs. temperature for G_{12}'' and η_{12} — 30748

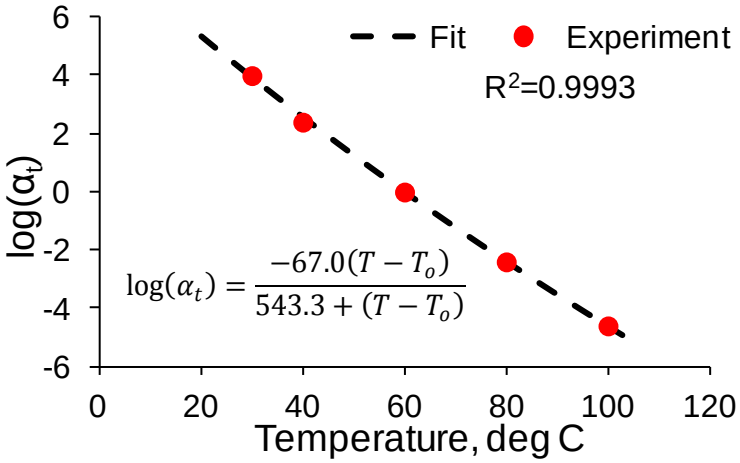

Figure **A-21**: Log temperature shear shift factor vs. temperature for G_{12}'' and η_{12} — 30757

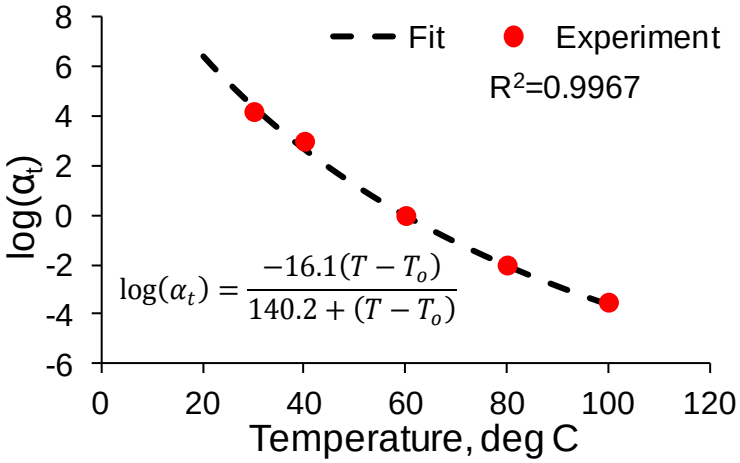

Figure **A-22**: Log temperature shear shift factor vs. temperature for G_{12}'' and η_{12} — 30918

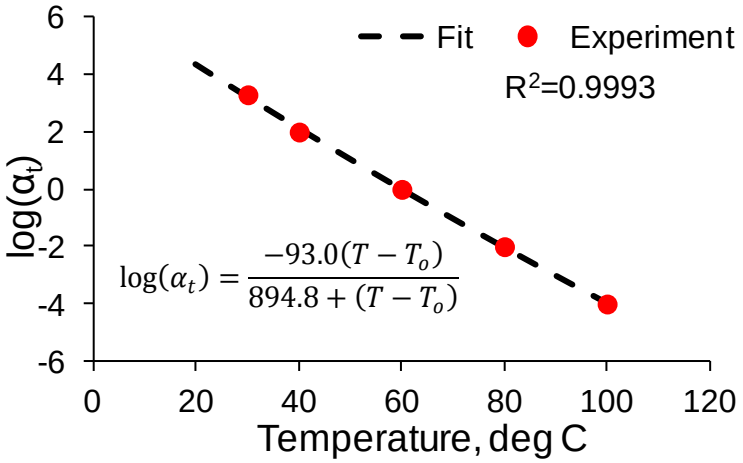

Figure **A-23**: Log temperature shear shift factor vs. temperature for G_{12}'' and η_{12} — 30917

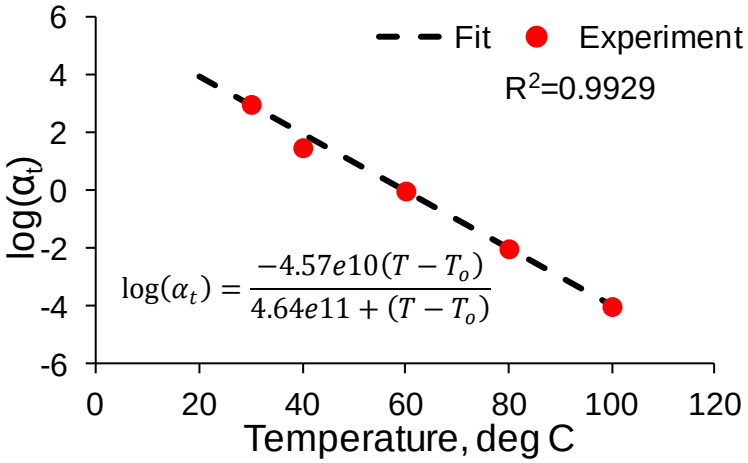

Figure **A-24**: Log temperature shear shift factor vs. temperature for G_{12}'' and η_{12} — EPON 862

Appendix B: Dynamic Shear Specimen Design

A composite rod tested in dynamic torsion experiences shear strain in a cyclic fashion presented in equation B-1,

$$\gamma_{12}(t) = \gamma_o \sin(\omega t) \tag{B-1}$$

where γ_o is the maximum amplitude of shear strain, ω is the frequency in rad/s, and t is time. The shear strain rate in the composite rod is the derivative of the shear strain expression B-1, presented in equation B-2,

$$\dot{\gamma_{12}} = 2\pi f \gamma_o \cos(2\pi f t) \tag{B-2}$$

with $2\pi f$ substituted in for ω. As an example, if the shear strain amplitude of interest is 3100 με, at a frequency, f, of 80 Hz the maximum shear strain rate is 1.558 m/m/s. The maximum frequency of the torsional DMA is only 16 Hz, so solving for shear strain amplitude in equation (B-2) with 1.558 m/m/s and 16 Hz yields 15500 με. The shear strain rate of a composite shaft is the same for shear strain amplitude 3100 με and frequency 80 Hz as for shear strain amplitude 15500 με and frequency 16 Hz. The highest shear strain amplitude that the torsional DMA is able to hold is 5000 με. Therefore the shear strain rate selected in this research was 0.503 m/m/s. The shear strain amplitude is approximately 60 % high and the shear strain rate is approximately 60 % low versus the real driveshaft case.

The torque in a composite rod is related by the equation B-3,

$$T = \frac{GJ\gamma}{r} * 10204 \tag{B-3}$$

where T is the torque in g-cm, G is the shear stiffness of the rod in Pa, J is the polar area moment of inertia in m^4, γ is the shear strain in the rod, and r is the radius of the rod. The polar area moment of inertia for a rod is (equation B-4),

$$J = \frac{\pi}{2} r^4 \tag{B-4}$$

To design a specimen for measuring the dynamic shear properties of a composite rod, the polar area moment of inertia, the maximum shear strain amplitude, and an estimate of the dynamic shear storage modulus of the rod are needed. For example, a rod with a 0.965 mm diameter (the diameter of the orifice used in this investigation) and an approximate shear modulus of 4 GPa for epoxy would require a torque of 112 g-cm. The torque must not exceed capacity of the torque measurement cell, which is 2000 g-cm in the case of the RDS-II used in this investigation.

Appendix C: Spin Rig Alignment

To apply a constant strain across a shaft in bending, the shaft must have a constant curvature. It is easiest to imagine that the shaft with constant curvature as laying on a circle (Fig. **C-1**). The strain in the shaft is related to the outer radius of the shaft, b, divided by the radius of curvature of the circle, ρ. c is half the arc length of the shaft.

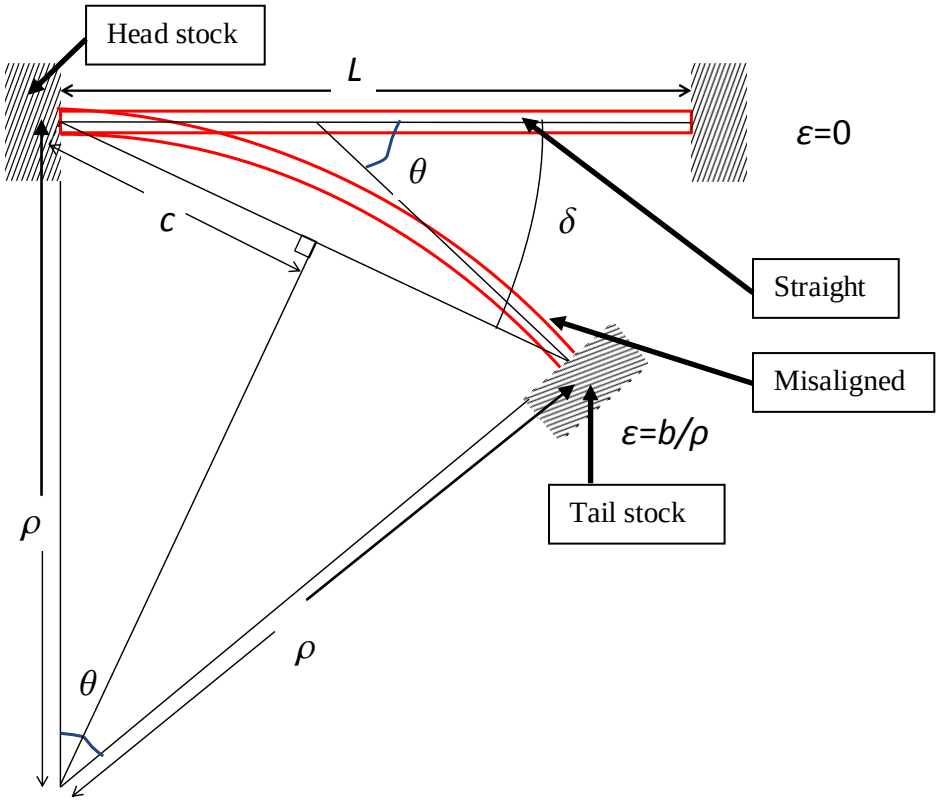

Figure **C-1**: Depiction of a shaft under straight and misaligned conditions

The head-to-tail stock misalignment angle, δ, is related to the radius of curvature and tail stock rotation, θ, by equation C-1.

$$\delta = \frac{\theta}{2} = \frac{L}{2\rho} \tag{C-1}$$

where L is the free length of the shaft between the end grips. It is important to notice that for δ to be exactly half of θ, there exists only one free length L because ρ is dependent on θ and therefore δ. For the spin testing carried out in this research the spin rig was already built, but in preliminary testing it was found that the strain was not uniform. It was hypothesized that the length between the tail and head stock of the spin rig was not correct. A misaligned shaft, as fitted into the spin rig, has three length segments: a rigid length L_L at the head stock where the tube is glued to the "left" grip, a free length L between the grips, and another rigid length L_R at the tail stock where the tube is glued to the "right" grip (Fig. **C-2**).

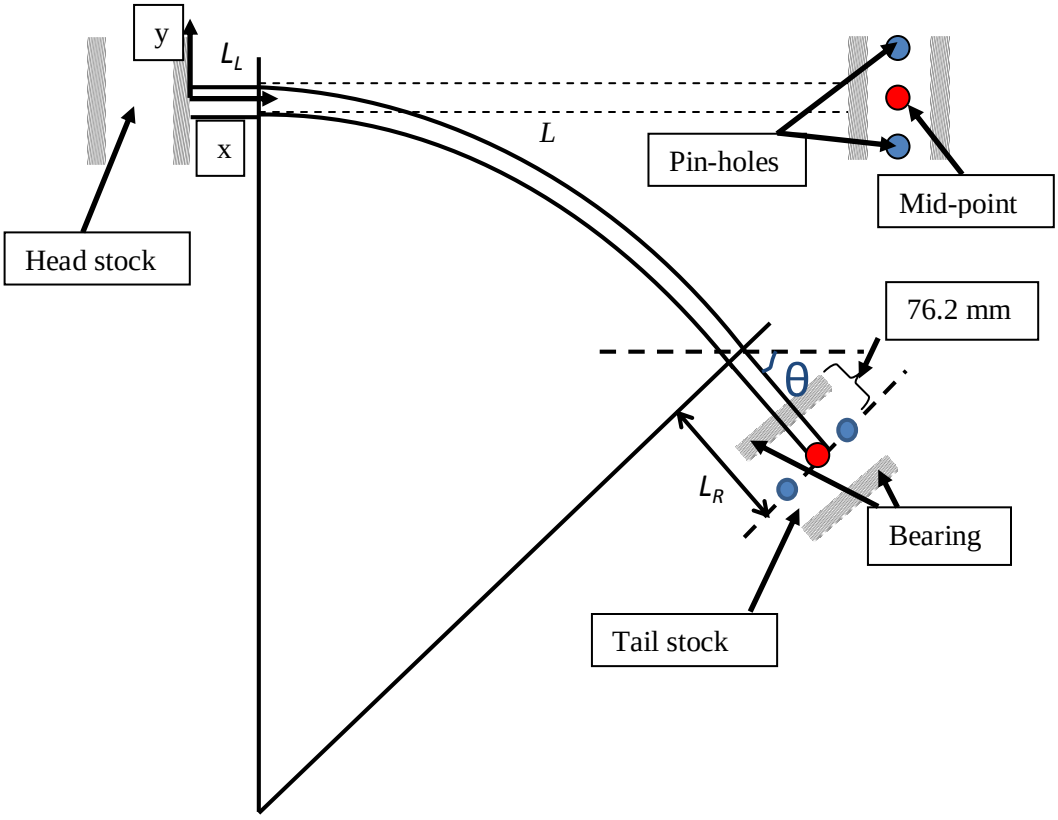

Figure **C-2**: Depiction of a misaligned shaft with labeled length segments

The angle δ and the coordinates of the midpoint location between the actual pin-holes was measured and compared to the theoretical midpoint coordinates in order for equation C-1to hold

true, allowing the misaligned shaft to have uniform strain. The theoretical midpoint coordinates for uniform strain can be calculated using equations C-2 and C-3 for a shaft of free length 381 mm.

$$x_{loc} = L_L + 2c\cos(\delta) + L_R\cos(\theta) \tag{C-2}$$

$$y_{loc} = 2c\sin(\delta) + L_R\sin(\theta) \tag{C-3}$$

where 2*c* is shown in Figure **C-1**. The distance from the front tailstock bearing to the pin-holes is 76.2 mm. The values for L_L and L_R were optimized using the Solver addon in Microsoft Excel until the alignment error, the product of the average percent error between the actual and theoretical pin-hole midpoints in the x and y direction, was minimized. The optimized solution yielded a value of 76.2 mm for L_L and 153.4 mm for L_R (Fig. **C-3**). The average deviation between the actual and theoretical pin-hole locations using optimized values for the length segments was less than 2 %.

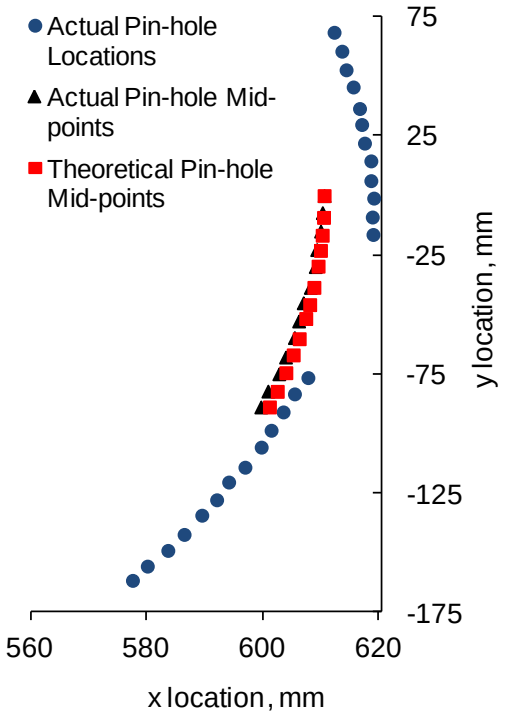

Figure **C-3**: Actual and theoretical pin hole locations with optimized L_L and L_R